Ministry of Higher Education

and Scientific Research

University of Babylon

College of Sciences for Women

Preparation of Polymer-Graphene/MoS_2 thin films by laser ablation: Characterization and optoelectronic Applications.

A thesis

Submitted to the Council of the College of Science for Women

University of Babylon in Partial Fulfillment of the Requirements for

the Degree of Philosophy of Doctorate in Laser Physics and its

Application

By

Nagham Mohammed Obaid

Supervised By

Asst. Prof. Amer K.H. Al.Nafiey

Prof. Dr. Ghaleb Abd-Alwahab Ali Al-Dahash

1444 A.H **2023A.D**

بسم الله الرحمن الرحيم

﴿ لَا يُكَلِّفُ اللَّهُ نَفْسًا إِلَّا وُسْعَهَا لَهَا مَا كَسَبَتْ وَعَلَيْهَا مَا اكْتَسَبَتْ رَبَّنَا لَا تُؤَاخِذْنَا إِنْ نَسِينَا أَوْ أَخْطَأْنَا رَبَّنَا وَلَا تَحْمِلْ عَلَيْنَا إِصْرًا كَمَا حَمَلْتَهُ عَلَى الَّذِينَ مِنْ قَبْلِنَا رَبَّنَا وَلَا تُحَمِّلْنَا مَا لَا طَاقَةَ لَنَا بِهِ وَاعْفُ عَنَّا وَاغْفِرْ لَنَا وَارْحَمْنَا أَنْتَ مَوْلَانَا فَانْصُرْنَا عَلَى الْقَوْمِ الْكَافِرِينَ ﴾

صدق الله العلي العظيم

(سورة البقرة : اية286)

Supervisor's certificate

We certify that this thesis entitled *" Preparation of Polymer-Graphene/MoS_2 thin films by laser ablation: Characterization and optoelectronic Applications"*. Was prepared by the student (***Nagham Mohammed Obaid***) under our supervision at the College of Science for Women, University of Babylon as partial fulfillment of the requirement for the Degree of Philosophy of Doctorate in Laser Physics and its Application.

Signature:

Name: Dr. Ghaleb Abd-Alwahab Ali Al-Dahash

Title: Professor

(Supervisor)

Date: / / 2023

Signature:

Name: Dr. Amer K. H. Al.Nafiey

Title: Assistant Professor

(Supervisor)

Date: / / 2023

Head of the Department Certificate

In view of the available recommendations, I forward this thesis for debate by the examining committee.

Signature:

Name: Jinan Ali Abd

Title: Professor

(Head of Laser Physics Department)

Date: / / 2023

Dedication

To my father and mother, the root to whom all that I am is attributed...

To my little family, my husband and children...

To my teachers, and everyone who taught me a letter, and I became a slave to him with my knowledge...

To the birds of paradise, who sacrificed their blood for us... our righteous martyrs.

Nagham

Acknowledgement

I want to express my deep gratitude and appreciation to my supervisor, Asst. Proof. ***(Amer K. H. Al.Nafiey)****, College of Science for women - Laser Physics and proof.* ***(Ghaleb Abd-Alwahab Ali Al-Dahash)****,College of Science for women - Laser Physics for their guidance, suggestions, and encouragement throughout the research work, without him, this thesis would have been impossible.*

Thanks and appreciation to Dr. ***(Jinan Ali Abd)*** *Head of the Laser Physics Department for her moral and scientific support. I also extend my thanks and gratitude to Dr.* ***(Ahmed Naji Abd)****, Al-Mustansiriya University / College of Science and to Dr.* ***(Alaa Hussein Ali)****, University of Baghdad for their wonderful position and scientific assistance in conducting laboratory tests to assist him in conducting laboratory tests. I also thank the virtuous brother, the assistant lecturer* ***(Rafie Tohme Ahmed)****, College of Science for women - Laser Physics, for his help in conducting laboratory tests.*

Finally, my thanks and appreciation go to the owner of great credit, my dear husband's assistant lecturer ***(Hassan Ali)*** *for his assistance to me during the preparation of this dissertation.*

Nagham

List of Symbols

Symbol	*Description*	*Units*
A	Area of the Photodetector	cm^2
c	Speed of Light	m/s
d	Lattice Space	A°
D_g	Crystallite size	nm
D^*	Specific Detectivity	$cm.Hz^{1/2}.W^{-1}$
E_c	Conduction Band	eV
E_v	Valance Band	eV
E_r	Fermi Energy Level	eV
E_g	Energy Gap	eV
h	Plack Constant	J.s
I	Current	A
I_d	Dark Current	mA
I_n	Noise Current	mA
I_{Ph}	PhotoCurrent	A
I_s	Saturation Current	µA
I_{sc}	Short Circuit Current	µA
J_s	Saturation Current Density in Dark	mA/cm^2
J_o	Saturation Current Density in Illumination	mA/cm^2
k_B	Boltzmann Constant	J/K
P	Power Density	mW/cm^2
q	Electronic Charge	C

List of Symbols

R_λ	Spectral Responsivity	$A.W^{-1}$
T	Transmission	%
t	Time	s
t_t	Film Thickness	nm
V	Voltage	V
V_{oc}	Open-Circuit Voltage	mV
η	Quantum Efficiency	%
λ	Wavelength of UV-VIS.NIR	nm
	Wavelength of X-Ray Diffraction	A°
ρ	Resistivity	Ω.cm
$\sigma_{d.c}$	Conductivity	$(\Omega.cm)^{-1}$
μ_h	Hall Mobility	$cm^2/Volt.s$
μ_e	Electron Mobility	$cm^2/Volt.s$
f	Frequency	Hz
α	Absorption Coefficient	cm^{-1}
ε	Complex Dielectric Constant	$J^{-1}C^2m^{-1}$

List of Abbreviations

The Acronym	*Description*
PL	Photoluminescence
MoS_2	Molybdenum Disulfide
CVD	Chemical Vapor Deposition
NP_s	Nanoparticles
TMD	Transition-Metal Dichalcogenide
S	Sulfide
Mo	Molybdenum
P_3HT	Poly(3-hexylthiophene-2,5-diyl)
LED_s	Light-Emitting diodes
FET_s	Field-Effect Transistor
PCE	Power Conversion Efficiencies
GF	Graphene Flake
CE	Counter Electrode
$DSSC_s$	Dye-Sensitized Solar Cells
PEDOT	Poly(3,4-ethylenedioxythiophene)
PSS	Polystyrene Sulfonate
CVD	Chemical Vapor Deposition
ML	multi-Layer
FL	few-layer
2D	Two-Dimension
J_{sc}	Short Circuit Photocurrent Density

List of Abbreviations

T.T	Thermal treatment
PLD	Pulse Laser Deposition
PLA	Pulsed Laser Ablation
PLAL	Pulsed Laser Ablation in Liquids
PVD	Physical Vapor Deposition
PSi	Porous Silicon
Si	Silicon
TEM	Transmission Electron Microscopy
SEM	Scanning Electron Microscopy
XRD	X-Ray Diffraction
UV	Ultraviolet
IR	Infrared
VIS	Visible
PEC	Photo Electrochemical
RMS	Root Mean Square
FTIR	Fourier Transform Infrared Spectroscopy
FWHM	Full Width at Half Maximum
HTL	Hole Transport Layer
rGo	Reduced Graphene Oxide
C.S	Crystallite Size
PBDTTT	polymer poly - benzo-alt-thienothiophen
PCBM	Phenyl-C61-butyric acid methyl ester

List of Contents

List of Contents

List of Contents

List of Contents

List of Contents

ABSTRACT

This work presents, for the first time, the production of P_3HT- G/MoS_2 nanocomposite by laser ablation of graphene and molybdenum disulfide (MoS_2) targets in Poly (3-hexylthiophene) (P_3HT) solution using a Q-switch Nd-YAG laser with a repetition rate of 1 (Hz) and different laser pulses of 200, 500 and 800 for both graphene and MoS_2 deposited onto a porous silicon (PSi) substrate using the drop-casting technique. The structural, topographical and optical properties of the prepared nanocomposite were analyzed using XRD, AFM, FTIR, TEM and UV-Vis spectroscopy analytical instruments.

XRD analysis indicated the existence of many peaks which belonged to G and MoS_2 nanoparticles (NP_s). The XRD analysis also showed a correlation between the intensity of these peaks and the number of laser pulses.

The results of FTIR analysis provide information about the strong bond between the nanocomposite elements for the P_3HT-G_{800P}/$MoS_{2\ 800P}$ sample. As observed by TEM imaging, G and MoS_2 NPs appear to be hemispherical shapes and the statistical results indicated that the size distribution was increased from 3.1 to 20.8 nm by increasing the number of laser pulses.

The observations of UV-Vis spectroscopy showed that the absorption coefficient and absorbance were increased by increasing the number of laser pulses due to the concentration of NP_s. The results also dicated that the indirect energy band gap of the P_3HT-G_{800P}/$MoS_{2\ 800P}$ sample is 2.1 eV which is very suitable for optoelectronic applications. The electrical study using the Hall effect shows that the P_3HT-G/MoS_2 nanocomposite is of an n-type and that the mobility and concentration of charge carriers depend on the laser pulses.

The P_3HT-G/MoS_2 nanocomposite was used to fabricate photodetector and solar cell devices. It has been found that the number of laser pulses that are used to produce G and MoS_2 NP_s affects the photodetector performance. The maximum value of the

spectral responsivity, specific detectivity and quantum efficiency of the fabricated detector was 0.36 A/W, 5.1×10^{12} cm.$Hz^{1/2}$.W^{-1} and 49.2% respectively at a wavelength of 900 nm due to the absorption edge of silicon. Whereas, the maximum value of the spectral responsivity, specific detectivity and quantum efficiency of the fabricated detector was 0.24 A/W, 3.39×10^{12} cm.$Hz^{1/2}$.W^{-1} and 38.9% respectively at a wavelength of 760 nm due to the absorption edge of P_3HT-G/MoS_2 NP_s, then, the fabrication of solar cells using P_3HT-G/MoS_2 nanocomposite and we investigated the effect of the number of laser pulses used to produce G and MoS_2 NP_s, on the efficiency of fabricated solar cells. The electrical properties of the fabricated solar cell were investigated in dark and light conditions and the results showed that its efficiency was 6.11% with V_{oc} and I_{sc} equal to 97 mV and 176 mA respectively.

Chapter One
Introduction and Review

1.1 Introduction

The chemical type and structure of a material's components are recognized to have a significant impact on its properties [1]. Bulk materials that contain a large number of atoms, in particular, can be identified by the energy bands that are responsible for most of the physical and chemical properties of solid materials due to the overlapping of atomic and molecular orbitals. As for nanomaterials with dimensions ranging from 1 to 100 nanometers, the number of atoms is so small that the electronic energy bands change dramatically, affecting all physical properties of materials [2–4].

Silicon and germanium are nanostructured semiconductors that emit visible light luminescence despite having modest and indirect band gaps in their bulk state [4]. The PL signals appear to be dependent on the size of nanostructures, implying that the quantum confinement effect is involved [4,5].

On the other hand, metals with nanostructures to have a variety of unique characteristics. Metallic nanoparticles show marked differences in colour when their size and shape differ, as well as changes in transmitted and reflected spectra [6,7]. These colour effects are linked to individual metal nanoparticles' efficient resonant absorption of light and the stimulation of localized surface Plasmon's, which are associated with metal electron collective oscillations [6].

There are many ways of producing graphene and molybdenum disulfide nanoparticles for device manufacturing and optoelectronics applications, such as mechanical exfoliation, liquid exfoliation, chemical vapor deposition (CVD), and so on. In this research, the laser ablation technique was used to produce nanoparticles for graphene and MoS_2, which is an environmentally friendly and inexpensive method**.**

1.2 Nanocomposite

Metallic nanoparticles (NPs) implanted in a dielectric multitude are significantly influenced by their physical and chemical characteristics, such as their distribution within the matrix and attributes like size, shape, or size dispersion. As a result, controlling these characteristics during manufacturing has long been a difficulty, and one of the biggest obstacles to the development of useful applications based on these materials has been the lack of production techniques with the required level of control [8]. It is the nanomaterials used in this study**:**

1.2.1 Molybdenum Disulfide (MoS_2)

MoS_2 is a type of transition metal dichalcogenide (TMD) material that has attracted significant attention in recent years due to its unique electronic and optical properties. Specifically, the interactions between the d-electrons in the metal atoms and the chalcogenide atoms in the material can result in emergent phenomena such as quantum confinement, spin-orbit coupling, and valley polarization [9]. TMDs are hexagonal in nature and absorb visible to infrared ranged light [10]. Molybdenum disulfide (MoS_2), is a well-known and thoroughly investigated TMD material with Mo atoms sandwiched between two layers of S atoms, along with environmental stability as shown in Figure(1.1) [11]. Moreover, it appears in nature as an n-type material [12], with visible to near-infrared light absorption [10], a large work function of 5.1 eV [13], mechanically stable and transparent for flexible devices [9].

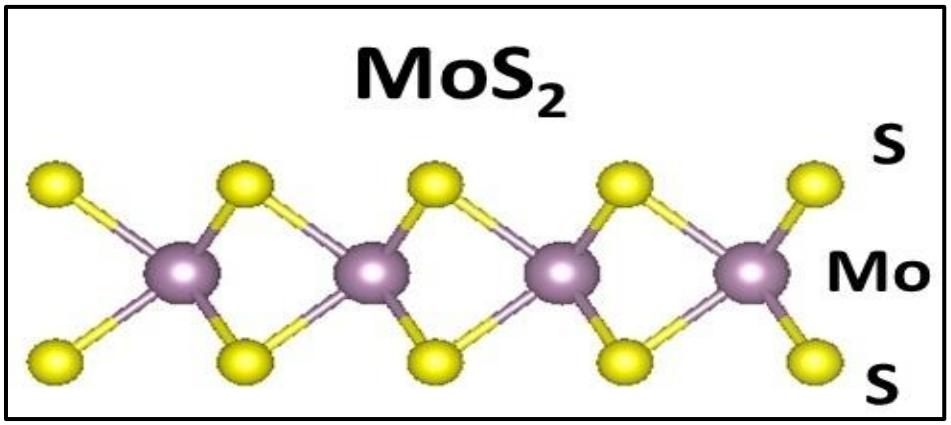

Figure(1.1): The MoS_2 structure [11].

Furthermore, these characteristics make MoS_2 and other transition metal dichalcogenide materials promising candidates for a wide range of applications, from electronic and optoelectronic devices to energy storage and conversion. For example, MoS_2 has been explored as a potential material for transistors, and photovoltaic cells [14]. The most attractive feature of MoS_2 is the variable energy gap from 1.2 to 1.8 eV as the material moves from bulk indirect bandgap to direct bandgap monolayer due to the quantum confinement effect. The MoS_2's physical properties are as in Table (1.1).

Table (1.1) :The physical properties of the MoS_2

Property	**Value**
Charge carrier mobility [15]	Up to 200 cm^2 /V·s
Molar mass [16]	160.07 g /mol
Band gap [17]	1.2 eV (indirect)
Specific density [16]	5.06 g/ cm^3
Melting point [18]	2648 K

Due to its direct bandgap, MoS_2 has a great advantage over graphene for several applications, including optical sensors and field effect transistors.

1.2.2 Graphene

Graphene, as shown in Figure (1.2). It is the basic structure of all forms of graphite, which is now used in most modern fields in the last decade. As a result of its unusual physical and chemical features, it has piqued the interest of researchers all over the world, proving its theoretical significance beyond a shadow of a doubt [19]. The physical characteristics of graphene are provided in the Table (1.2).

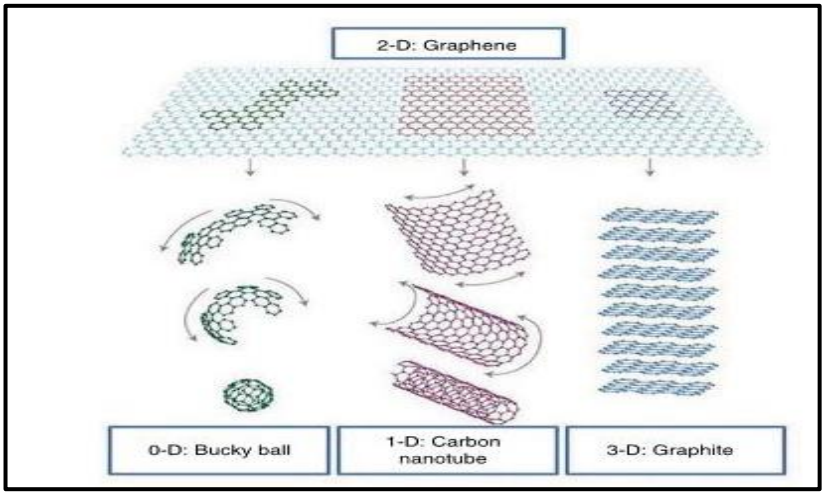

Figure(1.2): The structure of Graphene [20].

Table(1.2): The physical properties of the Graphene [21].

Property	Value
Charge carrier mobility	~200000 cm^2 /V·s
Thermal conductivity	(3-5)×10^3 W/m.K
Transparency	~ 97.4%
Band gap	0
Specific density	2.26 g/cm^3
Melting point	3800 K

Graphene is an attractive alternative material for diverse applications in electronic devices, fuel cells, biomedical sensors, energy storage, and super-capacitors due to its exceptional thermal, electrical, optical and mechanical properties [22].

1.2.3 Poly(3-hexylthiophene-2,5-diyl) (P_3HT)

P_3HT is a semiconducting polymer that has a p-type charge that is widely used in organic electronics and optoelectronics, such as solar cells, light-emitting diodes (LEDs), and field-effect transistors (FETs). It consists of a repeating unit of 3-hexylthiophene, which is a five-membered ring with a sulfur atom and a hexyl group attached to it [23], as shown in Figure (1.3). P_3HT has interesting optical properties due to its conjugated structure, which allows it to absorb and emit light in the visible range. It has a broad absorption spectrum that peaks around 550 nm, which corresponds to green light. The absorption coefficient of P_3HT is relatively high, which makes it a good candidate for use in solar cells [24]. P_3HT also exhibits fluorescence and phosphorescence, which are processes that involve the emission of light after excitation by light. The emission spectrum of P_3HT depends on the excitation wavelength and the processing conditions, but it typically peaks around 650 nm, which corresponds to red light [25]. Some physical properties of P_3HT are shown in the Table (1.3).

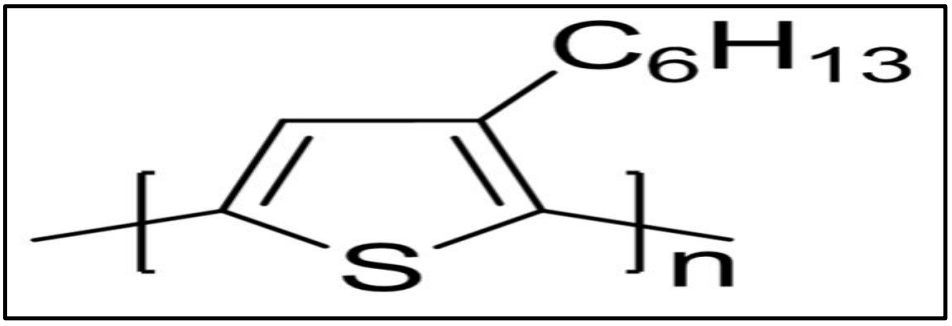

Figure(1.3):The chemical structure of poly(3-hexylthiophene)P_3HT[26].

Table(1.3): The physical properties of the polymer P_3HT.

Property	Description
Density	1.33 (g/cm^3)
Chemical formula	$(C_{10}H_{14}S)_n$
Solubility	Chloroform, chlorobenzene
Band gap [26]	2.1 eV
Hole mobility [27]	10^{-5} - 10^{-2} $cm^2(V\ s)^{-1}$
Electron mobility [28]	6×10^{-4} - 1.5×10^{-4} $cm^2(V\ s)^{-1}$
Decomposition temperature	300-400°C

1.3 Polymer-Based Nanocomposites in Solar Cell

Organic/inorganic nanocomposites have very important applications in devices such as photodiodes, photovoltaic cells, light-emitting diodes, and gas sensors [29]. The properties of the nanocomposite film can be easily modified by changing its composition [30]. A solar cell converts light energy into electrical energy through the photovoltaic process. The progress in photovoltaic technology started with the research of a French Physic Antoine-César Becquerel in 1839. The photovoltaic effect was observed during the experiment with a solid electrode in an electrolyte solution when the light falling upon the electrode created voltage. Using Photovoltaic cells has been one of the main methods to capture and convert solar energy.

Solar cells are on inorganic materials mostly silicon because of high power conversion efficiencies (PCE), up to 25%, due to the excellent charge transport properties and environmental stability [31,32].

The organic solar cells based on conjugated polymers have a high absorption coefficient and high rate of photon absorption [33]. In addition, they are advantageous because of (i) photo and electronic characteristics of conjugated polymers that may be enhanced by changing their chemical structure [34], (ii) the coating and printing techniques can be used to decrease the cost of fabrication procedure [35], and (iii) the flexibility enables to manufacture flexible devices [36,37]. In the last few years, remarkable work has been done to develop organic solar cells [38].

1.4 Photodetectors

Photodetectors are sensors of electromagnetic radiation (photons) that convert the optical signal into an electric signal proportional to the radiation intensity. The capability of certain materials to generate current when exposed to light was noticed first by Antoine Becquerel in 1850 but the first theoretical explanation of this phenomenon was given in 1936 by Vladimir Zworykin *et al*.[39]. Semiconductor-based photodetectors typically photodetectors have a p–n junction that converts light photons into the current. The absorbed photons make electron–hole pairs in the depletion region [40].

1.5 Literature Survey

Synthesis and characterization of polymer - graphene / MoS_2 had an interest during the past century and one can review them as related to the present work as follows:

In 2013, Lin *et al.* [41] studied, graphene flake (GF) was successfully embedded into a nanosheet like molybdenum sulfide (MoS_2) matrix via an in situ hydrothermal route, and the resultant hybrid was employed as a

counter electrode (CE) for Pt-free dye sensitized solar cells (DSCs). It is confirmed from scanning electron microscopy, X-ray diffraction, Raman spectroscopy and transmission electron microscopy that GFs are successfully incorporated in the nanosheet like MoS_2 matrix and thus result in its surface evolution. The DSC assembled with the novel nanosheet like MoS_2/GF hybrid CE exhibits a high photovoltaic conversion efficiency of 6.07%

In 2013, Li *et al.* [42] reported a facile solution processed method to fabricate a MoS_x anode buffer layer through thermal decomposition of $(NH_4)_2MoS_4$. Organic solar cells based on in situ growth of the MoS_x film as the anode buffer layer showed impressive improvements, and the power conversion efficiency was even better than that of a conventional poly(3,4-ethylenedioxythiophene) polystyrene sulfate (PEDOT:PSS) based device. The MoS_x film was systematically examined by Raman spectroscopy, XPS and AFM. The results indicated that both MoS3 and MoS_2 were beneficial to the device performance. MoS_2 could lead to higher J_{sc} because of improved hole extraction and light absorption, but V_{oc} decreased because of the lower conduction band , hence, resulted in recombination at the interface. When MoS_3 and MoS_2 reached the balance, the highest the power conversion efficiency of 3.90% was achieved, which was even higher than that of a conventional PEDOT:PSS-based device (3.64%).

In 2013, Yun *et al.* [43] used MoS_2 as both an electron extraction layer and a hole with drawal layer. p-type doped MoS_2 was used for the hole withdrawal layer, and n-type doped MoS_2 was used for the electron extraction layer. photon conversion efficiency increased from (2.8 %) to

(3.4%) in organic solar cells using p-type doped MoS_2 as a hole extraction layer. Particularly, after n-doping the photon conversion efficiency (PCE) was dramatically increased due to the change in work function compared with undoped MoS_2 thin films.

In 2014, Lei *et al.* [44] employed MoS_2 as a counter electrode material for dye sensitized solar cells (DSSCs) in three different structural: MoS_2 nanoparticles, multi layered MoS_2 and few layered MoS_2. The photon conversion efficiency of various MoS_2 morphologies is (5.41 %) for MoS_2 NPs, (2.92 %) for ML- MoS_2 and (1.74 %) for FL- MoS_2.

In 2014, Yang *et al.* [45] employed MoS_2 as a hole layer in an organic solar cell. UV–ozone post-treatment of 2D MoS_2 sheets led to the incorporation of oxygen atoms into the lattice of the sheets. The incorporated oxygen in 2D MoS_2 sheets significantly improved the performance of organic solar cells (OSCs), with a photon conversion efficiency (PCE) of 4.99 %. This is due to the possibility of using MoS_2 sheets as hole transport layers in organic solar cells. Also, MoS_2 nanosheets and oxygen containing MoS_2 nanosheets demonstrated superior optical transparency in the wavelength range (400–900) nm.

In 2014,Yang, *et al.* [46] develop a novel hole transport layer (HTL) composed of ultrathin two-dimensional, molybdenum disulfide (MoS_2) sheets decorated with 20 nm gold nanoparticles (MoS_2@Au) to make use of plasmonics for organic solar cells (OSCs). Both experimental and theoretical simulations results show that the MoS_2 @Au composite HTL for OSCs can more efficiently utilize the enhanced near-field, particularly along the horizontal direction. Coupled with the hole extraction capacity of the 2D MoS_2 layer, the plasmonic OSC device with MoS_2 @Au HTL

containing 12.5 vol% Au decoration density led to a J_{sc} enhancement of 15.6%; this resulted in a PCE of 7.25%, corresponding to an enhancement of 17.3% compared to the device with an HTL consisting of 2D MoS_2 alone.

In 2015, Hu *et al.* [47] used MoS_2 as an interfacial layer, and silver nanowires were used in conjunction with MoS_2 to create a transparent electrode. At 550 nm, AgNW- MoS_2 exhibits (93.1 %) transparency as a transparent electrode. and has a reduced sheet resistance, when compared to the Ag NW electrode alone, MoS_2 in the AgNW- MoS_2 composite electrode enhances environmental dependability and offers the best oxidation and moisture resistance. PBDTTT-C-T: A PC70BM-based organic solar cell with a cathode made of Ag NWs- MoS_2 nanosheets/n- MoS_2 nanosheets and an anode made of p- MoS_2 nanosheets/Ag for hole extraction produces a PCE of 8.72 %. the general cell structure is glass/Ag- MoS_2/n- MoS_2/PBDTTT-C-T: PC70BM/p- MoS_2/Ag.

In 2015, Chuang, *et al.* [48] They prepared gold nanoparticle-decorated molybdenum sulfide (AuNP@MoS_2) through a simple spontaneous redox reaction. Transmission electron microscopy, UV-Vis spectroscopy, and Raman spectroscopy were used to characterize the properties of the AuNP@MoS_2 nanomaterials. Employed such nanocomposites as the cathode buffer layers of organic photovoltaic devices (OPVs) to trigger surface plasmonic resonance, leading to noticeable enhancements in device efficiencies (PCE = 4.91 %).

In 2015, Jian, *et al.* [49] studied role of MoS_2 as an effective interfacial layer in graphene/silicon organic solar cells. By varying MoS_2 film annealing temperature and thickness. It is found that the power conversion efficiency (PCE) is increased from ~2.3% to ~4.4% with 80

°C annealed MoS_2 film whereas it drops significantly to ~0.6% with 200 °C annealed MoS_2 film. Besides, the PCE increases gradually with decreasing MoS_2 film thickness. The PCE can be further enhanced to ~6.6% with the aid of silicon surface passivation.

In 2015, Tsuboi *et al.* [50] demonstrated that the photovoltaic performances of graphene/Si Schottky junction solar cells were significantly improved by inserting MoS_2 thin-film layer by a chemical vapor deposition. This layer functions as an effective hole transporting layer. A high photovoltaic conversion efficiency of 11.1% was achieved with the optimized trilayer graphene/MoS_2/n-Si solar cell.

In 2015, Zongyu Huang *et al.* [51] fabricated a novel sunlight photo-detector based on a MoS_2/graphene heterostructure. The MoS_2/graphene heterostructure was prepared by a facile hydrothermal method. Photoresponse investigations performed by a photoelectrochemical (PEC) measurement system indicate that the synthesized MoS_2/graphene heterostructure shows superior photoresponse activities under the illumination of sunlight in contrast with bare MoS_2 and graphene. The improved photoresponsivity can be attributed to the enhanced light absorption, strong light matter interaction and the extremely efficient charge separation of the heterostructure.

In 2016, Rehman *et al.* [52] used the Al_2O_3 layer on the MoS_2 surface to improve the performance of the solar cells based on MoS_2/silicon. The power conversion efficiency of (PCE= 5.6%) was obtained, which is higher than the conversion efficiency of the solar cell based on MoS_2/silicon without adding the Al_2O_3 layer, which is (PCE =2.21%).

In 2016, Domenico De Fazio *et al.* [14] introduced flexible photodetectors (PDs) for visible wavelengths fabricated by stacking centimeter-scale chemical vapor deposited (CVD) single layer graphene (SLG) and single layer CVD MoS_2, both wet transferred onto a flexible polyethylene terephthalate substrate. The operation mechanism relies on injection of photoexcited electrons from MoS_2 to the SLG channel. The external responsivity is 45.5A/W and the internal 570A/W at 642 nm. This is at least 2 orders of magnitude higher than bulk-semiconductor flexible membranes. The photoconductive gain is up to 4×10^5. The photocurrent is in the 0.1–100 μA range. The devices are semitransparent, with 8% absorptance at 642 nm, and are stable upon bending to a curvature of 1.4 cm. These capabilities and the low-voltage operation (<1 V) make them attractive for wearable applications.

In 2016, Herme G. Baldovı´ *et al.* [53] synthesized MoS_2 quantum dots (QDs) have been in colloidal suspensions by 532 nm laser ablation (50 mJ/pulse) of MoS_2 particles in acetonitrile. High resolution transmission electron microscopy images show a lateral size distribution from 5 to 20 nm, and exhibit photoluminescence (PL) whose varies from 430 to 530 nm depending on the excitation wavelength. MoS_2 QDs were used as a photo catalyst to generation H_2 after mixing it with methanol solution and irradiating it with a Hamamatsu xenon lamp (235-850) nm.

In 2018, Palsaniya *et al.*[54] reported the synthesis of nanocomposites of polyaniline (PANI), with equal weight% of graphene (G) and MoS_2, prepared via in-situ oxidative polymerization of PANI, along with PANI-G binary nanocomposites. The morphological analysis confirms the formation of well-dispersed composite materials, and the ternary composite appears to be an interlayered structure of graphene and MoS_2,

encapsulating the PANI nanorods. The ternary composite PANI-G-MoS_2 symmetric electrode measurement exhibits a remarkably high specific capacitance (Cs, 142.30 F g^{-1}) over binary composites under galvanostatic charge-discharge (GCD) cycles. The improved cyclic stability has contributed significantly in recovering the capacitance retention as high as 98.11% in comparison with pure PANI (~40%) and binary composites (~60–96%). Further, PANI-G-MoS_2 symmetric electrode (viz., based on two electrode measurement) exhibits a high energy density (2.65 Wh kg^{-1}) at a power density of 119.21 W kg^{-1}, which is attributed to the high charge transport phenomenon occurs at the interfacial region between electrodes and electrolyte.

In 2018, Aydın, *et al.* [55] studied investigated the effect of a poly (3-hexylthiophene-2.5-diyl)(P_3HT) – graphene on the photoresponsivity characteristics of Si-based Schottky photodetectors. P_3HT which is known to be an electron donor and absorb light in the visible spectrum, was placed by dip-coating method on the graphene prepared by chemical vapour deposition. Current–voltage measurements of graphene/Si and P_3HT–graphene/Si behaviour confirming a Schottky junction formation at the graphene/Si interface. We found that the maximum spectral photoresponsivity of the P_3HT–graphene/Si photodetector at wavelength of 850 nm is about 0.78 A W^{-1}, It is three times more than the spectral response of graphene/Si photodetector which is about 0.24 A W^{-1}

In 2019, Nahid *et al.* [56] MoS_2-PANI hybrid structure were synthesized by internal polymerization of hydrothermally synthesized MoS_2 nanosheets with PANI for its application in photodetectors. Field-Emission Scanning Electron Microscopy (FESEM), High-Resolution Transmission Electron Microscopy (HRTEM), X-Ray Diffraction (XRD),

Fourier Transform Infrared Spectroscopy (FTIR) and UV–vis spectroscopy delete were performed to characterize the synthesized sample. The optical sensor of MoS_2-PANI hybrid structure were fabricated and altogether studied using laser excitation wavelengths (λ_{ex}): 635 nm (red), 785 nm (infra-red) and 1064 nm (near infra-red). The evaluated value of photoresponsivity of hybrid structure is quite high compared to the previously reported MoS_2 nanosheets based optical sensor. At 785 nm, maximum photoresponsivity of 25 A/W is observed at fixed power density of 1.4 mW/mm^2. The photoresponsive characteristics of MoS_2-PANI hybrid structure were examined as a function of optical power density.

In 2019, Ramasamy *et al.* [57] prepared MoS_2 nanosheets via a simple exfoliation method; then, they were blended into a conducting conjugated polymer (PEDOT:PSS),where use the nanocomposite (PEDOT: PSS/ MoS_2) as a hole extraction layer in solar cells based on P_3HT: PCBM ([6,6]-phenyl-C61-butyric acid methyl ester) .The devices using this hybrid film HTL showed power conversion efficiencies up to 3.74%, which is 15.08% higher than that of the reference ones having PEDOT:PSS as HTL.

In 2020, Sujit Kumar *et al.* [58] fabricated highly efficient ultraviolet (UV) photodetector based on Molybdenum Disulfide (MoS_2) layers using pulsed laser deposition (PLD) technique, and was the specific detectivity (D*) is (1.8×10^{14}) $cm.Hz^{1/2}W^{-1}$.

In 2020, Krishnamoorthy *et al.* [59] reported on the simple hydrothermal synthesis of diverse compositions of molybdenum sulfide (MoS_2)/graphene nanocomposites and their subsequent application in

dye-sensitized solar cells (DSSCs). The power conversion efficiency is about (PCE=8.92%) for MoS_2/graphene and is higher than the conversion efficiency of MoS_2 without graphene (PCE=3.36%) because graphene increased the charge collection faster and sensitized the dye better.

In 2021, Musaab Khudhur *et al.* [60] fabricated a nanocomposite of polymer/Graphene-Ag , and its application as a photodetector, it is observed that all the films have responsivity extended from visible to near-infrared region. The quantum efficiency increased from 2.26% for the PVA/p-Si device to 14.5% for the n-PVA/G(400P)/Ag(700p)/p-Si device and also from 2.9% for PMMA/p-Si to 24.18% for n-PMMA/G(400p)/Ag(700p)/p-Si device respectively.

In 2021,Baby *et al.* [61] prepared poly methyl methacrylate (PMMA)-MoS_2 nanocomposite films were by impregnation of exfoliated MoS_2 nanosheets into PMMA matrix by drop casting method. Synthesis of exfoliated MoS_2 nanosheets through microwave irradiation techniques was found to be simple, less time consuming, eco-friendly and cost effective. These optimized exfoliated MoS_2 nanosheets were introduced into the polymer matrix which was then subjected to different characterization techniques. The effect has been studied of exfoliated MoS_2 nanosheets on the mechanical properties of the polymer-MoS_2 composite.

In 2021,Samira and Mohammad Reza [62] obtained MoS_2 nanoparticles (NPs) by the laser ablation (Nd:YAG ,λ = 1064 nm) of a bulk MoS_2 in ethylene glycol solution, as a function of the laser fuence for the first time. The properties of the product were characterized using UV–vis, TEM, SAED, SEM with EDX, XRD, FT-IR, and Raman spectroscopy.The results showed that the synthesized MoS_2 NPs have a

hexagonal crystalline structure with diameters of 4–160 nm. In addition, most of them had a rounded shape whose λ_{max} varied from 212.5 to 216.5nm depending on the laser fuence. By increasing the laser fuence, the average size of these particles increased from 10 to 18 nm.

In 2021, Jun Maa *et al.* [63] described a novel method to synthesize MoS_2 by using pre-annealed sulfurized Mo foil. MoS_2 monolayers inserted at the graphene/n-Si interfaceis act as photon absorbing layers. This significantly improves the photovoltaic conversion efficiency of graphene-based Schottky junction solar cells. In heterojunction solar cells based on 2D materials, a comparatively high conversion efficiency of 12 % is successfully obtained.

In 2021,Dong Hee Shin *et al.* [64] made flexible solar cells from MoS_2, which works as a hole transfer layer with a transparent conductive electrode. The power conversion efficiency of these solar cells depends on the number of MoS_2 layers as well as on the concentration of doping, where the value of the power conversion efficiency PCE reached the greatest possible when the number of layers is (Ln=2) and the concentration of doping is (nD =20mM). When the active layer with quantum dots was added to the solar cell installation, the efficiency of the conversion power was increased to 4.23% and this efficiency was maintained after conducting the tests, which indicates the mechanical stability of this solar cell.

In 2022, Zhiwen Li *et al.* [65] reported a waveguide integrated MoS_2 photodetector operating at the telecom band, which is enabled by hot-electron assisted photodetection, a photoresponsivity of 15.7 mAW^{-1} at a wavelength of 1550 nm is obtained with a low bias voltage of 0.3 V.

In 2022, Yi-Shan *et al.* [66] enhanced the performance of a photodetector by modifying the rGO film with hydrophilic polymers poly(vinyl alcohol) (PVA) is reported. Compared with the rGO photodetector, the on/off ratio for the PVA/rGO photodetector shows 3.5 times improvement, and the detectivity shows 53% enhancement even when the photodetector is operated at a low bias of 0.3 V.

In 2022,Augustine *et al.* [67] fabricated a heterostructure of MoS_2/SnO_2. A SnO_2 film was deposited by Sn sputtering followed by oxidation of a Sn film in the ambient. Later, a MoS_2 film was deposited on SnO_2 by pulsed laser deposition. Under NIR illumination, the device exhibits excellent photoresponse with a responsivity of 0.35 A W^{-1} and a detectivity of (1.25×10^{11}) $cm.Hz^{1/2}W^{-1}$ at 0 V. The excellent performance of the device is attributed to the high electron transport behaviour of SnO_2 and a built in electric field at the interface.

In 2022, Velasco Davoise *,et al.* [68] discuss briefly the synthesis methods of Graphene-related materials (GRMs) and describes the current progress in GRM-based organic solar cells (OSCs). PV parameters (short circuit current, open circuit voltage, power conversion efficiency and fill factor) are summarized and comparatively discussed for the different structures. The efficiency recently surpassed 15% for an organic solar cell(OSC) incorporating polymer-modified graphene as a transparent electrode.

In 2023, Fu *et al* . [69] prepared a photodetector based on a hybrid dimensional heterostructure of laterally aligned multiwall carbon nanotubes (MWCNTs) and multilayered MoS_2 using the micro-nano fixed point transfer technique. The device demonstrated a responsivity of

(3.67×10^3) A/W at (λ =520 nm) and (718) A/W at (λ = 1060 nm). Moreover, the detectivity (D*) of the device was found to be (1.2×10^{10}) cm.$Hz^{1/2}W^{-1}$ at (λ = 520 nm) and (1.5×10^9) cm.$Hz^{1/2}W^{-1}$ at (λ = 1060 nm), respectively. The device also demonstrated external quantum efficiency (EQE) values of approximately 8.77×10^5 % at (λ = 520 nm) and 8.41×10^4 % at (λ = 1060 nm).

In 2023,Loeza-Poot,*et al.* [70] conducted a systematic study of the effects of the precursor solution (PS) processing and the post deposition thermal treatment (T.T) on the optical properties of P_3HT:PCBM absorber layer, by applying a central composite design of experiments. Results revealed that the temperature is the factor with the greatest influence on material properties; while the stirring time by itself is the least significant; however, its interaction with high temperature promotes the structural disorder, inducing degradation of the absorber layer. The DOE showed that P_3HT: PCBM layers with appropriate optical properties to be applied in OSCs are fabricated with a PS stirred at 53.5 °C for 18 h, and the post deposition thermal treatment below 150 °C. These results were corroborated with X-ray diffraction, microscope optical images, electrical and optical responses of manufactured solar cells.

1.6 Aim of this Study

1. Fabrication of a thin film from (Polymer, Graphene, MoS_2) materials using the pulsed laser ablation method.
2. Complete study of the properties of the (Polymer - Graphene / MoS_2) heterojunction to show its optical, structural, surface and electrical properties.
3. (Polymer - Graphene/MoS_2) heterojunction application in the work of a solar cell, photodetector and the study of its basic parameters.

Chapter Two

Theoretical Background

2.1 Introduction

The production of nanoparticles by laser ablation of solid materials, whether in a gas or in a vacuum, has been extensively explored during the past two decades. The laser ablation method has received great attention as a new technique for producing nanoparticles, which represents the phenomenon of laser material processing, as the amount of mass removed depends on the laser parameters such as (pulse duration, number of pulses, energy, wavelength, properties of the target material, and the surrounding environment) [71]. Finally, this chapter gives a general description of the PLAL technique and the theoretical part containing the characteristics of Structural, optical, electrical, and optoelectronic.

2.2 Laser - Material Processing

Laser beam provides the capacity to accurately transfer large energy amounts to confined areas of a material in order to achieve the required response [72]. The material must be absorption of the laser beam to have an effect on it. This absorption is remarkable in the process of laser-material interaction. This absorption process is a major source of energy within the material, this main source, shows that the beam of laser released from the source determines what occurs to the laser-irradiated material [73]. In Figure (2.1), the incident pulse of the laser heats the material target quickly, leading to shifting in phase and generating stress waves in the irradiated target. Then the material begins to melt and turns to a gaseous state, this happens in a very short time and plasma is created. The beam of laser will be absorbed by the plasma flame, resulting in the attenuation of the light intensity falling on the target, also due to the excitation and ionization of the plasma field, the plasma extends and

moves away from the zone of reaction to reach the base (substrate) and form a thin film layer [74].

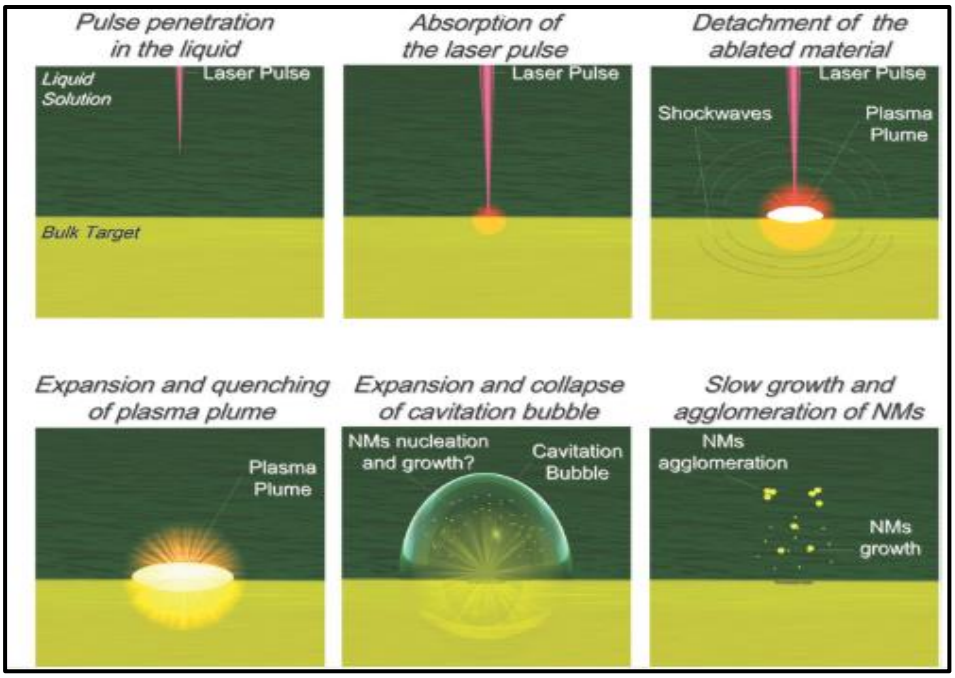

Figure(2.1): Laser Ablation and Particles Formation[75].

2.3 Synthesis of Nanoparticles

There are different approaches to synthesize nanomaterials (NMs), including the bottom-up and the top-down approaches Figure (2.2). In the bottom-up approach, NPs are first obtained at the atomic level and then integrated into the desired material. This includes the formation of NPs from colloidal dispersion and the formation of powders from the sol–gel method, which is then followed by integration. Other examples include sedimentation, reduction, green synthesis, spinning, biochemical synthesis, atomic layer deposition, molecular self-assembly, and vapor phase deposition of NM_s [76]. In the top-down approach, a bulk material at the macroscopic level is trimmed down to the desired NPs by different means. Some examples of this are etching, ball milling, CVD, physical vapor deposition,

optical lithography, e-beam, soft lithography, nanoimprint lithography, block copolymer lithography, and scanning probe lithography.

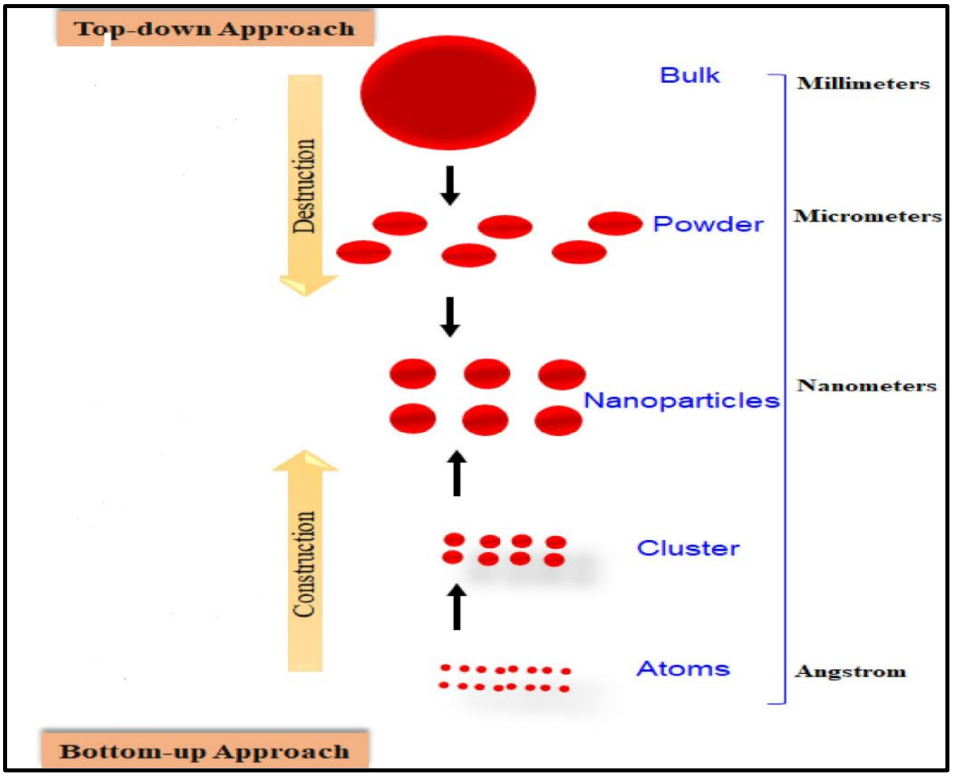

Figure (2.2): Schematic Illustrating the Top-down and Bottom-up Methods for Nanoparticle Preparation [76].

2.4 Synthesis Methods for 2D Materials

The synthesis method of high-quality 2D materials with large dimensions, controllable thickness, large crystal domain, and minimum defects is essential for realizing high-performance [77]. Until now, mechanical exfoliation, liquid exfoliation, CVD and PLAL are the main methods to synthesize 2D materials. So, will summarize how laser ablation works in liquids:

2.4.1 Pulsed Laser Ablation in Liquid Technique (PLAL)

First works of laser ablation in a liquid milieu for a fabrication of colloidal nanostructures were undertaken by researchers in chemistry [78]. These, mostly fundamental studies examined the potential of laser ablation technique for the production of stable solutions of various nanoparticles. The Figure (2.3) shows diagram of the main stages of PLAL. The main difference of laser ablation in liquids compared to the one in residual gases consists of the following:

(i) Much more efficient breakdown of a relatively dense liquid medium, which can absorb a significant amount of radiation energy; an efficient energy transfer from laser plasma to the surrounding liquid and a formation of a cavitation bubble.

Two phenomena can be clearly distinguished. The first one is the formation of a plasma jet in the first moments after the laser action. This jet was attributed to radiation-related ablation of material. The second one is the formation of the cavitation bubble, which grows until (150–250) s and then collapses. The collapse of the bubble releases a significant amount of mechanical energy and can become an additional source of material ablation.

(ii) An absorption of incoming radiation by nanoparticles produced, which are suspended in a solution. If the wavelength of pumping radiation is near some absorption bands of the nanoparticles, the radiation energy can be efficiently absorbed, yielding different effects such as a secondary ablation of material [79], fragmentation of colloidal particles, and even the formation of complex chemical compounds [80]. The laser ablation in liquids leads to the efficient production of nanoparticles, which are released into the liquid forming a colloidal solution. Such a

process is usually accompanied by a visible coloration of the liquid. However, when the ablation is performed in pure water or any other solution in the absence of chemically active components, the size of nanoparticles produced is relatively large, since the coagulation and aggregation processes of hot ablated atoms after the ablation process cannot be easily overcome. In particular, nanosecond ablation, used in most works, generally gives relatively large (10–300) nm and strongly dispersed [81].

It should be noted that for nanosecond pulses, size control can be achieved by decreasing the wavelength of pumping radiation, or decreasing the pulse width [82,83]. The size properties can also be somewhat controlled by varying the laser fluence [81].

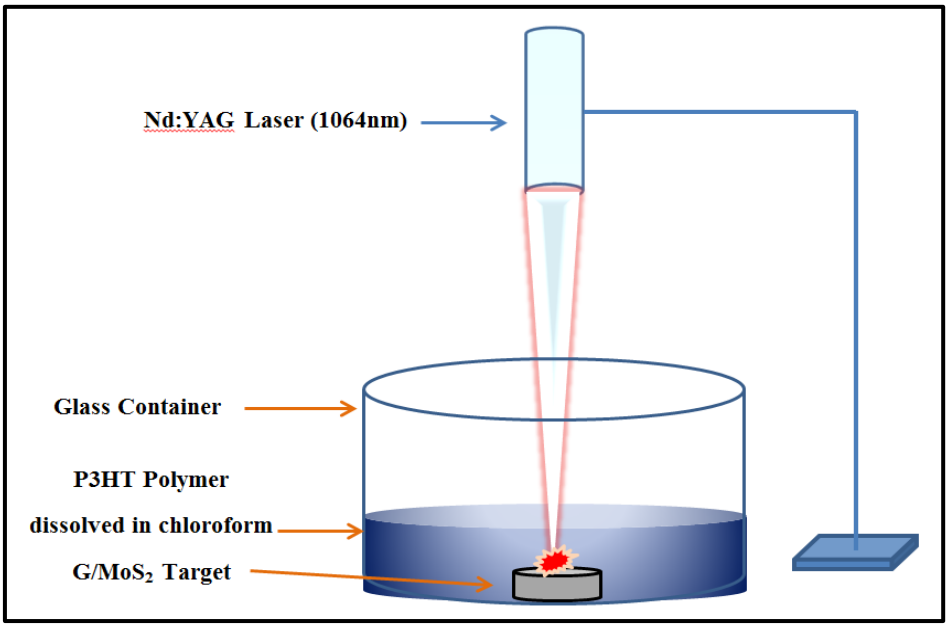

Figure (2.3): Diagram of the Main Stages of PLAL.

2.5 The Reasons for Using Ablation Laser in Liquids

1- The high purity of the finished products is a highlight of the PLAL technique .

2- PLAL is one of the experimental setup's lowest cost methods compared to other techniques requiring a vacuum chamber, high temperature or high pressure, etc.

3- The liquid environment plays an important role in cooling the ablated material [84].

2.6 Effect of Laser Parameters

The main, obvious, parameter of PLAL is the target material However, due to a complex cascade of physical–chemical phenomena, laser ablation in liquids does not necessarily give NP_s with the same phase and composition of the bulk target. Moreover, different materials show different reactivity and yield different products under the same experimental conditions. In general, all laser parameters affect the final NM_s. These parameters are:

2.6.1 Pulse Wavelength

The overlap of formed NP_s with incoming laser pulses occurs in the PLAL setup therefore the use of wavelengths that are not absorbed by the NM is preferred to avoid interaction with the products. If NPs absorb laser pulses, they may undergo further modifications during the synthesis [85].

The skin depth (i.e. the absorption coefficient) of the target depends on pulse wavelength. Usually, at shorter wavelengths, the absorption

coefficients of solid materials are larger. For instance, UV radiation is efficiently and uniformly absorbed by interband transitions in metal targets, yielding the regular erosion of all the irradiated area [87]. Conversely, near-infrared radiation is absorbed preferentially by defects and impurities in the metal target, generating a rugged erosion of the spot area. UV and NIR wavelengths are considered to be two oppose extreme cases, while visible light shows intermediate properties [86].

2.6.2 Pulse Energy

The pulse energy affects the amount of ablated material and the ablation mechanism [87]. NP_s productivity increases almost linearly with pulse energy as far as the dominating ablation mechanism remains the same [88]. When the pulse energy is increased, larger size distributions and larger average NP_s sizes are observed [89]. This is the concomitant effect of the larger amount of ablated material, which implies an higher concentration of target species in the plume, and of the detachment of solid and melted fragments, which is more probable at high energy.

2.6.3 Spot Area

When the spot area is increased by keeping the fluence unchanged, the NP_s productivity also increases. In theory, one may expect that a larger spot area corresponds to a smoother gradient of temperature, pressure, concentration and consequently, to a more homogeneous structure of the final products [90].

2.6.4 Repetition Rate.

The repetition rate defines the time interval (Δt_p) between consecutive laser pulses, with a higher repetition rate corresponding to a smaller Δt. The productivity of NP_s for unit time increases with the repetition rate However, the linear increase is observed only for Δt_p longer than the lifetime of the cavitation bubble, which is of the order of (10^{-4} –10^{-3}) s [91]. This corresponds to repetition rates lower than (10^3 – 10^4) Hz.

2.6.5 Number of Laser Pulses

A rough surface absorbs more light, but not homogeneously in all its parts, with consequence inhomogeneities in the profile of the detached material [86]. The concentration of NMs increases in solution for an increasing number of laser. The number of laser pulses is proportional to the ablation time. The amount of ablated material increases with the number of laser pulses [92].

2.7 Manufacture of Porous Silicon by Photoelectrochemical Etching

Porous silicon (P-Si) has been studied by researchers recently, primarily focusing on its photoluminescence properties and potential applications in fields such as photovoltaic devices, chemical sensors, and biological sensors. One commonly employed method for producing porous silicon is photoelectrochemical etching (PECE) using silicon wafers immersed in an electrolyte containing hydrofluoric acid (HF) and surfactants, particularly ethanol [93,94]. In this technique, a photon source such as lasers or intense light is utilized to introduce the necessary

holes in the irradiated region of the silicon wafer, initiating the etching process. This technique offers several advantages, including:

1- Simplicity of the process.

2- Controllable processes with precise processing parameters.

In this method, the silicon wafer acts as the anode, while platinum or other conductive materials resistant to HF serve as the cathode. To withstand the highly corrosive of hydrofluoric acid, the electrolysis cell is typically constructed from acid-resistant polymers like teflon [95].

2.8 Optical Properties

The study of the optical properties of semiconductors is of great importance to learn a lot about the electronic transitions that occur in materials, as well as the structure of energy bands, optical energy gaps and optical constants such as refractive index and dielectric constant in its real and imaginary parts, as well as used to study lattice vibrations, and optical properties represent one among the main results whose results were based on many analyzes about the nature of the atomic structure of the material, as well as the effect the material's absorption of light photons in the occurrence of electronic transitions within its packet structure, and thus knowledge of the structure of energy bundles, and gives information about the value of the energy gap if it is direct or indirect [96].

2.8.1 Absorption Edge

It is the rapid increase in absorption when the absorbed radiation energy is approximately equal to the energy gap, therefore, the absorption edge represents the lowest energy difference between the highest point in

the valence band and the lowest point in the conduction band [97]. Absorption regions are divided into three regions as in Figure (2.4):

- High Absorption Region (part A)

This region has a high optical absorption coefficient ($\alpha \geq 10^4 cm^{-1}$); it is due to the transition between the valence band and conduction band, according to the Tauc plot [98].

$$\boldsymbol{\alpha h\nu = A'\left(h\nu - E_g\right)^n} \ldots\ldots\ldots\ldots\ldots\ldots\ldots\ldots\ldots\ldots\ldots\ldots\ldots\ldots\ldots\ldots (\mathbf{2-1})$$

whereas :-

A': a constant that depends on the nature of the substance.

E_g: the energy gap.

n: an exponential coefficient is a constant that takes the values (3,2) depending on the type of electronic transitions .

- Exponential Region (part B)

The transition from the extended states in the valence band to the local states in the conduction band or vice versa. The absorption coefficient value in this region ($1 < \alpha < 10^4 cm^{-1}$ is subject to the Urbach relationship [98].

$$\boldsymbol{\alpha = \alpha_0\ e^{\left(\frac{h\nu}{\Delta E_t}\right)}} \ldots\ldots\ldots\ldots\ldots\ldots\ldots\ldots\ldots\ldots\ldots\ldots\ldots\ldots\ldots\ldots\ldots\ldots\ldots\ldots\ldots\ldots (\mathbf{2-2})$$

Where ΔE_t is the Urbach energy.

-Weak Absorption Region (part C)

This region depends on the nature of the material in terms of preparation conditions, purity and thermal history. The absorbance coefficient for this region is very small ($\alpha < 1cm^{-1}$) where there is a weak absorption tail and this region represents the electronic transitions between the tails in the energy gap [98].

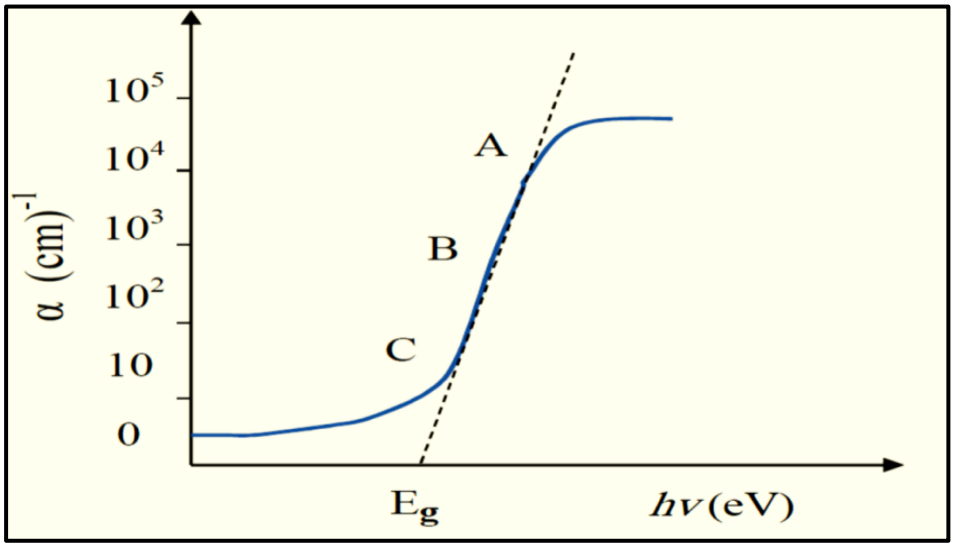

Figure (2.4): The Main Regions of Optical Absorption [98].

2.8.2 Optical Transitions

There are two types of electronic transitions in semiconductors, they are direct and indirect, depending on the location of the highest point at the top of the valence band and the lowest point at the bottom of the conduction band [99].

2.8.2.1 Direct Transitions

A direct transition occurs when the position of the top of the valence band has the same value as the wave vector ($\vec{k}$) for the position of the bottom of the conduction beam, this means that ($\Delta\vec{k} = 0$) and this

transition is accompanied by an interaction between the incident photon and the valence beam electron, and both momentum and energy are conserved. As in the following relationship [100]:-

$$\boldsymbol{E_f - E_i = h\nu} \quad \ldots\ldots\ldots\ldots\ldots\ldots\ldots\ldots\ldots\ldots\ldots\ldots\ldots\ldots\ldots\ldots \quad \mathbf{(2-3)}$$

$$\Delta\overrightarrow{\boldsymbol{k}} = \mathbf{0} \quad \ldots\ldots\ldots\ldots\ldots\ldots\ldots\ldots\ldots\ldots\ldots\ldots\ldots\ldots\ldots\ldots\ldots \quad \mathbf{(2-4)}$$

whereas :-

E_i ,E_f : the initial energy and the final energy of the electron in both the valence and conduction bands, respectively.

$h\nu$:The energy of an absorbed photon.

These transfers are of two types in the case of the allowed direct transition (n =1/2), and in the case of forbidden direct transition (n =3/2).

2.8.2.2 Indirect Transitions

This transition occurs when the energies of the top of the valence band and the bottom of the conduction band do not match in the space of the wave vector ($\overrightarrow{k}$), where the transition from the highest point in the valence band to the lowest point in the conduction band is not perpendicular, so the value of the wave vector will be ($\Delta\overrightarrow{k} \neq 0$). This transition is accompanied by a change in the momentum of the crystal, and this change in the momentum of the crystal is compensated by the lattice either by absorbing a phonon or emitting it in order to achieve the law of conservation of energy and momentum. The absorption equation in this type of semiconductor is given by the following relationship:-

$$\alpha h\nu = A''\left(h\nu - E_g \pm E_p\right)^n \ldots\ldots\ldots\ldots\ldots\ldots\ldots\ldots\ldots\ldots\ldots\ldots\ldots\ldots\ldots\ldots (2-5)$$

A": a constant that depends on the nature of the substance.

E_p: phonon energy.

The (+) sign means phonon emission.

The sign (-) means phonon absorption.

n: Exponential modulus.

These transfers are of two types as well. In the case of the allowed indirect transition (n=2), and in the case of the forbidden indirect transition (n=3). The process of emission or absorption in these transitions depends on the temperature, the opposite of what it is in direct transitions [100], and all transitions are shown in Figure (2.5).

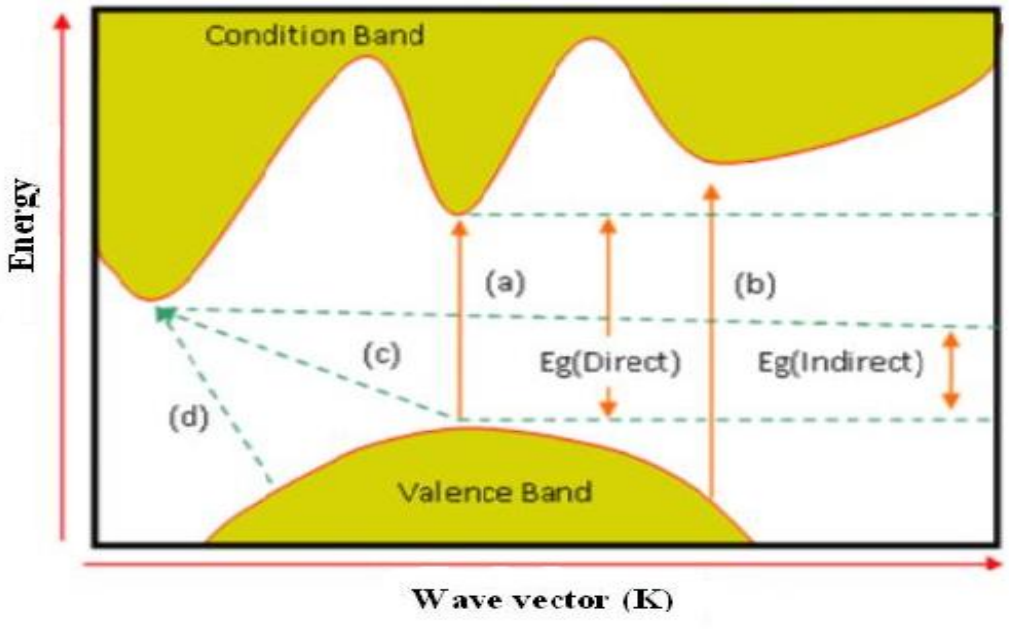

Figure (2.5): (a) Direct Transition is Allowed, (b) Direct Transition is Forbidden, (c) Indirect Transition is Allowed, (d) Indirect Transition is Forbidden [101].

2.9 Optical Constants

2.9.1 Absorption Coefficient (α)

The absorption coefficient (α) of the intensity of light passing through a material, is a factor that expresses the fraction of the beam absorbed per unit thickness of the material. Through the absorption coefficient, it is possible to identify the nature of electronic transitions. If the value of (α) is greater than $(10^4)\text{cm}^{-1}$, this means that direct electronic transitions occur between the valence and conduction bands, but if (α) is less than (10^4) cm^{-1}, this means the occurrence of indirect electronic transmissions. The Beer-Lambert law states that the amount of absorbed light is proportional to the number of molecules absorbing it, if radiation enters a specific solution, the amount of absorbed or transmitted rays is an exponential function of the concentration of the solution (dissolved). According to the Beer-Lambert law, the absorption coefficient can be found through the following relationship [102]:-

$$\boldsymbol{I = I_0 \exp(-\alpha\, t) \ldots\ldots\ldots\ldots\ldots\ldots\ldots\ldots\ldots\ldots\ldots\ldots\ldots\ldots\ldots\ldots\ldots\ldots..(2-6)}$$

whereas :

t: Thin film thickness .

α: material absorption coefficient (cm^{-1}).

The ratio (I/I_o) is called transmittance and after simplifying equation (2-6), we get:

$$\boldsymbol{\alpha = 2.303\ \mathrm{Log}\ (I_0/I)/t \ldots\ldots\ldots\ldots\ldots\ldots\ldots\ldots\ldots\ldots\ldots\ldots\ldots\ldots.\ldots(2-7)}$$

The magnitude (I_o/I) represents the absorbance of the film material (A), which represents the decrease in the energy falling on the thin film. Therefore, equation (2-7) can be written in the following form:

$$\alpha = 2.303\frac{A}{t} \quad \dots\dots\dots\dots\dots\dots\dots\dots\dots\dots\dots\dots\dots\dots\dots\dots\dots\dots\dots\dots\dots\dots.\dots(2-8)$$

whereas :

A: Absorbance of the film material.

t: Thin film thickness .

2.9.2 Transmittance

The ratio (I/I_0) is known as transmittance (T), which is the ratio between the intensity of the transmitted light ray (I) to the intensity of the incident ray (I_0), and it is given by the following relationship [103]:

$$T = \frac{I}{I_0} = e^{-\alpha t} \quad \dots\dots\dots\dots\dots\dots\dots\dots\dots\dots\dots\dots\dots\dots\dots\dots\dots\dots\dots\dots\dots(2-9)$$

Where (t) is the thickness of the material (cm) and (α) is the absorption coefficient (cm^{-1}).

Reflectivity (R) and absorbance (A) are related to the law of conservation of radiation energy [104].

$$R + T + A = 1 \quad \dots\dots\dots\dots\dots\dots\dots\dots\dots\dots\dots\dots\dots\dots\dots\dots\dots\dots\dots\dots\dots\dots(2-10)$$

2.9.3 Extinction Coefficient

It represents the imaginary part of complex refractive index (n*) [105]:

$$n^* = n - ik_o \quad \dots\dots\dots\dots\dots\dots\dots\dots\dots\dots\dots\dots\dots\dots\dots\dots\dots\dots\dots\dots\dots..(2-11)$$

Where :

n: the real part of refractive index , equal (c/v).

c: velocity of light in space

v: velocity of light in matter.

n*: complex refractive index which depends on the material type, crystal structure (grain size), crystal defects, stress in the crystal and extinction coefficient (k), is given by following equation [106]:

$$\boldsymbol{K_\circ = \frac{\alpha\,\lambda}{4\,\pi}} \ldots\ldots\ldots\ldots\ldots\ldots\ldots\ldots\ldots\ldots\ldots\ldots\ldots\ldots\ldots\ldots\ldots\ldots\ldots\ldots\ldots\ldots\ldots\ldots\ldots\ldots\ldots\ldots\ldots \mathbf{(2-12)}$$

Where:

λ : is the wavelength of incident photon rays.

α : absorption coefficient .

2.9.4 Dielectric Constant

When a light incident on the atoms in the material, a reaction between incident radiation and the charges of the material will happen. This will lead to a polarization of the charges of the material [107]:

$$\boldsymbol{\varepsilon = \varepsilon_1 - i\varepsilon_2} \ldots\ldots\ldots\ldots\ldots\ldots\ldots\ldots\ldots\ldots\ldots\ldots\ldots\ldots\ldots\ldots\ldots\ldots\ldots\ldots\ldots\ldots\ldots\ldots\ldots\ldots\ldots\ldots\ldots\ldots \mathbf{(2-13)}$$

Where:

ε_1: is the real part of the complex dielectric constant.

ε_2: is the imaginary part of it. For the calculation of the dielectric constant in its two parts, one can use the following expressions [107]:

$$\boldsymbol{\varepsilon_1 = n_o^2 - k_o^2} \ldots\ldots\ldots\ldots\ldots\ldots\ldots\ldots\ldots\ldots\ldots\ldots\ldots\ldots\ldots\ldots\ldots\ldots\ldots\ldots\ldots\ldots\ldots\ldots\ldots\ldots\ldots\ldots. \mathbf{(2-14)}$$

$$\boldsymbol{\varepsilon_2 = 2\,n_o\,k_o} \ldots\ldots\ldots\ldots\ldots\ldots\ldots\ldots\ldots\ldots\ldots\ldots\ldots\ldots\ldots\ldots\ldots\ldots\ldots\ldots\ldots\ldots\ldots\ldots\ldots\ldots\ldots\ldots. \mathbf{(2-15)}$$

2.10 Electrical Properties (Hall Effect)

The Hall effect is defined as the difference in the distribution of current in a metal sheet due to a magnetic field, and this phenomenon is one of the important phenomena in knowing the type of charge carriers, their density, and the mobility of these carriers [108]. The mechanism of the Hall effect depends on applying a magnetic field (B_z) on the semiconductor in a direction perpendicular to the direction of flow of electric current (I_x) in it. The current and the magnetic field are called the Hall Voltage V_H [109]. The Hall coefficient from equation (2-16) was used. Figure (2.6) illustrates the Hall phenomenon. Through the study of the Hall Effect, determine carrier concentration, carrier type, and the mobility of semiconductor material from the following relationships [110]:

$$\boldsymbol{R_H = \frac{V_H}{I_x} . \frac{t}{B_z}} \dots\dots\dots\dots\dots\dots\dots\dots\dots\dots\dots\dots\dots\dots\dots\dots\dots\dots. \boldsymbol{(2-16)}$$

$$\boldsymbol{R_H = \frac{-1}{n.q}} \quad (n - type) \dots\dots\dots\dots\dots\dots\dots\dots\dots\dots\dots\dots\dots. \boldsymbol{(2-17)}$$

$$\boldsymbol{R_H = \frac{+1}{p.q}} \quad (p - type) \dots\dots\dots\dots\dots\dots\dots\dots\dots\dots\dots\dots\dots. \boldsymbol{(2-18)}$$

$$\boldsymbol{\mu_H = \sigma \, |R_H|} \dots\dots\dots\dots\dots\dots\dots\dots\dots\dots\dots\dots\dots\dots\dots\dots\dots\dots. \dots \boldsymbol{(2-19\,)}$$

Where (B) the intensity of the magnetic field, (I) the current passing through the conductor, (n) the concentration of charge carriers, (e) the charge of electrons.

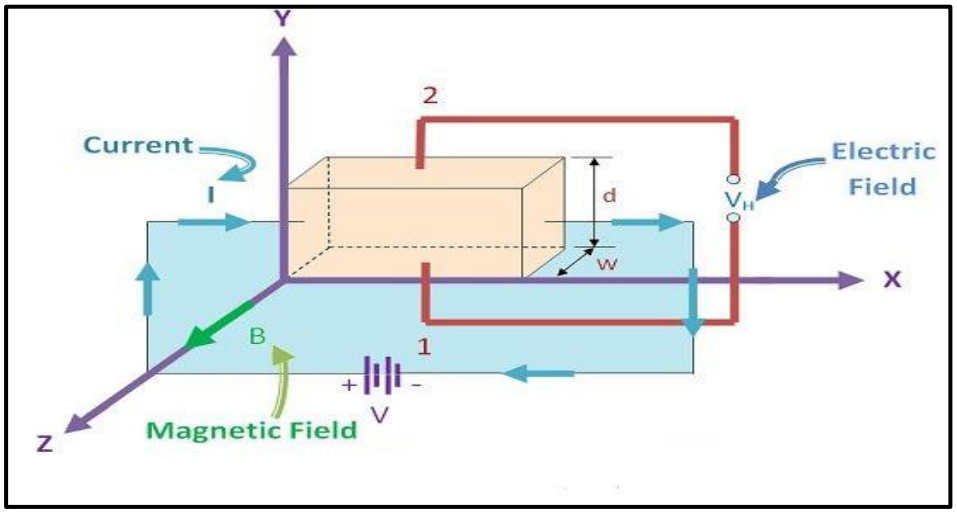

Figure (2.6) :The Electric Circuit to Measure the Impact of the Hall [111].

2.11 Heterojunction

A heterojunction is formed when two semiconductors with varying energy gap values (E_g), work function (Φ_m), dielectric constant (ε_s), and lattice constants are brought together. On the other hand, a homojunction is a junction between two semiconductors that share similar energy gap values, work function (Φ_m), dielectric constant, and lattice constants, but differ in carrier type.

2.12 Detectors

The detector absorbs electromagnetic radiation and sends out an electrical signal that is generally proportional to the electromagnetic radiation intensity depending on the type of detector and how it works; the output signal may be either a voltage or a current [112]. There are two essential detectors classified according to detection mechanism, photonic and thermal detectors:

2.12.1 Thermal Detectors

These detectors depend on the thermal effect as the absorbing thermal ray stimulates the motion of the molecules to cause an increase in the temperature of the absorbent medium, thus the physical properties change of the detector. The thermal detectors have the distinguish that respond to all wavelengths equally, as shown in the Figure (2.7). The advantage of thermal detectors is their response to long wavelengths at room temperature [113].

2.12.2 Photonic Detectors

This detector converts photons directly into free current carriers, When light falls on the detector the photons excite the electrons to higher energy levels leading to forming electrical charge carriers (e or h) that remain inside the detector material. The incident photon must have energy equal to or greater than band gap energy to excite valence electrons, the longest wavelength that can be absorbed is specific by cut-off wavelength ($\lambda_{\text{cut off}}$) given by Planck's equation [113]:

$$\boldsymbol{\lambda_{cut\,off} = \frac{1.24}{E_g(eV)}} \quad \ldots\ldots\ldots\ldots\ldots\ldots\ldots\ldots\ldots\ldots\ldots\ldots\ldots\ldots\ldots\ldots\ldots\ldots\ldots\ldots\ldots\ldots\ldots.\ldots \boldsymbol{(2-20)}$$

These reagents are characterized by having a spectral response within a specified range of wavelengths depending on the type of reagent and have a short response time therefore, these reagents are preferred over thermal detectors because of their high detectivity and response time is shorter than thermal reagents and does not require cooling [113].

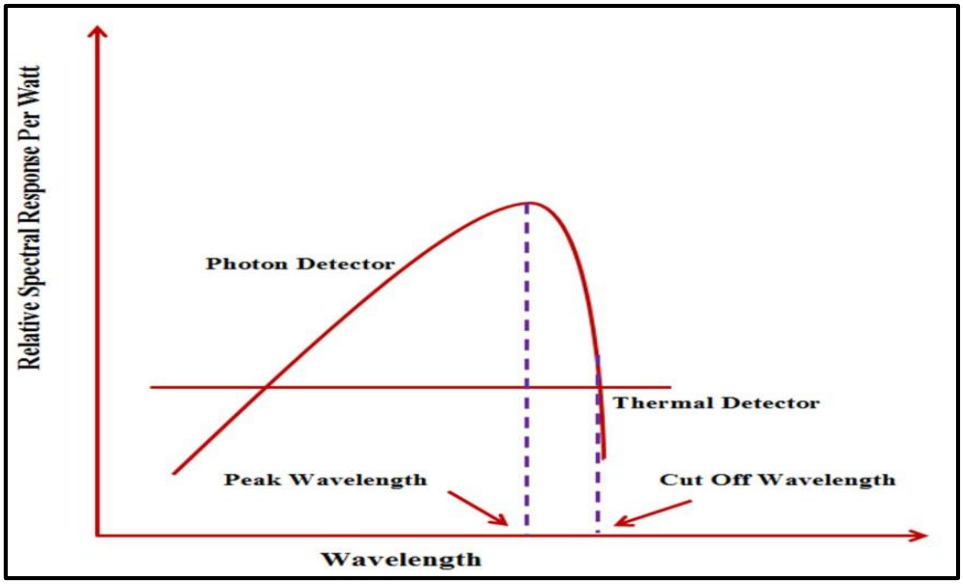

Figure (2.7): The Ideal Spectral Response for Thermal and Photon Reagents [112].

2.13 The Detectors Parameters

2.13.1 The Spectral Responsivity (R_λ)

It is the ratio between the output quantity current or voltage from the detector to the power of the incident radiation. As in the relationship [112]:

$$\boldsymbol{R_\lambda = \frac{I_{photocurrent}}{P_{input}}\ (A/W)\ \ or\ \frac{V_{photovoltge}}{P_{input}}\ (V/W) \dots\dots\dots (2-21)}$$

2.13.2 Detectivity

It is the lowest incident power detected by the detector or is the inverse of the noise equivalent power [114]:

$$\boldsymbol{D_\lambda = \frac{1}{NEP} = \frac{R_\lambda}{I_n}\quad (Watts^{-1}) \dots\dots\dots\dots\dots\dots\dots\dots\dots\dots\dots\dots\dots (2-22)}$$

I_n : Total noise current

Noise Equivalent Power (NEP) defined, as incident power is required to produce a signal voltage or current equal to the noise voltage or current at the detector output. Detectivity increases when NEP decreases [114]:

$$\boldsymbol{NEP = \frac{I_n}{R_\lambda}} \quad (\boldsymbol{Watts}) \ldots\ldots\ldots\ldots\ldots\ldots\ldots\ldots\ldots\ldots\ldots\ldots\ldots\ldots\ldots\ldots\ldots\ldots (\boldsymbol{2-23})$$

The term detectivity is replaced by specific detectivity (D*) used to compare types of reagents and is known by relationship [114].

$$\boldsymbol{D^* = \frac{\sqrt{A\,.\Delta f}}{NEP}} \qquad (\boldsymbol{cm.Hz})^{\boldsymbol{1/2}}\,.\boldsymbol{W^{-1}} \ldots\ldots\ldots\ldots\ldots\ldots\ldots\ldots\ldots\ldots\ldots (\boldsymbol{2-24})$$

$$\boldsymbol{D^* = R_\lambda \frac{\sqrt{A\,.\Delta f}}{I_n}} \qquad (\boldsymbol{cm.Hz})^{\boldsymbol{1/2}}\,.\boldsymbol{W^{-1}} \ldots\ldots\ldots\ldots\ldots\ldots\ldots\ldots\ldots\ldots (\boldsymbol{2-25})$$

$$\boldsymbol{I_n = (2qI_d\Delta f)^{1/2}} \ldots\ldots\ldots\ldots\ldots\ldots\ldots\ldots\ldots\ldots\ldots\ldots\ldots\ldots\ldots\ldots\ldots\ldots (\boldsymbol{2-26})$$

Where:

Δf: The bandwidth

A: Active area of the detector

I_d: Dark current

q: Electron charge.

2.13.3 Quantum Efficiency

It is the ratio between the number of electron-hole pairs (EHP'S) generated to the total number of absorbed photons [115]. The quantum efficiency is essentially another way of expressing the effectiveness of the incident optical energy for producing an output of electrical current, it may be related to the responsivity by the equation [116]:

$$\eta_{quantum} = \frac{R \times 1.24}{\lambda_{(\mu m)}} \times 100\% \ldots\ldots\ldots\ldots\ldots\ldots\ldots\ldots\ldots\ldots\ldots\ldots\ldots (2-27)$$

2.14 Principle of the Solar Cell or Photovoltaic

Photovoltaic (PV) or solar cells are p-n junction semiconductor devices; that convert sunlight directly into electrical energy. Figure (2.8) shows the mechanism of the photovoltaic. The solar cell principle depends on two parameters, the generation of current through absorbed incident illumination and the loss of charging carriers through recombination mechanisms [117]. The junction is oriented such that sunlight falls on the n-type layer (the window layer). Nearly all photons pass through the n-type layer and are then absorbed in the p-type layer (the absorbed layer). Photons that are absorbed in or that are very near the depletion region produce free charge carriers (e-h) that are available to produce an electric current. In the depletion layer, the electric field drifts electrons to the side of the n-type and holes drifts to the side of the p-type. Contacts on the front and back of the device collect these charge carriers and result in an electric current, this permanent current can be converted into alternating current or stored for other uses [118].

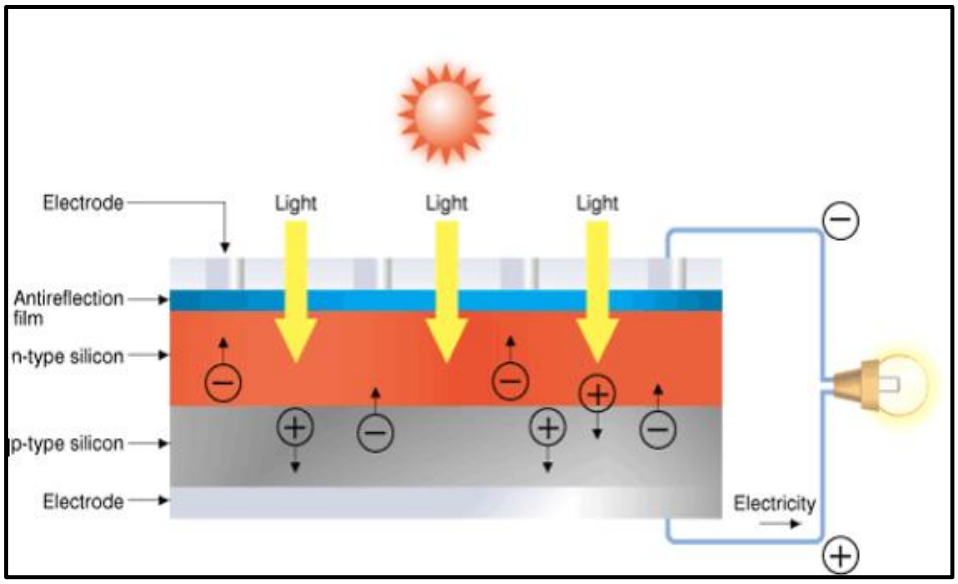

***Figure** (2.8): Mechanism of the Photovoltaic [119].*

Figure (2.9) shows the energy diagram of a heterojunction solar cell. In the dark, the Fermi levels of the semiconductors correspond and there is no current flow as in the case (a). In forward bias, shifts the Fermi level of the n-type semiconductor upwards and that of the p-type semiconductor downwards, thus decreasing the potential energy barrier of the junction and easing the current flow across it as in case (b) while in reverse bias, the barrier increase and the current does not flow as in case(c). Case (d), shows the state illumination of the junction, a pair (e-h) generated causing an increase in the concentration of minority carriers, so the energy of the barrier will decrease and allow the passage of current and a photovoltage V_{OC} generated across the junction [119].

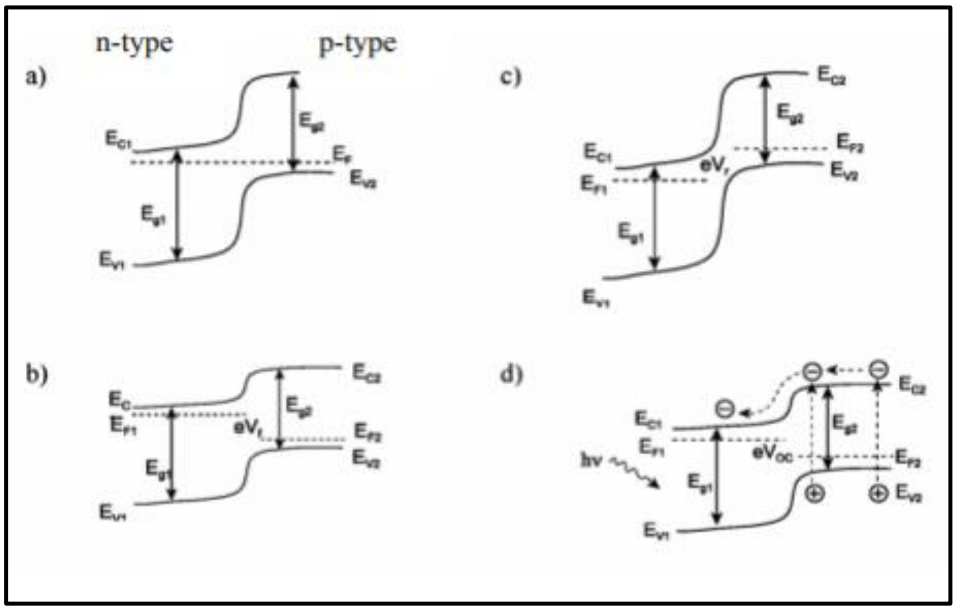

Figure (2.9): Energy band Diagram of a p-n-Heterojunction Solar Cell: (a) under in Dark (Thermal Equilibrium) (b) at Forward Bias (c) at Reverse Bias and (d) under Illumination, Open Circuit Conditions[119].

Solar cells can be categorized into several types based on their manufacturing process [120, 121]. These types include:

a) Homojunction: In a homojunction solar cell, the n-type and p-type layers are made from the same semiconductor material.

b) Heterojunction: Heterojunction solar cells have n-type and p-type layers made from different semiconductor materials.

c) Schottky Junction: A Schottky junction solar cell consists of a combination of a semiconductor and a metal. The Schottky barrier at the junction can function as a solar cell when exposed to light. This type of cell is known for its easy manufacturing process, cost-effectiveness, and high responsiveness to short wavelengths. For effective operation, the metal layer needs to be thin to allow incident light to reach the semiconductor, facilitating the flow of photocurrent.

2.15 Solar Cell Parameter

A photovoltaic cell may be represented by the equivalent circuit model shown in Figure (2.10) [122]. This model consists of current due to optical generation (I_L), a diode that generates a current, a series resistance (R_s), and shunt resistance (R_{sh}). The series resistance is due to the resistance of the metal contacts, ohmic losses in the front surface of the cell, impurity concentrations, and junction depth. The series resistance is an important parameter because it reduces both the short-circuit current and the maximum power output of the cell. Ideally, the series resistance should be ($R_s = 0$). The shunt resistance represents the loss due to surface leakage along the edge of the cell or due to crystal defects. Ideally, the shunt resistance should be infinite ($R_{sh}= \infty$) [123]. Four parameters that are very important to describe the performance of a solar cell (open circuit voltage, short circuit current, filling factor and conversion efficiency) can derived from the I-V curve measured under illumination [124].

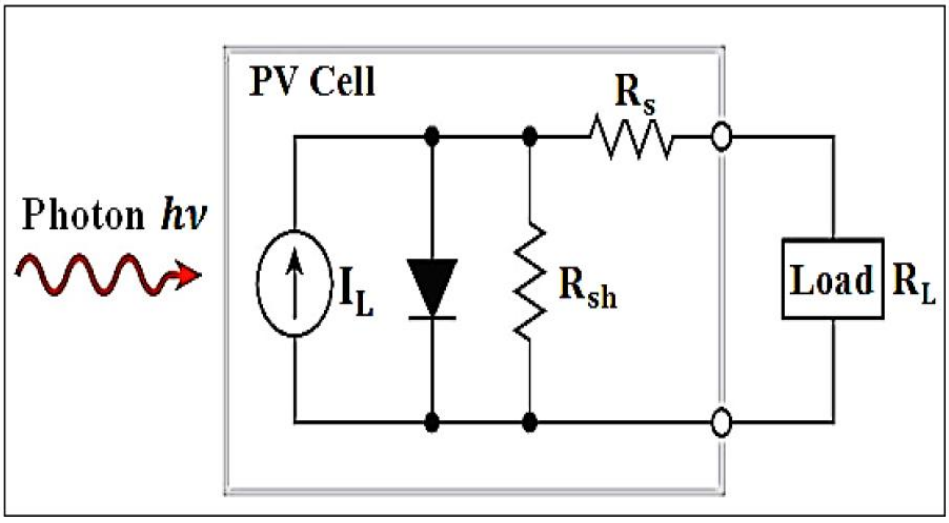

Figure (2.10): Idealized equivalent circuit of a photovoltaic cell [122].

2.15.1 Short-Circuit Current (I_{SC})

The short circuit current I_{sc} is the maximum current that passes through the junction under illumination in the absence of voltage applied and resistance is zero, as in Figure (2.11) [125].

2.15.2 Open-Circuit Voltage (V_{oc})

It is the voltage that passes through the device at zero current (no connected) and the resistance is infinitely [125].

$$V_{o.c} = \frac{k_B T}{q} ln\left(\frac{I_{sc}}{I_0} + 1\right) \ldots\ldots\ldots\ldots\ldots\ldots\ldots\ldots\ldots\ldots\ldots\ldots\ldots\ldots\ldots\ldots\ldots\ldots (2-28)$$

Where (T) is the temperature, (q) is the electron charge, and (I_o) is the reverse saturation current or the dark current.

2.15.3 Fill Factor (F.F)

It is a ratio of the maximum power output of the IV curve divided by the open circuit voltage (V_{oc}) and the short circuit current (I_{SC}). The (F.F) is to give an indication of the quality of the PV cell's semiconductor junction and the recombination losses in space [125].

$$F.F = \frac{P_m}{V_{oc} I_{sc}} \ldots\ldots\ldots\ldots\ldots\ldots\ldots\ldots\ldots\ldots\ldots\ldots\ldots\ldots\ldots\ldots\ldots\ldots\ldots\ldots\ldots\ldots (2-29)$$

The maximum power obtained from the cell can be written by the following relationship:

$$P_m = (V_m * I_m) \ldots\ldots\ldots\ldots\ldots\ldots\ldots\ldots\ldots\ldots\ldots\ldots\ldots\ldots\ldots\ldots\ldots\ldots\ldots\ldots\ldots\ldots (2-30)$$

Where:

I_{sc} : is the short circuit current.

V_{oc} : is open circuit voltage .

I_m: the maximum value of the current.

V_m: the maximum value of the voltages.

2.15.4 Conversion Efficiency

It is the ratio between the maximum output power to the incident power [125].

$$\boldsymbol{\eta = \frac{P_m}{P_{in}} \times 100\ \%} \ldots\ldots\ldots\ldots\ldots\ldots\ldots\ldots\ldots\ldots\ldots\ldots\ldots\ldots\ldots\ldots\ldots\ldots\ldots\ldots\ldots\ldots (\mathbf{2-31})$$

$$\boldsymbol{P_{in} = incident\ Intensity\ (I_{in})\ \times Area\ of\ Cell\ (\ A)} \ldots\ldots.(\mathbf{2-32})$$

where (P_m) is the maximum power, and (P_{in}) is the incident power.

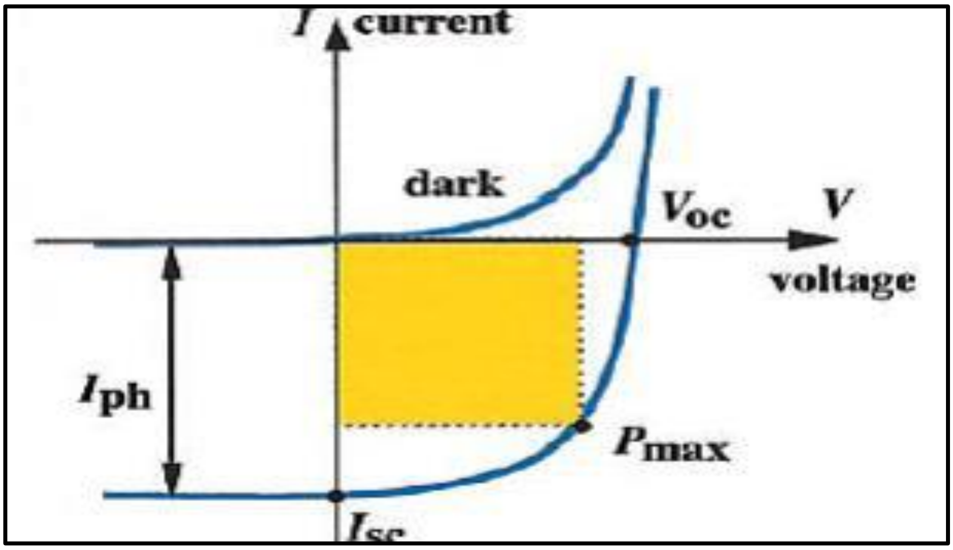

Figure (2.11): Current-Voltage Characteristics of a Solar Cell in Dark and under Illumination [124].

Chapter Three
Experimental Part

3.1 Introduction

This chapter includes the practical aspect from preparing the substrate stage to manufacturing the solar cell thin film and the detector. In addition, it describes all the measurements used to study the properties of prepared films such study the structural and morphological features of X-ray diffraction (XRD), Transmittance Electron Microscope (TEM) and the optical properties, Fourier Transform Infrared (FTIR) spectroscopy. Also, the electrical measurements of the optoelectronic of the detector and solar cell. The schematic diagram of the experimental work and measurements for all samples prepared is shown in Figure (3.1).

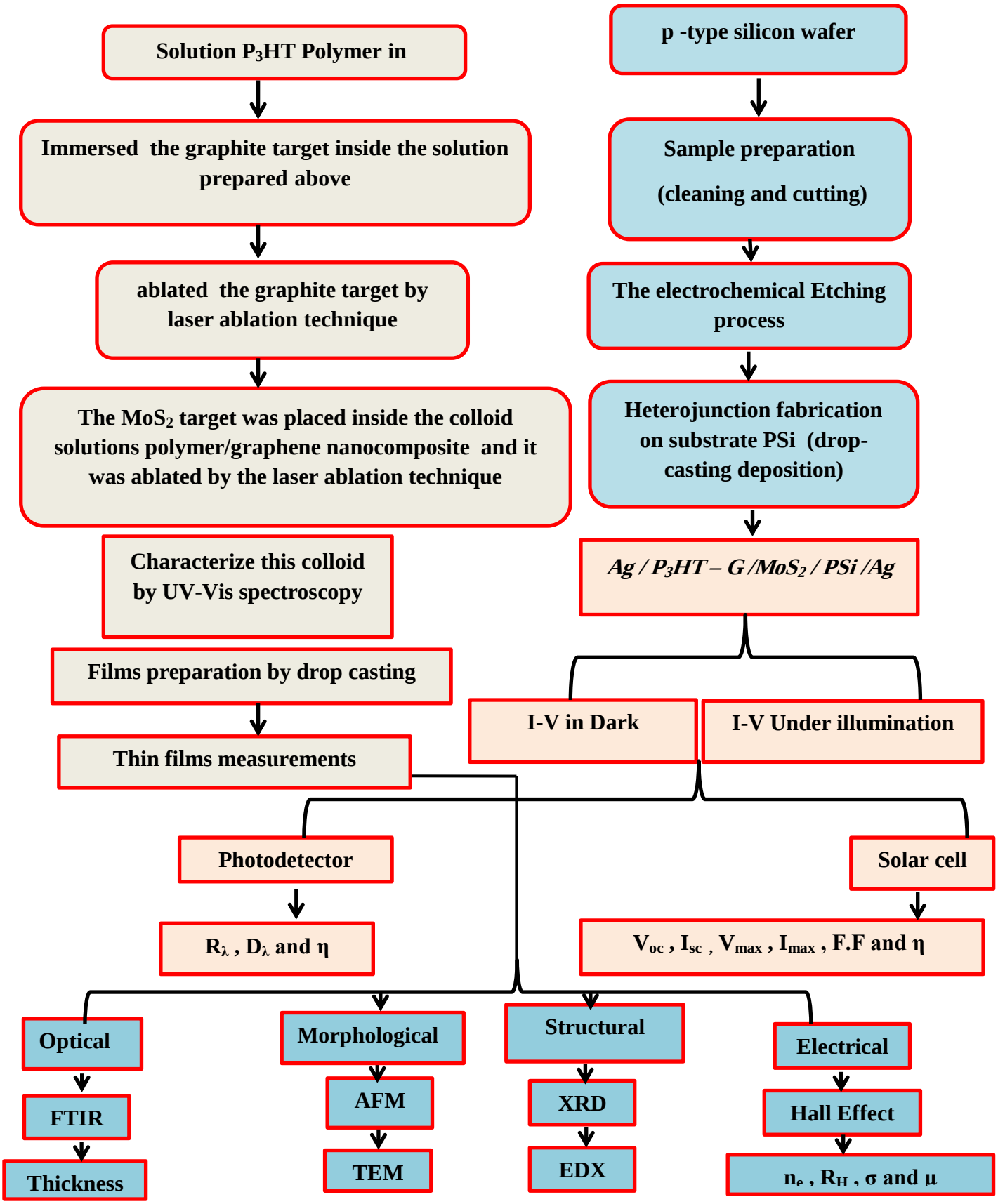

Figure (3.1): Schematic Diagram of the Experimental Work.

3.2 Materials Used

3.2.1 Graphite

Graphite pellet (99.99% quality), with Diameter (2cm), thickness (4mm) and molecular weight (12.01g/mol) was purchased from (Shenzhen Rearth Technology Co. Limited, China).

3.2.2 Molybdenum Disulfide (MoS_2)

MoS_2 pellet (99.99% quality), with Diameter (2cm), thickness (4mm) and molecular weight (160.07g/mol) was purchased from (Shenzhen Rearth Technology Co. Limited, China).

3.2.3 Poly(3-hexylthiophene-2,5-diyl) (P_3HT)

P_3HT polymer powder with molecular weight (16000 g/mol) was purchased from (Shenzhen Rearth Technology Co. Limited, China).

3.3 Substrates

Two types of substrates used in this project, which are described below:

- The glass substrates (2.5cm×2.5cm) are used for optical characteristics. The substrates cleaned with alcohol and rubbed with soft paper.
- Silicon wafer (Si) was chosen p-type with orientation (110) and resistivity (1-10) Ω.cm. Before the nanocomposite deposition, the wafer silicon was cut into small pellets with a suitable size of about (2.5×2.5) cm^2 It is cleaned by immersion in a chemical solution consisting of HF 10% and H_2O for 15 minutes. Then these specimens were rinsed with distilled water several times and dried using soft paper.

3.4 Preparation of P_3HT-G/MoS_2 Nanocomposite Using the Laser Ablation Method

The graphite and molybdenum disulfide (MoS_2) pellets are cleaned with methanol to remove suspended impurities. A semiconducting P_3HT polymer is prepared by dissolving 0.5 mg of P_3HT powder in 40 mL of chloroform solution under a magnetic stirrer for 30 min. The graphite pellet is placed in a clean beaker and immersed with 5 mL of the P_3HT polymer solution, then the graphite pellet is excised using laser pulses (Q-switch Nd-YAG), fundamental wavelength (λ = 1064) nm and energy (E_{pulse} = 200) mJ/pulse, at a repetition rate of (1) Hz, and with pulses (200) pulse. Three samples are prepared with the same previous parameters for a graphite pellet. A molybdenum disulfide (MoS_2) pellet was placed in the P_3HT-G colloidal solutions and excised with the same laser parameters as above but with different laser pulses (200,500 and 800) pulses.

These previous steps are repeated but with different numbers of pulses (200,500 and 800) pulses for graphite and (200) pulse for the MoS_2 pellet. Figure (3.2) shows a schematic of the main stages of pulsed laser ablation in liquid technique (PLAL).

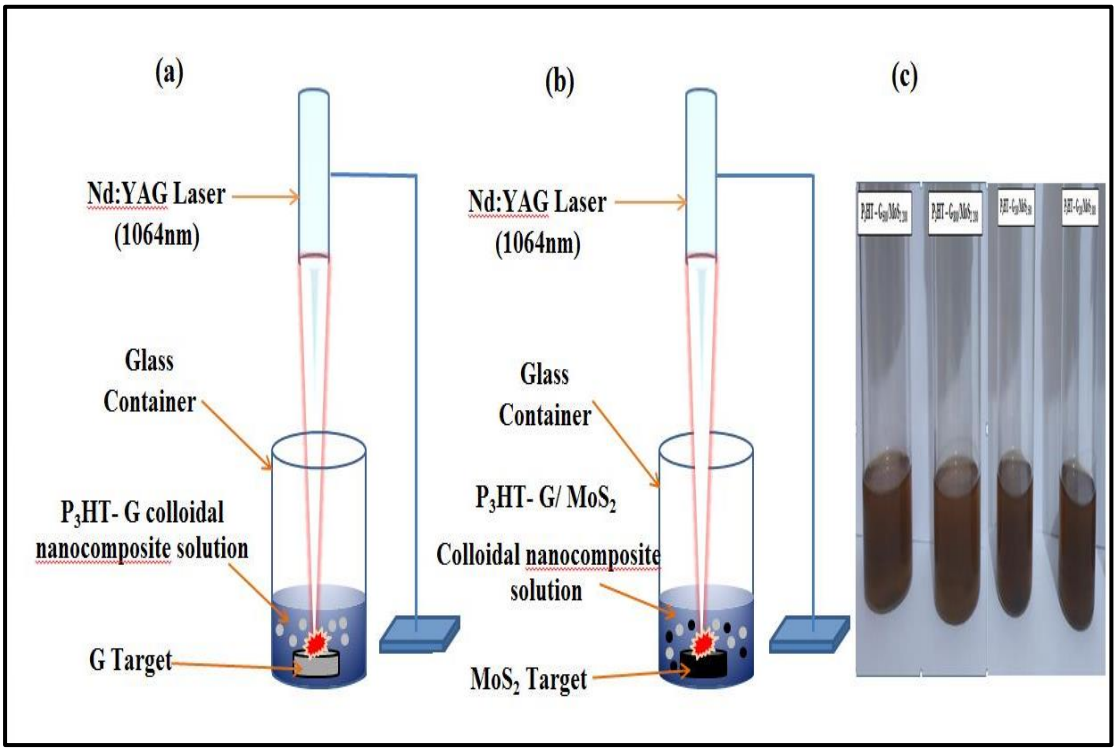

Figure (3.2): Diagram of the main stages of Pulsed Laser Ablation in Liquid Technique (PLAL) ;(a)For graphite target placed in P_3HT polymer solution. (b) placing a target of molybdenum disulfide (MoS_2) in a colloidal nanosolution of P_3HT - graphene. (c) Photograph of the nanocomposite P_3HT - graphene/MoS_2.

3.5 Preparation of Porous Silicon Substrate

Porous silicon (P-Si) layers were prepared by anodic etching with an electrochemical cell in which a substrate with an etched area of (0.785) cm^2 was etched in the teflon etch cell using a 1:1 mixture of ethanol purity 99.99% and aqueous hydrogen fluoride 47% purity. The sample was anodized at a current density of (15) mA/cm^2; for 15 minutes etching time, a thin layer of silver was deposited on the reverse side. Without further heat or chemical treatment, it was made befor engraving. Figure (3.3) shows schematic diagrams of the electrochemical etch setup. This device was prepared and worked on in the laboratories of the College of Science / Al-Mustansiriya University.

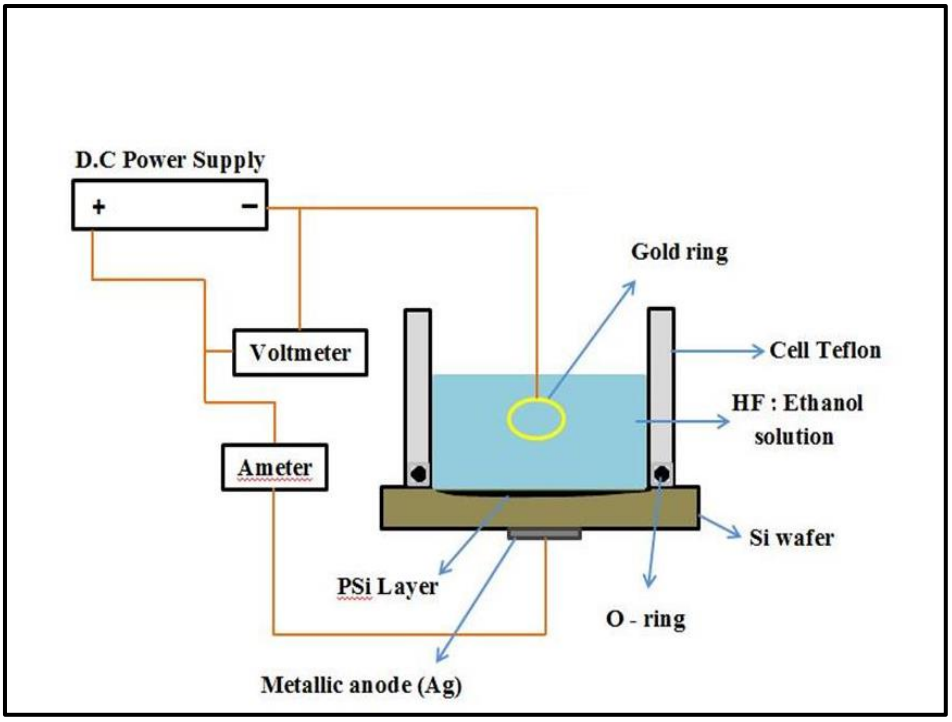

Figure (3.3): Schematic Diagrams of Electrochemical Etching set-up.

3.6 Thin Film Preparation by Drop Casting Method

It is a method to deposition a P_3HT - G/MoS_2 film on the substrate as in Figure (3.4). Drop casting is the best applied to form a diversity of thin films, and allows high productivity and no waste of the materials. nanoparticles are extracted from the solution using a pipette where several drops are dropped on the surface of the substrate at (70) °C and when dry, drops are added again. The process is repeated 3 times, then the film is ready. This device has been prepared and worked on in the laboratories of the College of Science / Al-Mustansiriya University.

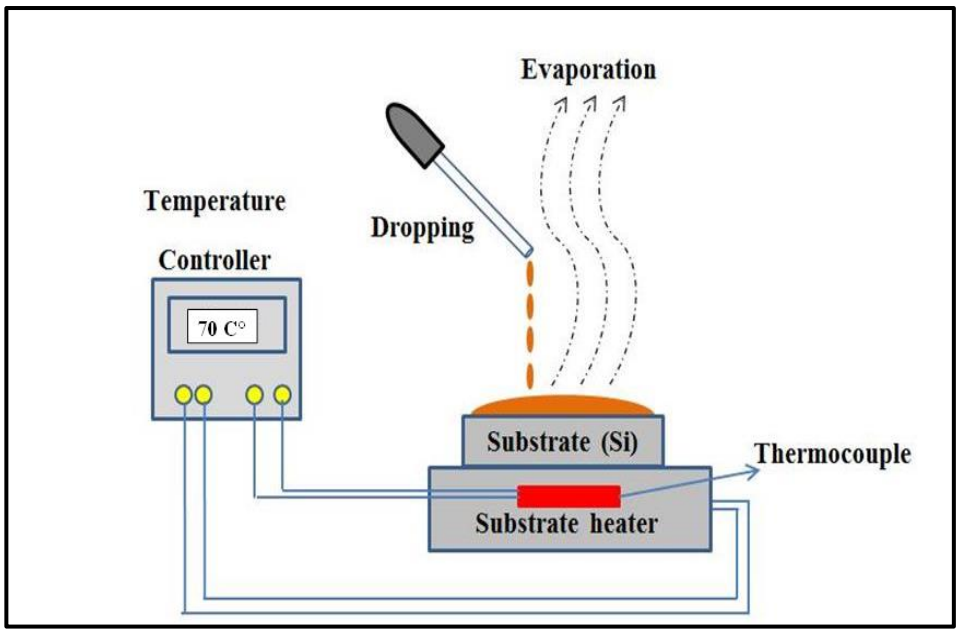

Figure (3.4): Diagram Drop Casting Method.

3.7 Electrodes Deposition

3.7.1 Electrodes Deposition for Hall Effect by Thermal Vacuum

This is done by using a thermal vacuum deposition system under low pressure (10^{-5}) Torr. The schematic diagram of this system is illustrated in Figure (3.5a). Where Aluminum sheets are used as a mask with dimensions (1cm×1cm), and Aluminium wire as the source material.

These masks are placed on films deposited on a glass substrate to depose the Aluminium on the thin film surface of the nanocomposite by using thermal vacuum deposition .The vapours of Aluminium will be deposited on the surface of the substrate after going through the Aluminium sheet mask. The substrate is placed at a distance away from the source with Aaluminium mask consisting of windows with diameters (0.2) cm as in Figure (3.5b). The mask will only allow specific areas of the film to be deposited with the evaporated vapour.

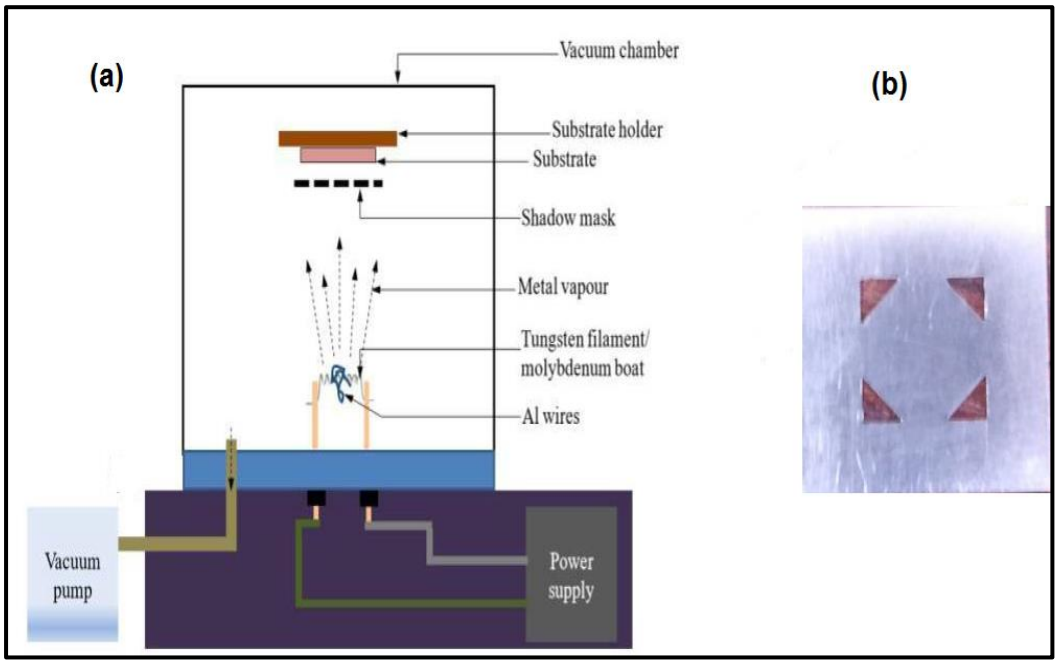

Figure (3.5): (a) Schematic Diagram of Thermal Evaporation System used for Electrode Deposition.(b) Picture the Mask.

3.7.2 Electrodes Deposition and Preparation p-n Junction for Optoelectronic

Using the drop-casting method to deposit the nanocomposite solution onto a silicon (Si) wafer substrate (p-type) for fabricating the p-n junction, and for the electrical measurements of the photodetector and the solar cell, silver paste was used as electrodes on the front surface of the nanocomposite film and on the back side of the silicon substrate as shown in Figure (3.6). Optoelectronic devices are manufactured in with the following architecture:

Ag/Active layer (P_3HT-G/MoS_2)/ PSi/ Ag

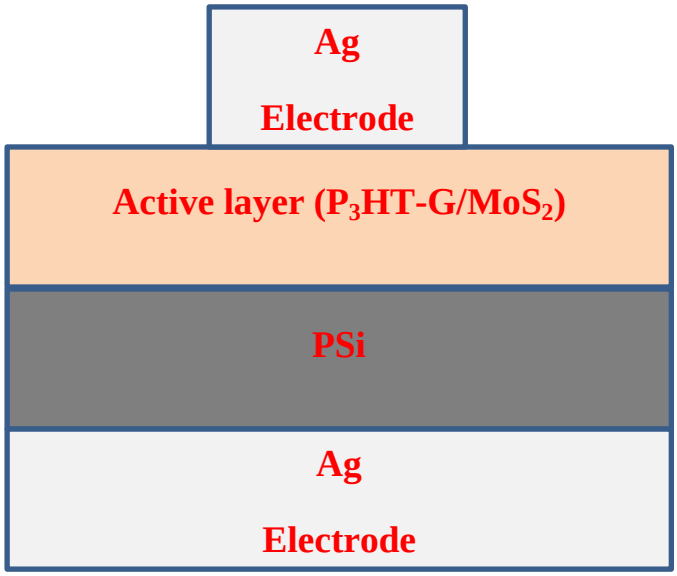

Figure (3.6): Diagram of p-n Junction.

3.8 Optical Measurement

3.8.1 Spectrophotometer(UV-VIS.NIR)

The optical measurements of the nanocomposite are obtained using a spectrophotometer (CECILCE 7200) made by England company, for the wavelength range from 200 to 900 nm. The optical properties are calculated from these optical measurements, Figure (3.7) explains the working principle for the spectrophotometer. The test was conducted in the College of Science for Women/Department of Laser Physics / University of Babylon.

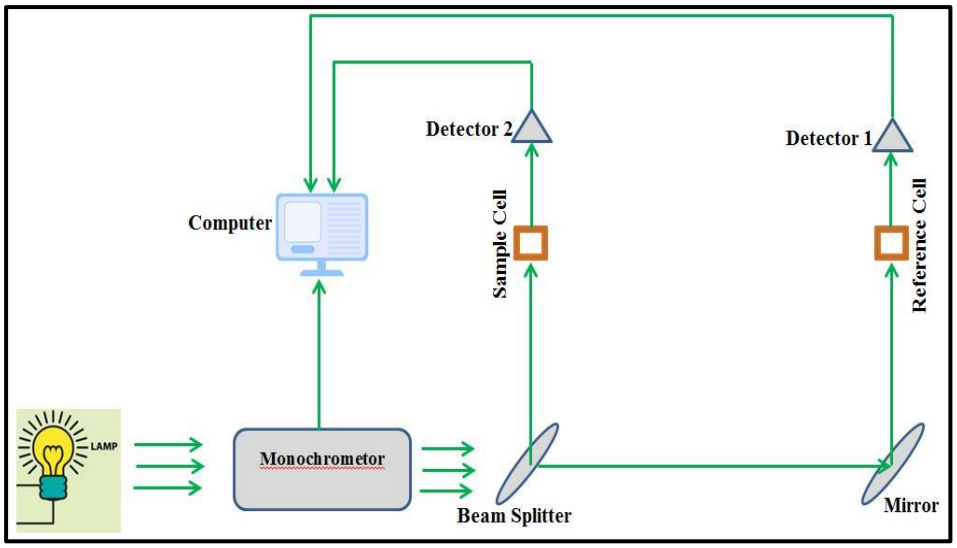

Figure (3.7): The Working Principle of UV-VIS.NIR Spectrophotometer.

3.8.2 Fourier Transform Infrared Spectroscopy (FTIR)

FTIR spectroscopy of the nanocomposite was tested with the Fourier transform infrared spectrophotometer (Shimazdu, IRAffinity-1, Japan) in the 450-4000 cm^{-1} wave number range. The principle of working of an FTIR spectrophotometer involves the use of interferometry and Fourier transforms to obtain the infrared spectrum of a sample. The Fourier-transformed interferogram provides the infrared spectrum of the sample, which displays the absorption or transmission of infrared light at different frequencies. The spectrum contains characteristic absorption peaks that correspond to the vibrational and rotational modes of the sample's molecular bonds. The testing was conducted at of College of Science, University of Baghdad.

3.8.3 Films Thickness Measurement

Ellipsometry is an optical technique to characterize the thickness of thin films and is an analytical technique that measures the change in the polarization of the light after it interacts with a thin film. Components of an ellipsometry (HOLMARC-INDIA): (light source polarized such as a semiconductor laser (λ=532)nm, polarizer, sample stage, analyzer, detector, data analysis system) as shown in Figure (3.8). The sample is placed on a controllable base, and the polarized light is directed onto the surface of the thin film sample at a specific angle of incidence. The light interacts with the film, causing changes in its polarization state due to reflection, refraction, and absorption within the film. After interacting with the film, the light is collected by a detector. The detector measures the change in the polarization state of the reflected light, typically by analyzing the intensity and phase of the light at different polarization angles. The measured change in the polarization state is then analyzed using mathematical models and algorithms to extract information about the thin film properties, such as thickness. The Table (3.1) shows the thickness of all prepared films. The test was conducted in the College of Science for Women / Department of Laser Physics / University of Babylon.

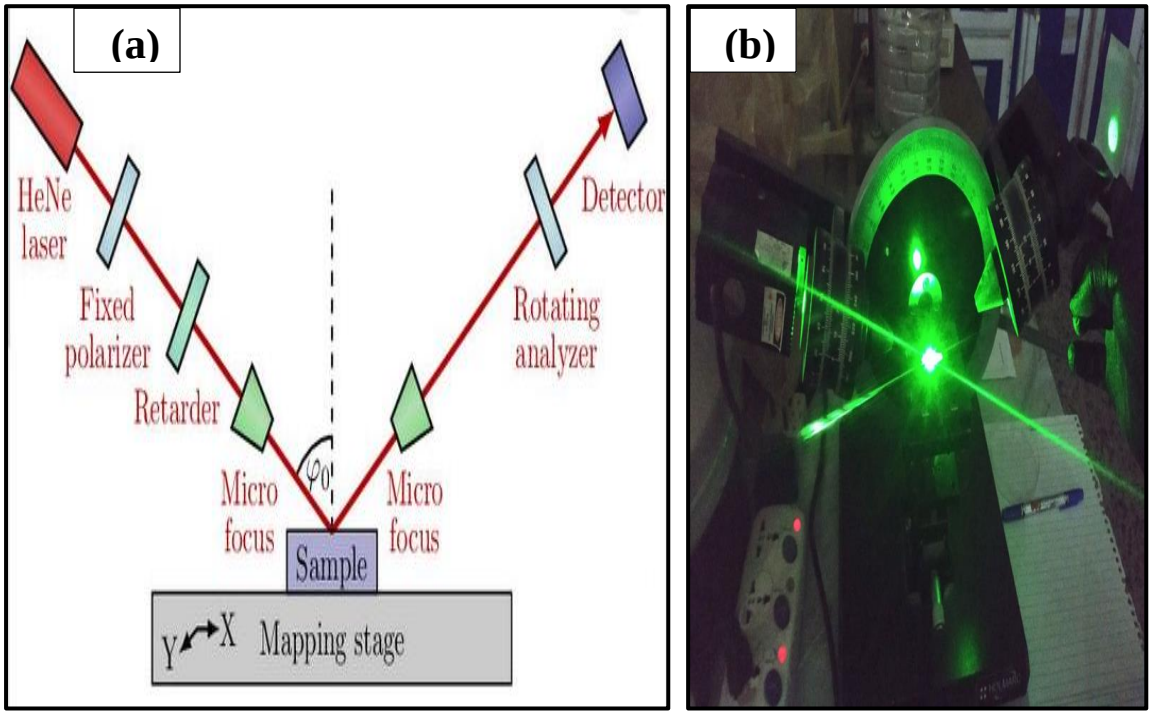

Figure (3.8): (a) Schematic setup of an Ellipsometry Experiment.;(b)Photograph of the Ellipsometry Technique.

Table (3.1): shows the thickness of all prepared films.

Samples	Thickness thin film (nm)
$P_3HT - G_{200P} / MoS_{2\ 200P}$	230
$P_3HT - G_{200P} / MoS_{2\ 500P}$	230.2
$P_3HT - G_{200P} / MoS_{2\ 800P}$	230.1
$P_3HT - G_{500P} / MoS_{2\ 200P}$	230.5
$P_3HT - G_{800P} / MoS_{2\ 200P}$	230.2
$P_3HT - G_{800P} / MoS_{2\ 800P}$	230.8

3.9 The Hall Effect Measurements

Hall effect measurements have been done by the Van der Pauw; model (HMS-3000 Ecopia) with constant current and magnetic field (10nA, 0.55T). Hall measurement is used to determine the type of charge (n-type or p-type), concentration, mobility, Hall coefficient, and resistance. Figure (3.9) shows the electric circuit of the Hall effect. The was conducted at of College of Science, University of Baghdad.

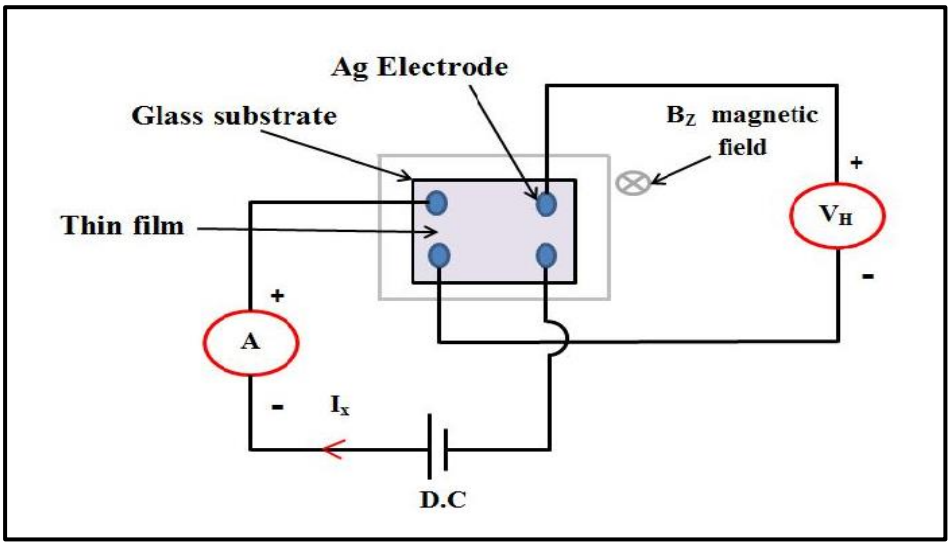

Figure (3.9) :The Electric Circuit of the Hall Effect.

3.10 Structural and Morphological Measurements

3.10.1 X-ray Diffraction (XRD)

The X-ray diffraction technique gives information about the shape, positions and signal intensity of the diffraction planes. Study x-ray diffraction type SHIMADZU" XRD-6000 X-ray, power diffraction system with Cu-Kα x-ray tube (λ = 1.54056 Å) was used. The X-ray scans were performed between 2θ values of (20º-80º) the system works by voltage 40 kV and current 30 mA. The calculation of the average crystallite size can be performed using Scherrer's formula using equation (3-1) [126]:

$$C.S = \frac{k\,\lambda}{FWHM\ cos\theta} \quad \dots\dots\dots\dots\dots\dots\dots\dots\dots\dots\dots\dots\dots\dots\dots\dots\dots\dots (3-1)$$

C.S: Crystallite size (nm).

k: Dimensionless form factor .

FWHM: Full width at half maximum in (radian) unit.

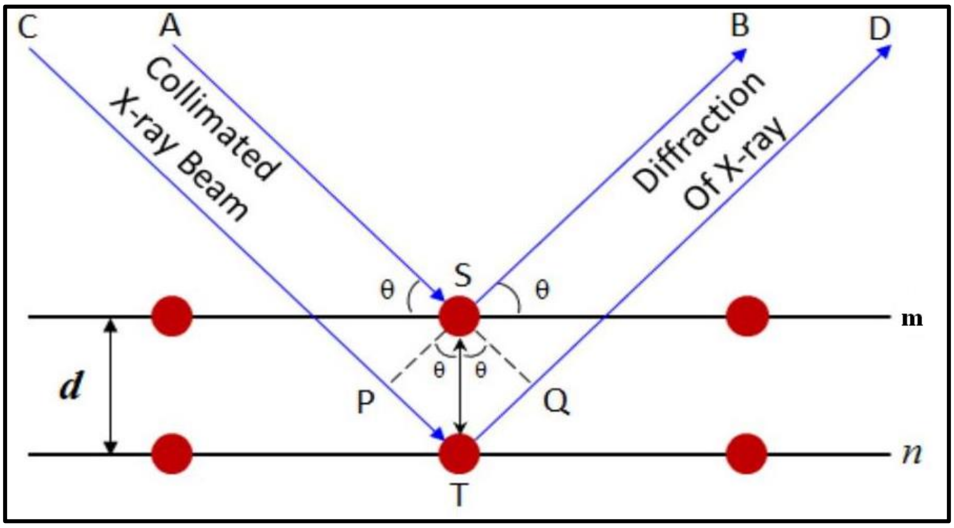

Figure (3.10): General schematic of a Bragg Diffraction [127].

3.10.2 Transmission Electron Microscope (TEM)

transmission electron microscopy is a method that involves passing a focused beam of electrons through an extremely thin sample, leading to interactions with the sample. These interactions generate an image that reflects the sample's characteristics. TEM was employed to determine the diameter of nanoparticles using equation (3-2). The investigation utilizing TEM was conducted using a specific instrument, the (CM10 PW6020 model) from Philips-Germany. The testing was conducted at the University of Tehran in Iran.

$$\boldsymbol{D\ (nm) = \frac{d}{M} \times \frac{3}{4}} \dots\dots\dots\dots\dots\dots\dots\dots\dots\dots\dots\dots\dots\dots\dots\dots\dots..\boldsymbol{(3-2)}$$

Where; (D) nanoparticle diameter, (d) real diameter on image and M magnification of TEM [128].

3.10.3 Scanning Electron Microscopy(SEM)

Scanning electron microscopy (SEM) is basically a type of electron microscopes. The SEM study has been carried out by (model :Jeol JSM-6335F) from Philips-Germany. This device can analyze the energy dispersion of X-rays (EDX) (Model:7353), to obtain information about the elemental composition of a sample and to identify the elements present in the sample and determine their concentrations. The testing was conducted at the University of Tehran in Iran.

3.10.4 Atomic Force Microscope (AFM)

The atomic force microscope (Model: CSPM AA3000) is supplied by Angstrom advanced, to determine the surface morphology and surface roughness of all thin films and their statistical distribution. The test was conducted at of College of Science, University of Baghdad.

3.11 Electrical Measurements for Optoelectronics

3.11.1 Current –Voltage Characteristic under Dark and Light

The electrical circuit as shown in Figure (3.11) was adopted for the measurements of the properties (current-voltage) in the case of the dark and the light for all manufactured solar cells. In the case of the dark, solar cells are placed in a dark chamber and connected to the electric circuit, it is biased forward to measure the bias current by (Keithly 616 Digital Electrometer) with voltage (0-10) Volt. Then reflect the polarity to measure the values of reverse bias current, with voltage (0-10) Volt. In the case of illumination where used for this purpose Halogen lamp (Philips) with a light intensity of the amount (100) mW/cm^2, to measure the values of reverse bias current (I_{ph}), with voltage (0-10) Volt. The testing was conducted at of College of Science, University Al-Mustansiriya.

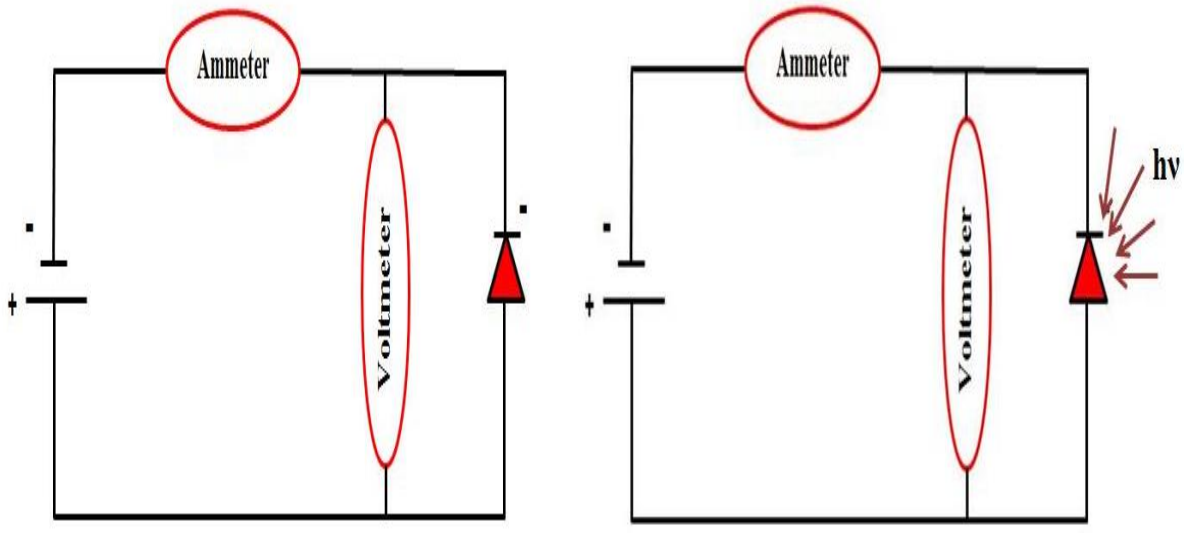

Figure (3.11): Circuit Diagram used to Measure (Voltage –Current) Characteristics (left Dark and right Light).

3.11.2 Measurements of the Photodetector Thin Films

3.11.2.1 Spectral Responsivity (R_λ)

The spectral responsivity measurement using a double-beam UIR-210A spectrophotometer operating within the range (200-1000) nm of wavelengths. The current measurements were performed using a 8010 DMM Fluke digital multimeter. R_λ determined using the equation (2-21). The testing was conducted at of College of Science, University Al-Mustansiriya.

3.11.2.2 Specific Detectivity (D)*

The specific detectivity is determined by the equation (2-25).

3.11.2.3 Quantum Efficiency (η_q)

The quantum efficiency is determined by the equation (2-27).

3.11.3 Measurements of the Solar Cell Thin Films

To complete the properties measurements (current-voltage) in the case of light for all manufactured solar cells, where the power supply is removed and a variable resistance is placed instead to determine the parameters of the solar cell, the voltage of the open circuit (V_{oc}), the short circuit current (I_{sc}) as shown by Figure (3.12). Thus can be calculated the filling factor (F.F) and the photovoltaic efficiency of the solar cell by equations (2-29, 2-31) respectively.

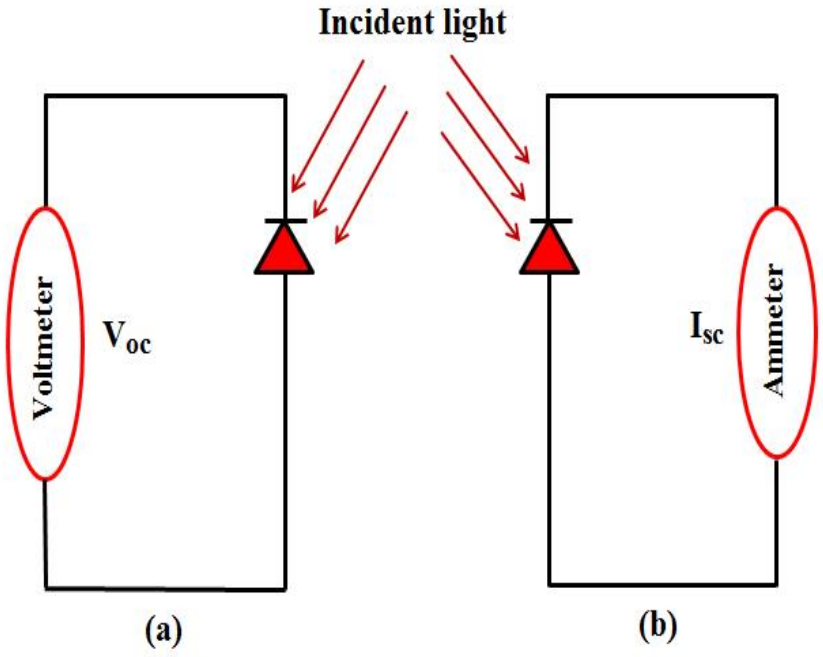

Figure (3.12): (a) Open-Circuit Voltage. (b) Short-Circuit Current.

Chapter Four

Results & Discussion

4.1 Introduction

In this chapter, all the experimental data obtained for this research are presented and discussed. The results showed studied the optical properties of the P_3HT-G/MoS_2 nanocomposite such as optical absorption, absorption coefficient (α). The study discusses crystal structure (XRD), surface topography (AFM) and electrical properties for all thin films of the P_3HT-G/MoS_2 nanocomposite, and the results of (I-V) characteristics in the dark and illumination for solar cell and photodetector.

4.2 Structural and Surface Morphology Measurements

4.2.1 X-ray Diffraction Analysis (XRD)

The prepared samples' X-ray diffraction (XRD) pattern was analyzed, and the results are presented in Figure (4.1). The peaks observed at 2θ = 14.4° and 2θ = 33.2° correspond to the (002) and (101) planes, respectively, of MoS_2 which is in agreement with previously reported literature data (JCDPS Card No: 1317-33-5) [129]. Similarly, the peaks observed at 2θ = 26.2° and 2θ = 44.6° correspond to the (002) and (101) planes, respectively, of graphene, which is in agreement with previously reported literature data (JCDPS Card No: 89-7213) [130], The absence of a peak at (2θ =10°), which belongs to graphene oxide, is evidence that a conversion from graphene oxide to graphene, i.e., a reduction in oxygen has occurred. Also observed The P_3HT (010) peak at 2θ = 23.4°, is the most intense peak in the X-ray diffraction pattern of P_3HT because it is the most sensitive to the stacking of the polymer chains in the crystal lattice [131]. It is worth noting that an increase in the

number of pulses of graphene (G) led to an increase in the intensity of the peaks observed at (2θ = 26.2°, 44.6°), (2θ = 26.4°, 44.6°) and (2θ = 26.2°, 44.7°) for P_3HT-G_{200P}/$MoS_{2\ 200P}$, P_3HT-G_{500P}/$MoS_{2\ 200P}$, and P_3HT-G_{800P}/$MoS_{2\ 200P}$, respectively. Similarly, an increase in the number of pulses of MoS_2 led to an increase in the intensity of the peaks observed at (2θ = 14.2°, 33.2°), (2θ = 14.4°, 33.4°) and (2θ = 14.6°, 33.2°) for P_3HT-G_{200P}/$MoS_{2\ 200P}$, P_3HT-G_{200P}/$MoS_{2\ 500P}$, and P_3HT-G_{200P}/$MoS_{2\ 800P}$, respectively. The disappearance of the pure P_3HT polymer peak suggests that the GNP_s and MoS_2NP_s successfully penetrated the P_3HT chains, which is supported by the FTIR results that showed the presence of thiophene rings in all the prepared samples. Scherer's method was used to calculate the crystal size of the produced films according to the equation (3-1), and Table (4.1) shows the XRD data for all of the films.

The results reveal that the crystallite size increases with the increase in the number of laser ablation pulses of the G and MoS_2 targets, due to the increasing of concentration both of the GNP_s and MoS_2NP_s.

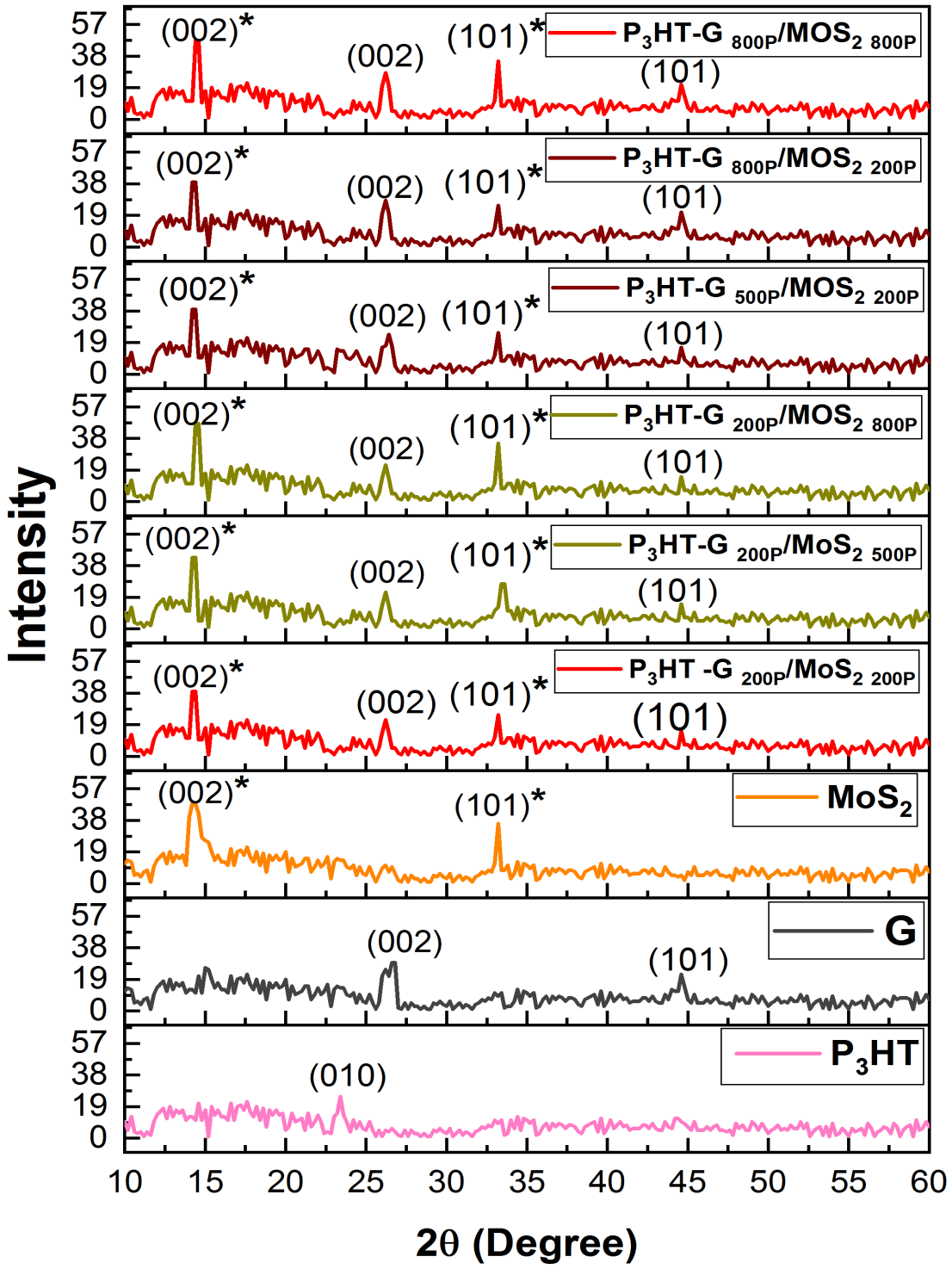

Figure (4.1): The XRD Pattern of all the Prepared Samples; (*) refers to MoS_2 planes.

Table (4.1): The XRD Results for all the Films Prepared.

Samples	2 θ Standard (deg)	2 θ (deg)	hkl Plane	FWHM (deg)	Crystallite size (nm)	Average crystallite Size (nm)
P_3HT	23.5	23.4	(010)	0.689	14	14
G	26.381	26.2	(002)	1.564	5	18
	44.391	44.6	(101)	0.33	31	
MoS_2	14.387	14.2	(002)*	1.056	7	13
	33.508	33.2	(101)*	0.425	19	
$P_3HT - G_{(200P)} / MoS_{2\ (200P)}$	14.387	14.2	MoS_2 (002)*	0.647	14	15
	26.381	26.2	G (002)	0.942	9	
	33.508	33.2	MoS_2 (101)*	0.57	11	
	44.391	44.6	G (101)	0.353	26	
$P_3HT - G_{(800P)} / MoS_{2\ (800P)}$	14.387	14.4	MoS_2 (002)*	0.659	12	19. 5
	26.381	26.2	G (002)	0.941	18	
	33.508	33.2	MoS_2 (101)*	0.58	31	
	44.391	44.6	G (101)	0.364	17	
$P_3HT - G_{(200P)} / MoS_{2\ (500P)}$	14.387	14.4	MoS_2 (002)*	0.657	13	16.75
	26.381	26.2	G (002)	0.391	21	
	33.508	33.4	MoS_2 (101)*	0.689	11	
	44.391	44.6	G (101)	0.376	22	
$P_3HT - G_{(200P)} / MoS_{2\ (800P)}$	14.387	14.6	MoS_2 (002)*	0.663	13	19
	26.381	26.2	G (002)	0.68	14	
	33.508	33.2	MoS_2 (101)*	0.425	19	
	44.391	44.6	G (101)	0.34	30	
$P_3HT - G_{(500P)} / MoS_{2\ (200P)}$	14.387	14.4	MoS_2 (002)*	0.658	13	15.25
	26.381	26.4	G (002)	0.822	11	
	33.508	33.2	MoS_2 (101)*	0.547	14	
	44.391	44.6	G (101)	0.362	23	
$P_3HT - G_{(800P)} / MoS_{2\ (200P)}$	14.387	14.4	MoS_2 (002)*	0.662	13	19
	26.381	26.2	G (002)	0.689	14	
	33.508	33.2	MoS_2 (101)*	0.478	17	
	44.391	44.6	G (101)	0.33	32	

(*) refers to MoS_2 planes.

4.2.2 Atomic Force Microscope (AFM)

The atomic force microscopy (AFM) technique was utilized to investigate the surface topography of (P_3HT-G/MoS_2) nanocomposite deposited on a p-type silicon wafer. The average pore diameter, roughness average (Ra) and root mean square (RMS) values were estimated and tabulated in Table (4.2). It is noteworthy from the table that the highest Ra, RMS and average particle size were observed for the (P_3HT-G_{800P}/$MoS_{2\ 800P}$) sample, with values of 25.27, 20.98 and 100.7 nm respectively. Conversely, the lowest values were recorded for the (P_3HT - G_{200P} /$MoS_{2\ 200P}$) sample, with values of 5.54, 4.116 and 52.77 nm for Ra, RMS and average particle size respectively. Figure (4.2) illustrates 3D images of P_3HT- G/MoS_2 samples prepared with varying laser pulses for graphite and MoS_2 are presented. The results indicate a significant change in the surface topography of the samples, which is attributed to an increase in the number of pulses for both graphite and MoS_2.

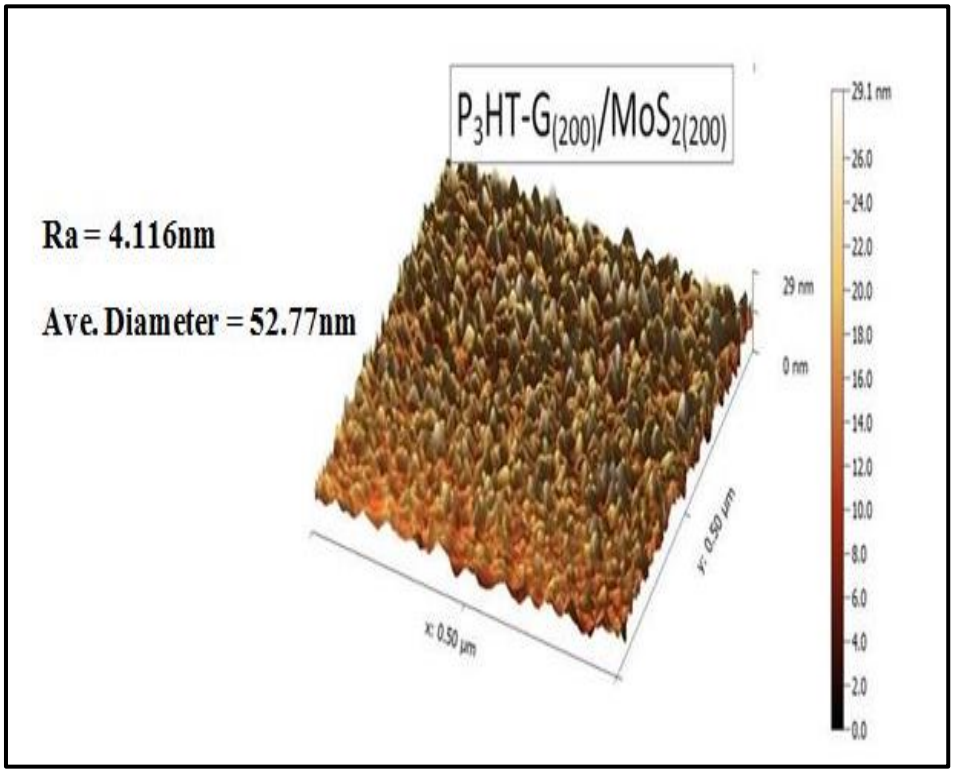

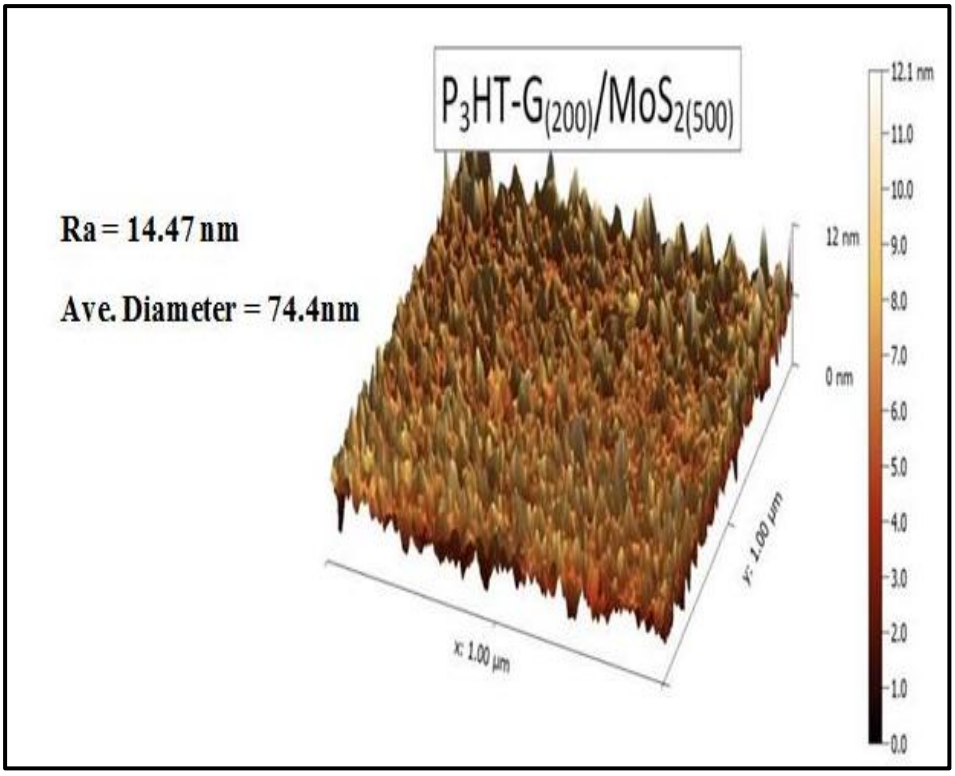
P3HT-G(200)/MoS2(500)
Ra = 14.47 nm
Ave. Diameter = 74.4nm
12.1 nm
11.0
10.0
9.0
8.0
7.0
6.0
5.0
4.0
3.0
2.0
1.0
0.0
12 nm
0 nm
x: 1.00 µm
y: 1.00 µm

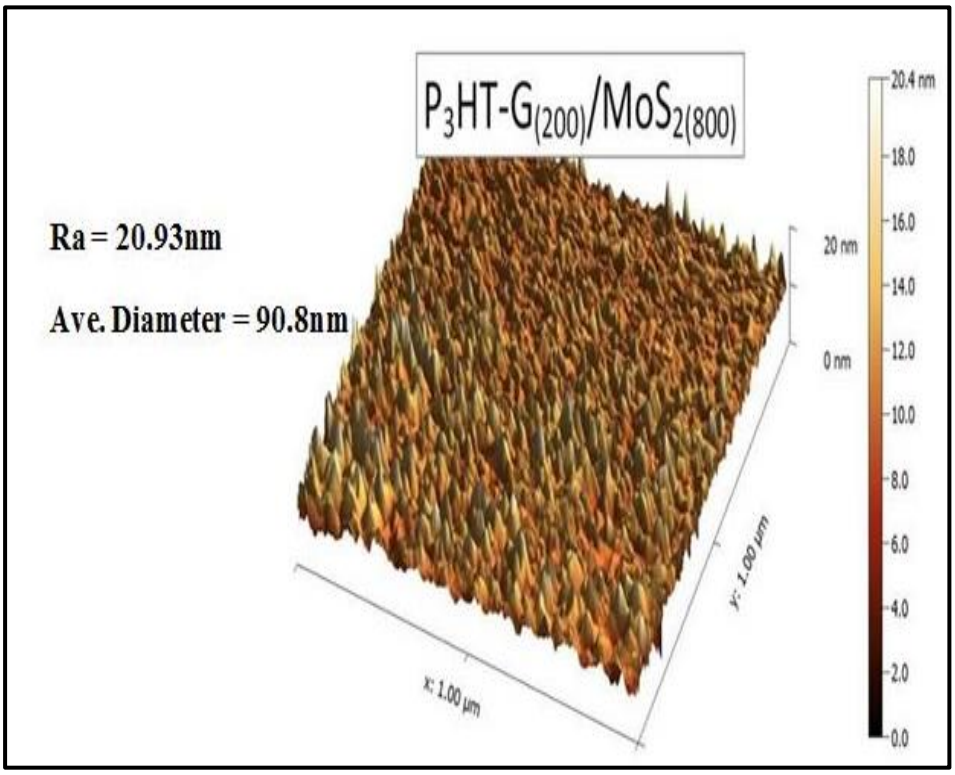
P3HT-G(200)/MoS2(800)
Ra = 20.93nm
Ave. Diameter = 90.8nm
20.4 nm
18.0
16.0
14.0
12.0
10.0
8.0
6.0
4.0
2.0
0.0
20 nm
0 nm
x: 1.00 µm
y: 1.00 µm

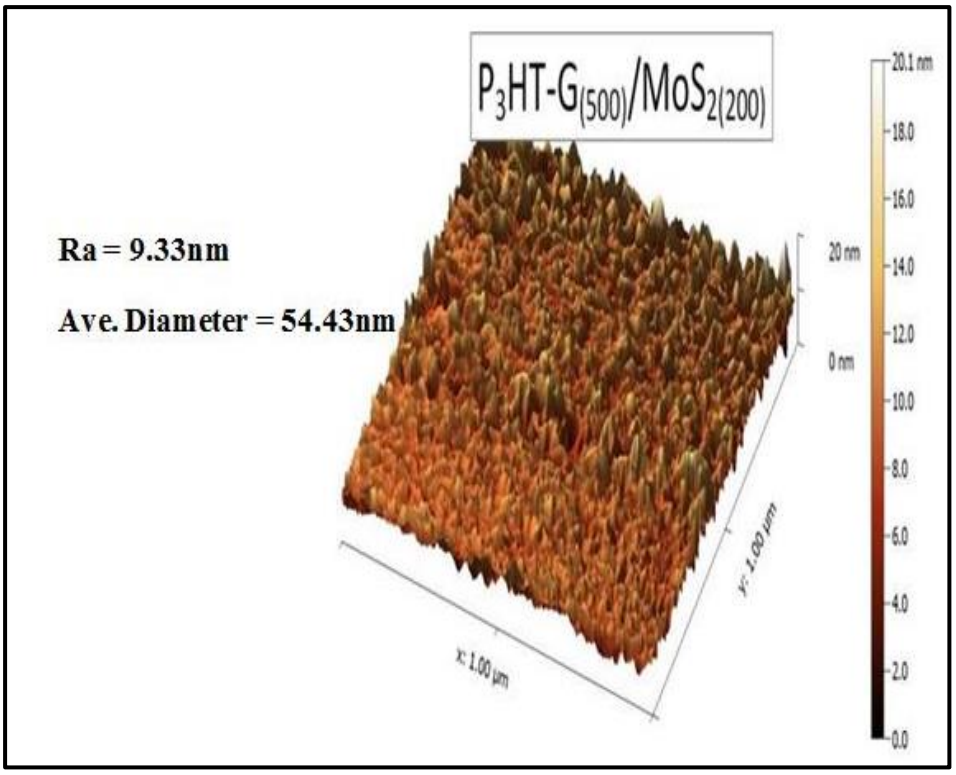
P3HT-G(500)/MoS2(200)
Ra = 9.33nm
Ave. Diameter = 54.43nm
20 nm
0 nm
x: 1.00 µm
y: 1.00 µm
20.1 nm
18.0
16.0
14.0
12.0
10.0
8.0
6.0
4.0
2.0
0.0

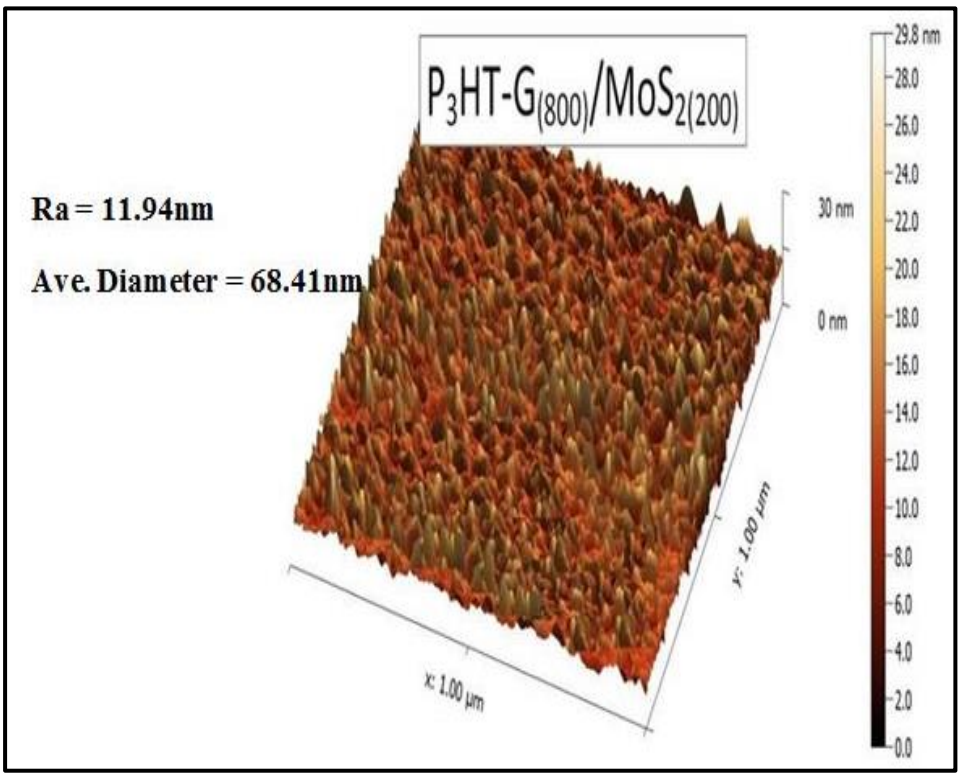
P3HT-G(800)/MoS2(200)
Ra = 11.94nm
Ave. Diameter = 68.41nm
30 nm
0 nm
x: 1.00 µm
y: 1.00 µm
29.8 nm
28.0
26.0
24.0
22.0
20.0
18.0
16.0
14.0
12.0
10.0
8.0
6.0
4.0
2.0
0.0

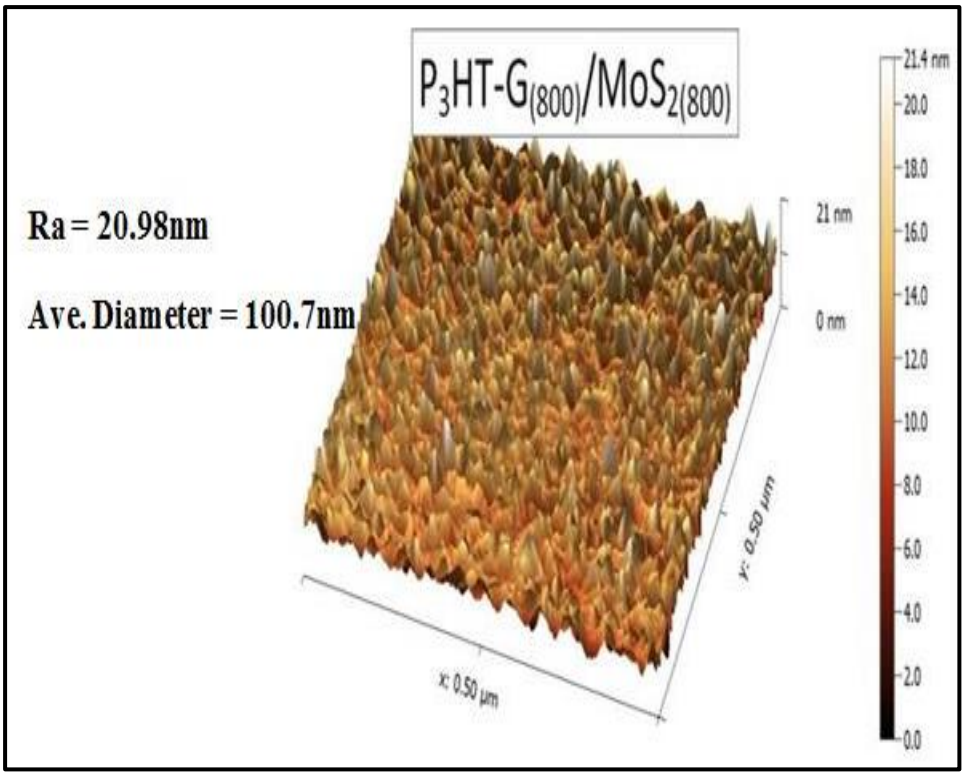

Figure (4.2):AFM Images of (P_3HT - G / MoS_2)Nanocomposits.

Table (4.2): Summarizes the Average Diameter, Ra, and RMS of The (P_3HT - G/ MoS_2) Nanocomposite Prepared On P-type Silicon Wafer.

Samples	RMS (nm)	Ra (nm)	Ave. Diameter (nm)
$P_3HT - G_{200}$ /$MoS_{2\ 200}$	5.54	4.116	52.77
$P_3HT - G_{800}$ /$MoS_{2\ 800}$	25.27	20.98	100.7
$P_3HT - G_{200}$ /$MoS_{2\ 500}$	17.72	14.47	74.4
$P_3HT - G_{200}$ /$MoS_{2\ 800}$	25.92	20.93	90.8
$P_3HT - G_{500}$ /$MoS_{2\ 200}$	11.65	9.33	54.43
$P_3HT - G_{800}$ /$MoS_{2\ 200}$	15.59	11.94	68.41

4.2.3 Transmission Electron Microscopy (TEM)

TEM was used to analyze the morphological aspects of the nanocomposites. Figures (4.3-4.8) shows TEM images of the P_3HT-G/MoS_2 nanocomposite with a 50 nm scale, revealing various regions with diameters ranging from 3.17 to 20.67nm. The images indicate that the G and MoS_2 nanoparticles have a semispherical shape, which is consistent with the findings of reference [132].

Some TEM images show that the nanoparticles coalesce to form a larger spherical particle. This phenomenon may result from several factors, including the small size of the particles and their interactions with the electron beam. When a sample is exposed to an electron beam in TEM, the electrons can interact with the atoms in the sample, causing changes in the morphology and structure of the sample. On the other hand, some TEM images clearly exhibit the core-shell effect in the P_3HT-G/MoS_2 nanocomposite.

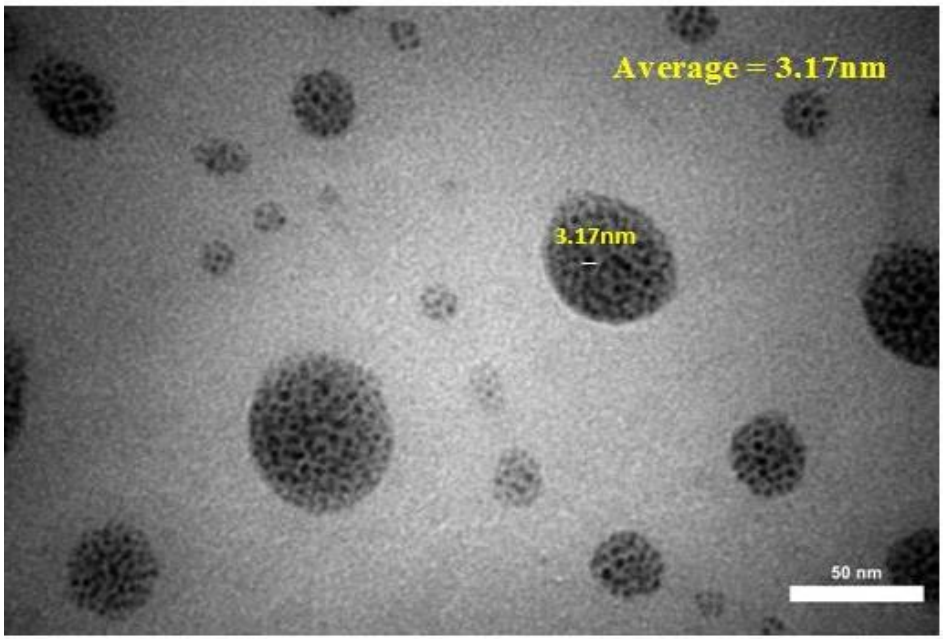

Figure (4.3):TEM Image of P_3HT-G_{200P}/$MoS_{2\ 200P}$ Colloidal Nanoparticles.

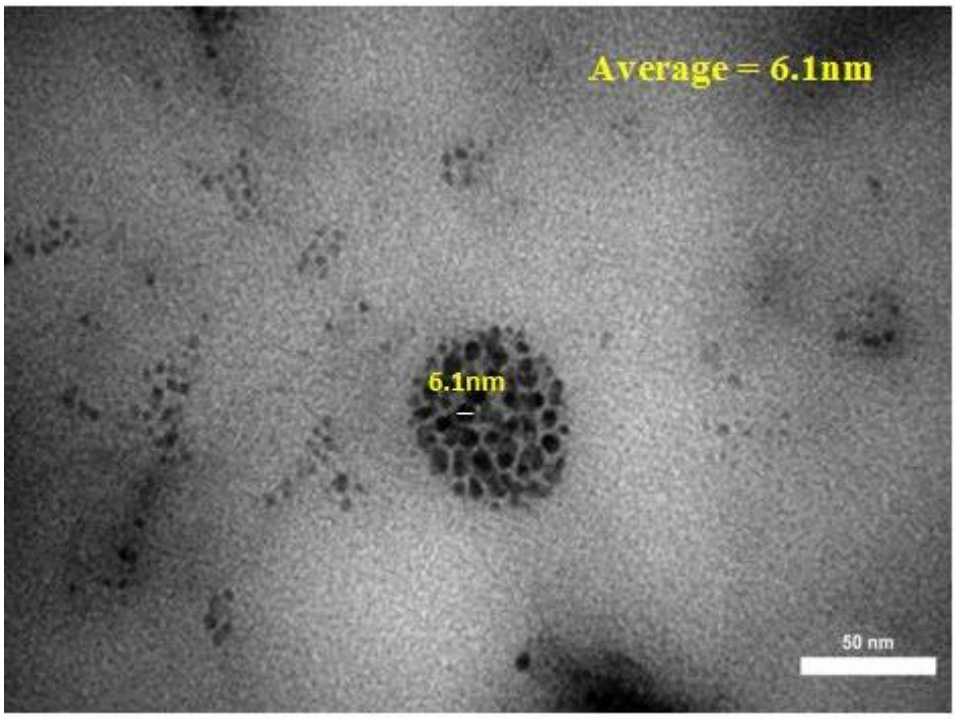

Figure (4.4):TEM Image of $P_3HT\text{-}G_{200P}/MoS_{2\ 500P}$ Colloidal Nanoparticles.

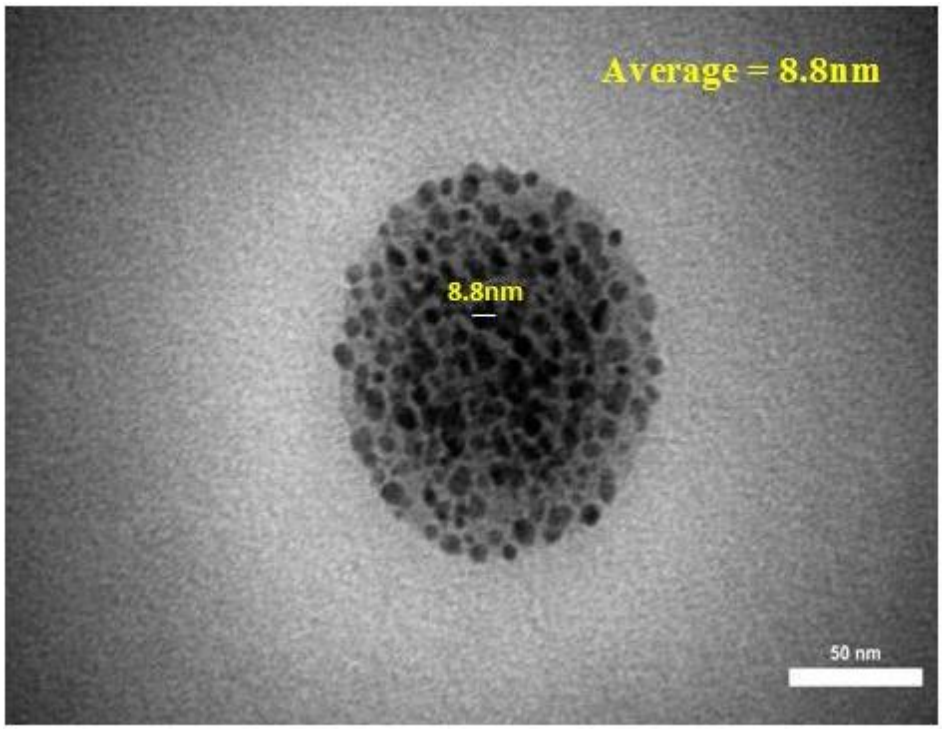

Figure (4.5):TEM Image of $P_3HT\text{-}G_{200P}/MoS_{2\ 800P}$ Colloidal Nanoparticles.

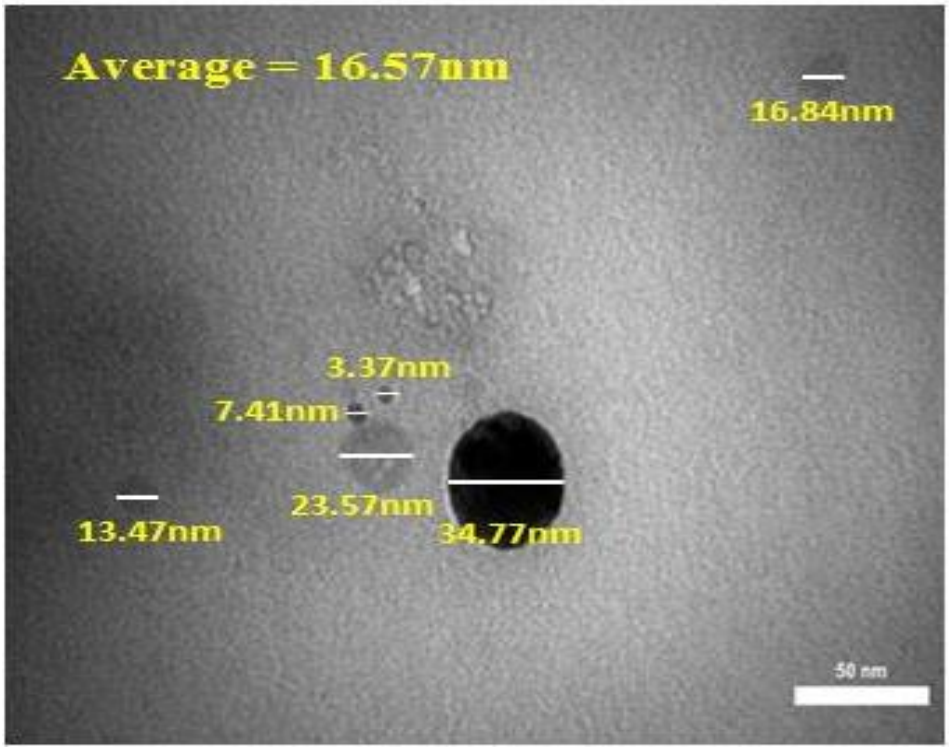

Figure (4.6):TEM Image of $P_3HT\text{-}G_{500P}$ / $MoS_{2\ 200P}$ Colloidal Nanoparticles.

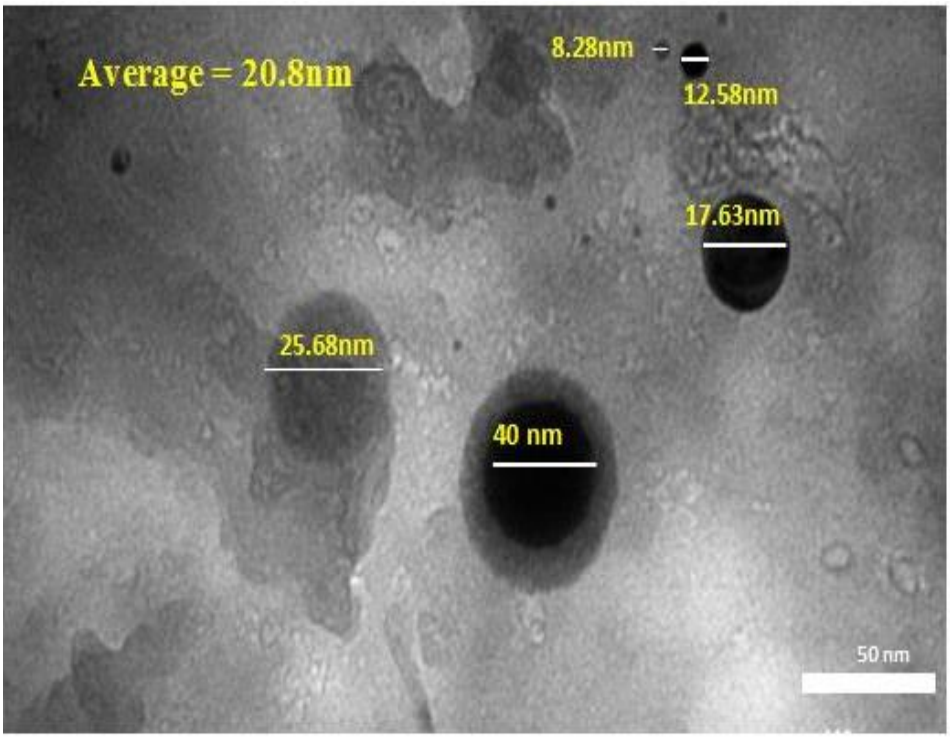

Figure (4.7): TEM Image of $P_3HT\text{-}G_{800P}$/$MoS_{2\ 200P}$ Colloidal Nanoparticles.

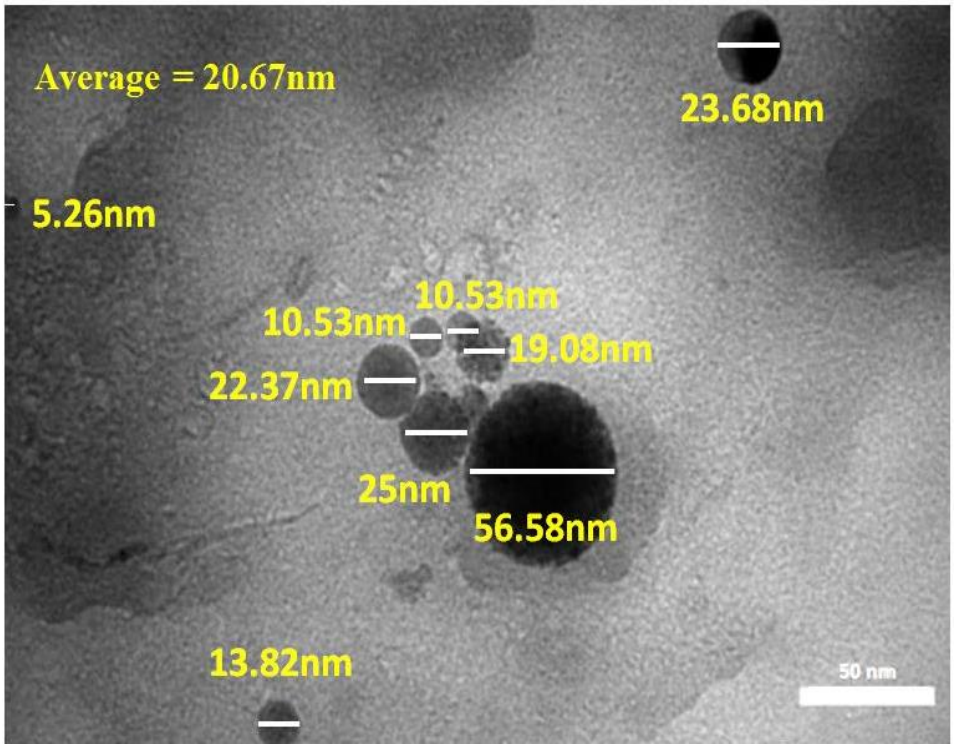

Figure (4.8): TEM Image of $P_3HT\text{-}G_{800P}$ / $MoS_{2\ 800P}$ Colloidal Nanoparticles.

4.2.4 Elemental Analysis (EDX)

The elemental composition of the P_3HT-G/MoS_2 nanocomposite was analyzed using energy-dispersive X-ray spectroscopy (EDX) for P_3HT-G/MoS_2 nanocomposite thin films at various laser pulse numbers, and the results are presented in Figures (4.9-4.14). The analysis confirms the presence of chemical elements of carbon, oxygen, sulphur, and molybdenum in the nanocomposites. It was noted that there are elements that increase and elements that decrease with the increase in the number of laser ablation pulses for the graphene and MoS_2 pellets. The EDX analysis of the P_3HT-G /MoS_2 films has been listed in Table (4.3).

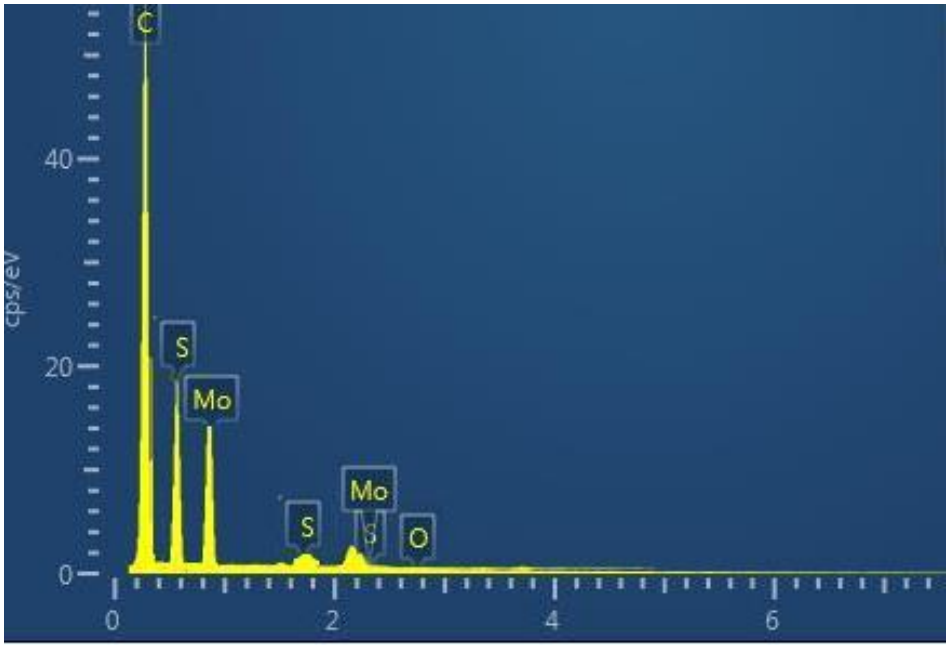

Figure (4.9): EDX Spectra for $P_3HT\text{-}G_{200P}/MoS_{2\ 200P}$ Prepared Film.

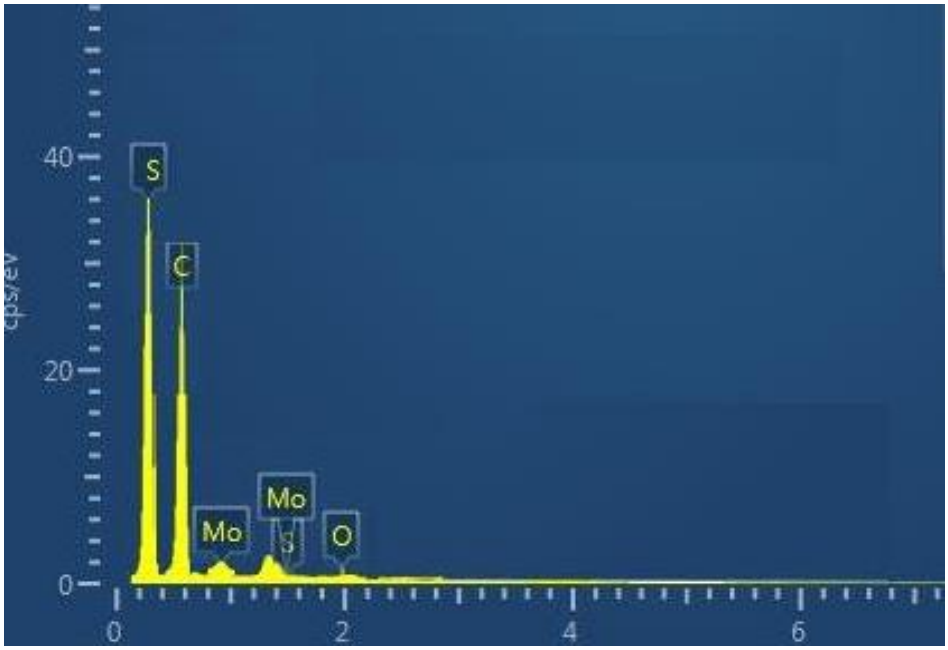

Figure (4.10): EDX Spectra for $P_3HT\text{-}G_{200P}/MoS_{2\ 500P}$ Prepared Film.

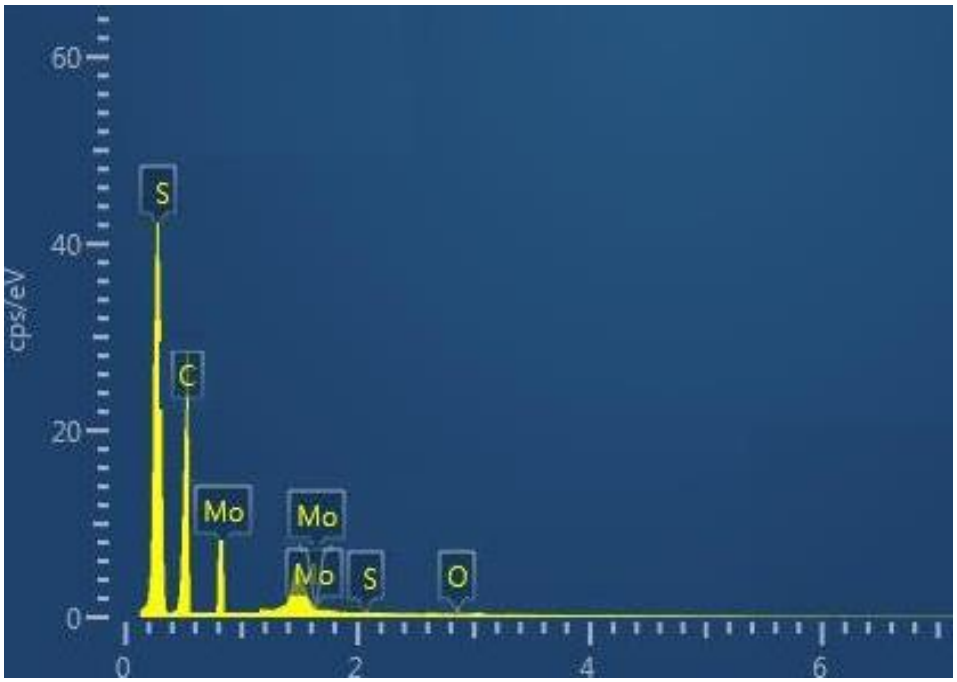

Figure (4.11): EDX Spectra for $P_3HT\text{-}G_{200P}/MoS_{2\ 800P}$ Prepared Film.

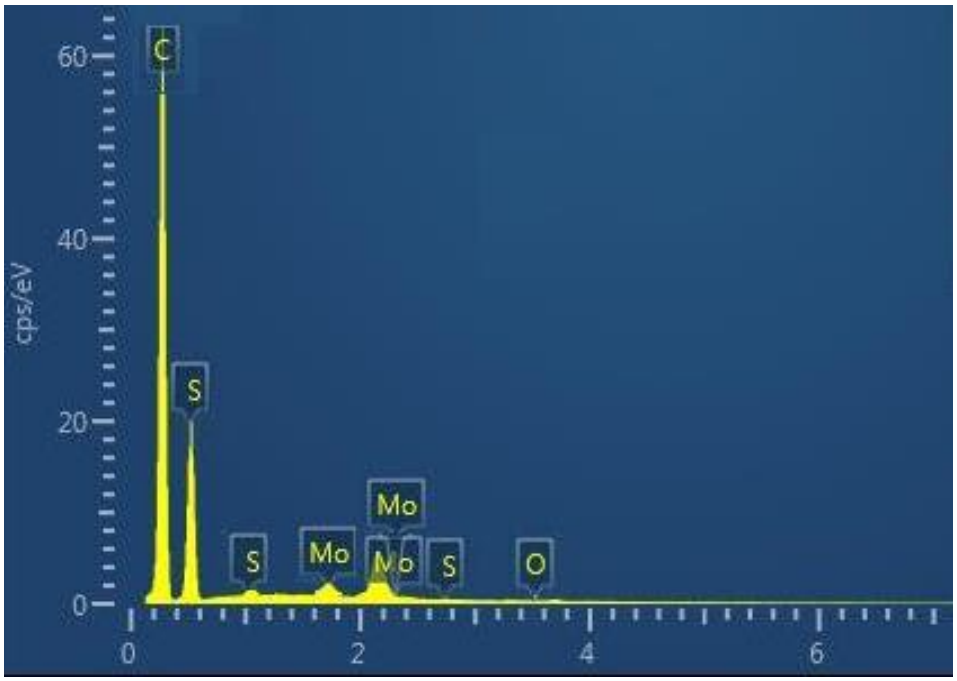

Figure (4.12): EDX Spectra for $P_3HT\text{-}G_{500P}/MoS_{2\ 200P}$ Prepared Film.

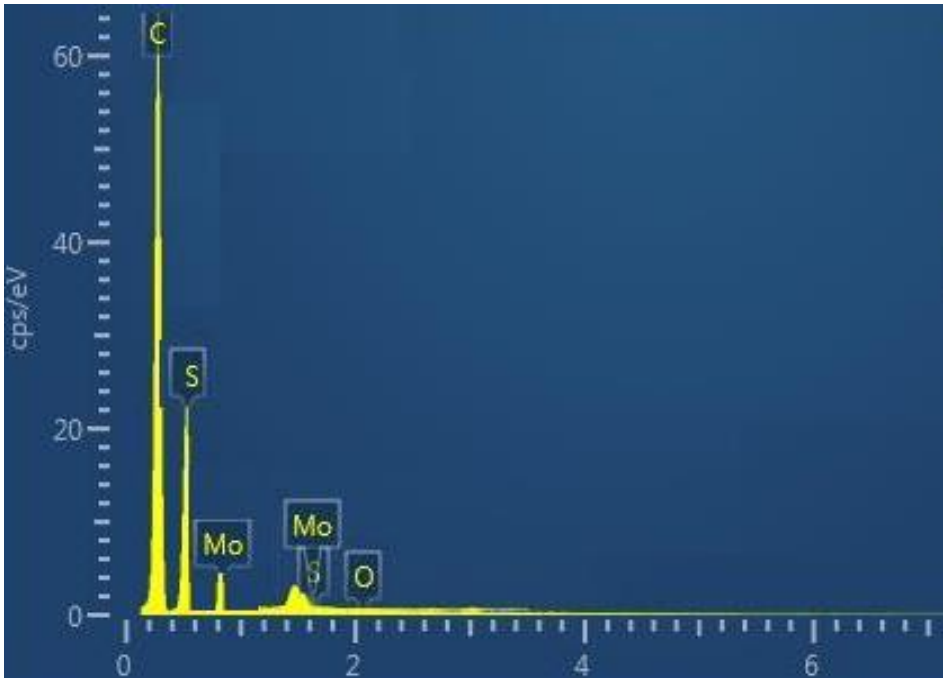

Figure (4.13): EDX Spectra for $P_3HT\text{-}G_{800P}/MoS_{2\ 200P}$ Prepared Film.

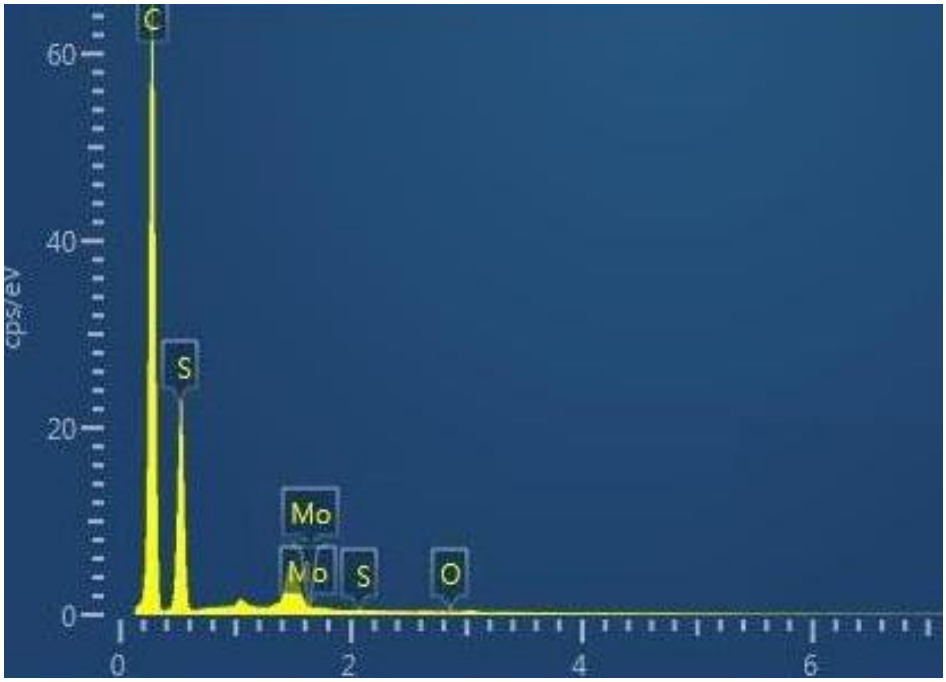

Figure (4.14): EDX Spectra for $P_3HT\text{-}G_{800P}/MoS_{2\ 800P}$ Prepared Film.

Table (4.3): The elements ratios of EDX analysis of P_3HT-G /MoS_2 films.

Samples	C	Mo	S	O	Total
$P_3HT - G_{200}$ /$MoS_{2\ 200}$	61.052	17.894	21.052	0	100
$P_3HT - G_{800}$ /$MoS_{2\ 800}$	65.829	6.532	27.135	0.502	100
$P_3HT - G_{200}$ /$MoS_{2\ 500}$	37.926	10.366	51.580	0.126	100
$P_3HT - G_{200}$ /$MoS_{2\ 800}$	31.0	24.0	45.0	0	100
$P_3HT - G_{500}$ /$MoS_{2\ 200}$	60.707	15.858	23.333	0.101	100
$P_3HT - G_{800}$ /$MoS_{2\ 200}$	64.646	10	25.252	0.101	100

4.3 Optical Properties Measurements

4.3.1 Absorbance (A) and Absorption Coefficient (α)

Figure (4.15) shows the absorption spectra for each P_3HT, G and MoS_2 in the chloroform solution, where it was observed that the absorption peak of the P_3HT polymer is in the visible region at a wavelength of (446) nm and was in agreement with the Ref. [133]. While the graphene in the ultraviolet at (271) nm is consistent with previous studies [134] and notice the absorption edge of MoS_2 at (520) nm, and also notice the weak peak at (636) nm which is identical to the Ref. [135].

The absorption spectra of all prepared samples are shown in Figure (4.16). It was observed that there was an increase and decrease in the absorption intensity with the increase in the number of laser pulses for both graphite and MoS_2 pellets, indicating an increase in the concentration of nanoparticles and also which may be attributed to the blackbody properties of graphene. The highest absorption peak is 0.92 at the wavelength 303nm for the sample $P_3HT - G_{800P}$ /$MoS_{2\ 800P}$ and the lowest peak is 0.74 at the wavelength 277nm for the sample P_3HT–

$G_{200P}/MoS_{2\ 200P}$. Additionally, a shift towards the longer wavelengths for the sample $P_3HT–\ G_{800P}/MoS_{2\ 800P}$, indicates an increase in particle size due to the quantum confinement effect, which is supported by previous research [136]. The combination of these three materials leads to the formation of a new nanocomposite with a broad absorption range extending from UV-NIR, and this will be very useful in optoelectronics. It shows very promising properties not only for future nanoscale applications but also for photonic applications such as solar cells and photodetectors.

Figure (4.17) shows the absorption coefficient as a function of the wavelength, it increases and decreases with the increase of the number of the laser pulses. This result is due to the increasing absorption for all the prepared samples which is attributed to the increasing concentration both of the GNPs and MoS_2NPs in the P_3HT solution. Table (4.4) displays the absorbance values and absorption coefficient for all the samples prepared. The absorption coefficient spectra (α) for all the prepared samples were determined using of equation (2-7). It is noteworthy that the value of the absorption coefficient (α) for all samples is more than (10^4) cm^{-1}, indicating a direct energy gap.

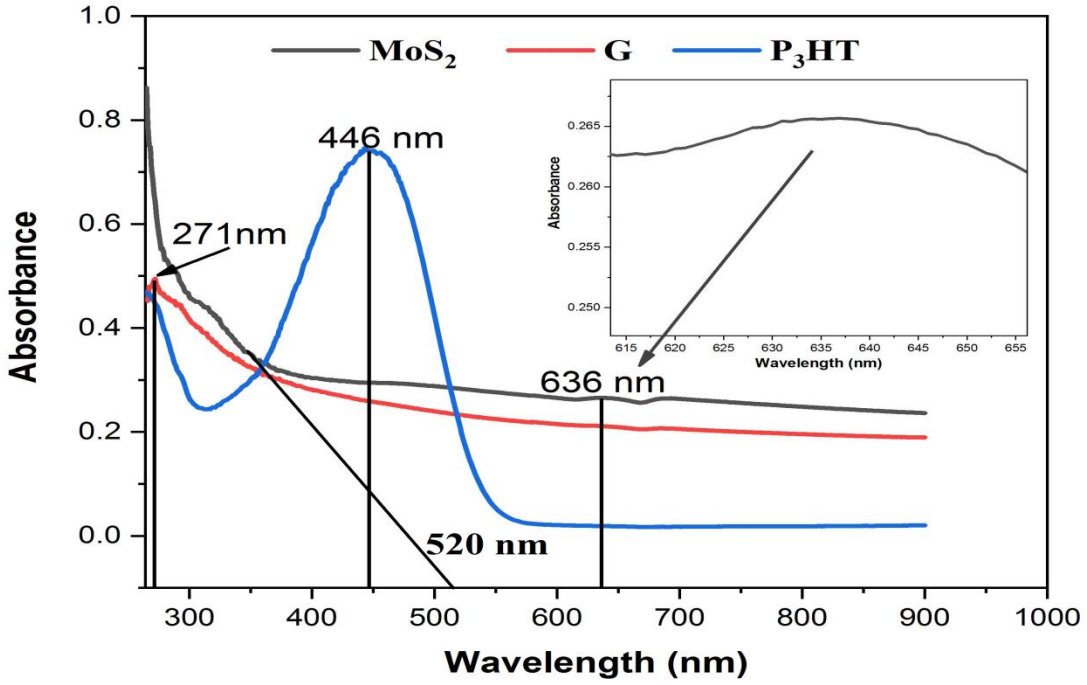

Figure (4.15): Shows the Absorbance Spectra of G, MoS_2 and P_3HT Prepared in Chloroform Solution.

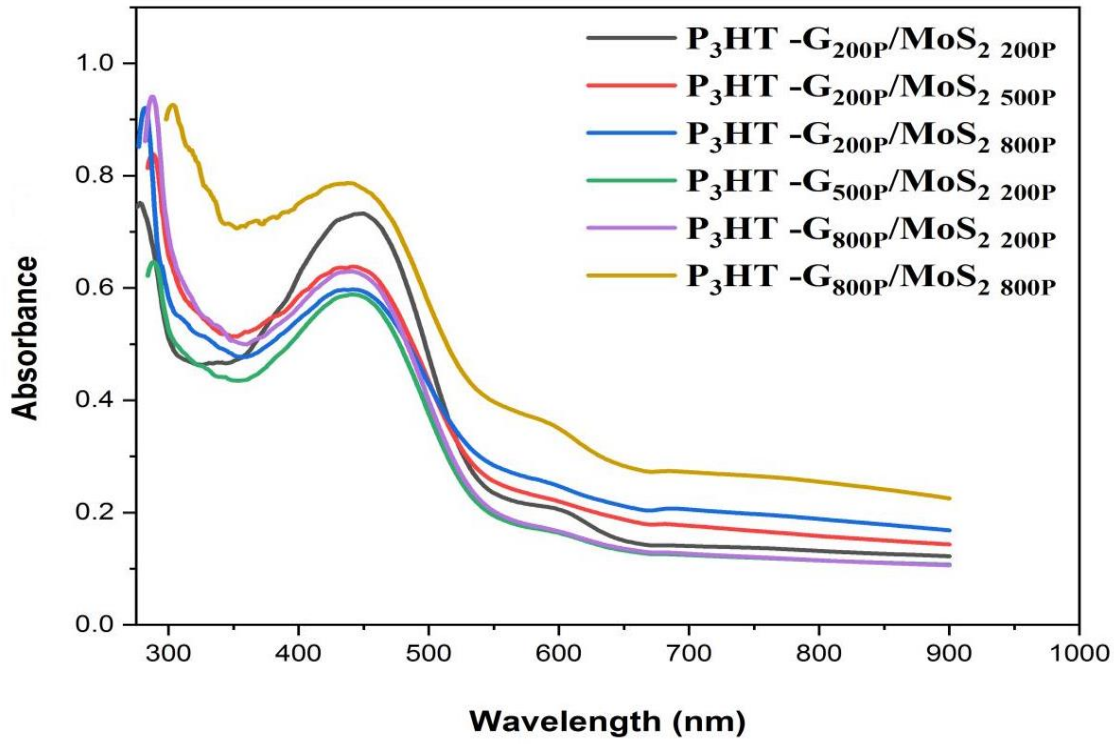

Figure (4.16): Shows the Absorbance Spectra of all the Prepared Samples.

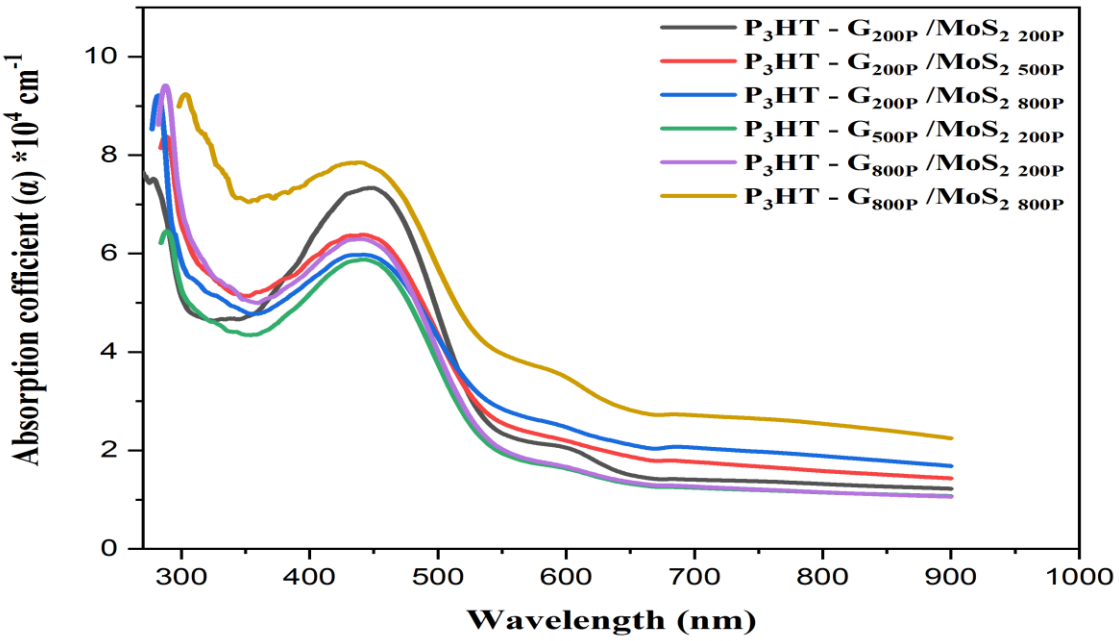

Figure (4.17): The Absorption Coefficient Spectra of for all the Prepared Samples with Different Laser Pulses Number.

Table (4.4): Shows the Absorbance Values and the Absorption Coefficient for all the Prepared Samples of (P_3HT - G/ MoS_2) Nanocomposite.

Samples	Absorbance	λ_{peak} (nm)	$\alpha \times 10^4$ (cm^{-1})
$P_3HT - G_{200P}$ /$MoS_{2\ 200P}$	0.74	277	7.4
$P_3HT - G_{800P}$ /$MoS_{2\ 800P}$	0.92	303	9.1
$P_3HT - G_{200P}$ /$MoS_{2\ 500P}$	0.83	289	8.3
$P_3HT - G_{200P}$ /$MoS_{2\ 800P}$	0.92	282	9.2
$P_3HT - G_{500P}$ /$MoS_{2\ 200P}$	0.64	290	6.3
$P_3HT - G_{800P}$ /$MoS_{2\ 200P}$	0.94	293	9.4

4.3.2 Optical Energy Gap(E_g)

The energy band gap of the $P_3HT–G/MoS_2$ nanocomposite has drawn between $(\alpha h\upsilon)^2$ and photon energy ($h\upsilon$), as shown in Figure (4.18). The energy gap values of the P_3HT-G/MoS_2 nanocomposite decreased from (2.28) eV for the sample $P_3HT–G_{200P}/MoS_{2\ 200P}$ to (2.1) eV for the sample $P_3HT–G_{800P}/MoS_{2\ 800P}$, with increasing number of laser ablation pulses for both the graphene and MoS_2 target. This decrease in the energy gap is attributed to the increase in graphene and its combination with MoS_2 leads to a decrease in the band gap because of the improved electrical conductivity of Hybrid material [137], or due to the creation of defects in the material by breaking the Mo-S bonds and creating sulfur vacancies. These defects act as trap states for electrons and holes, reducing the bandgap of the material. This effect has been observed in several studies, including a study by Wang et al.[138] and another by Huang et al.[139]. The direct energy gap values for all prepared samples obtained are shown in Table (4.5).

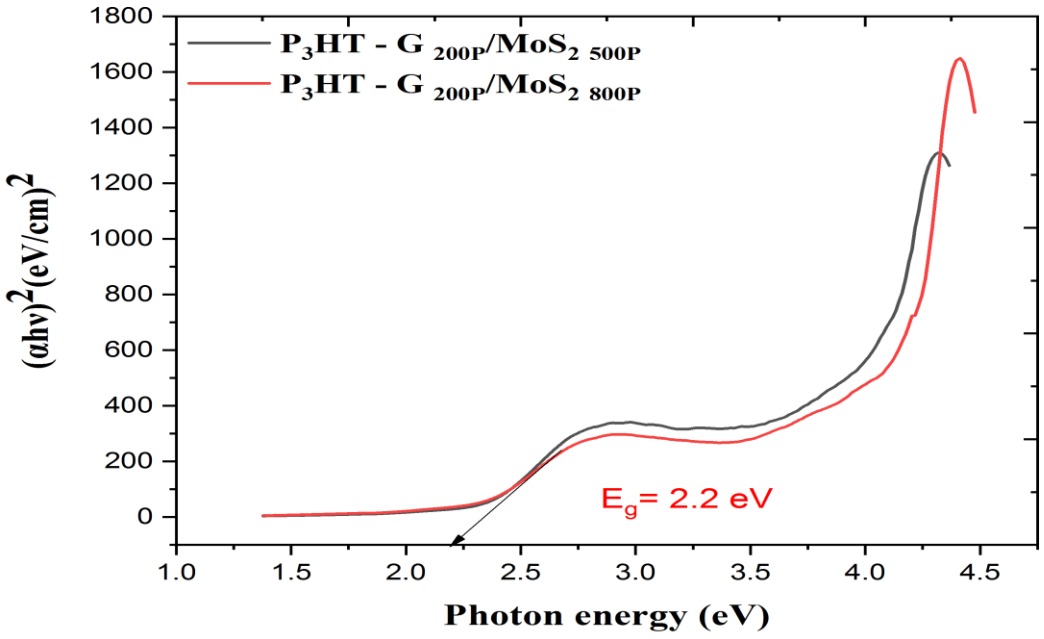

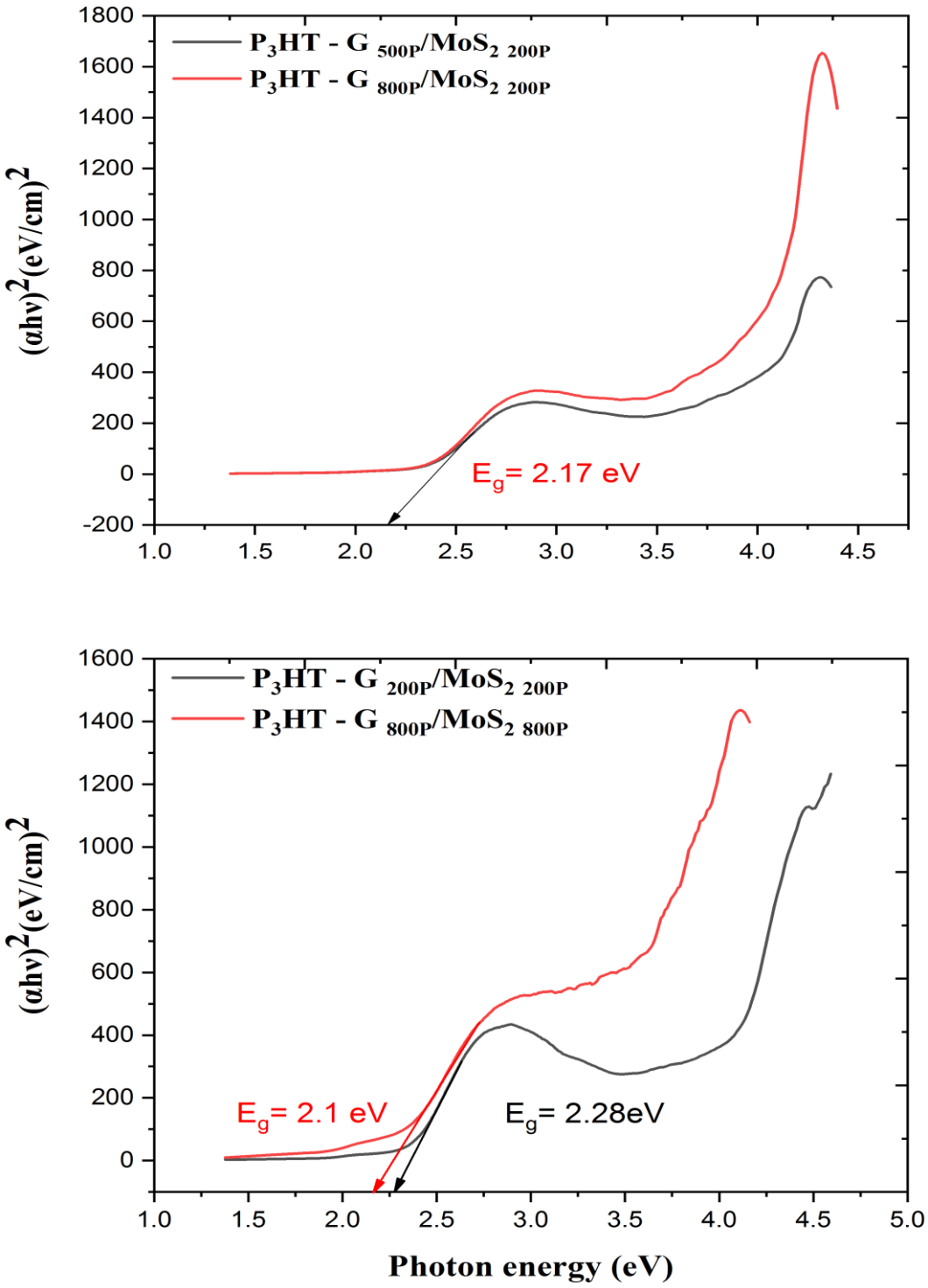

Figure (4.18): $(\alpha h\upsilon)^2$ versus Photon Energy Gap of $P_3HT - G / MoS_2$ Nanocomposite with Different Numbers of Laser Pulses.

Table (4.5): Allowed direct Energy Gap values for all Prepared Samples.

Samples	Allowed direct E_g (eV)
$P_3HT - G_{200P}$ /$MoS_{2\ 200P}$	2.28
$P_3HT - G_{800P}$ /$MoS_{2\ 800P}$	2.1
$P_3HT - G_{200P}$ /$MoS_{2\ 500P}$	2.2
$P_3HT - G_{200P}$ /$MoS_{2\ 800P}$	2.2
$P_3HT - G_{500P}$ /$MoS_{2\ 200P}$	2.17
$P_3HT - G_{800P}$ /$MoS_{2\ 200P}$	2.17

4.3.3 Fourier Transform Infrared (FTIR)

FTIR spectra of synthesized P_3HT-G/MoS_2 NP_S at different laser pulses are illustrated in Figure (4.19). The ablation of both the graphite target and MoS_2 was performed in chloroform solution at room temperature using an energy of (200) mJ and a wavelength of (1064) nm with several pulses of (800) pulse. In the P_3HT spectrum, the C-H stretching is represented by peaks at 714 and 1807 cm^{-1}[133], and observed O–H stretching vibration at peak 3482.23 cm^{-1}[140]. The MoS_2 spectrum shows bands at 667.90 and 772.29 cm^{-1} attributed to Mo–S stretching and S stretching, respectively [56]. The spectrum of G peaks at 1649.34 and 1695.42 cm^{-1}, correspond to C=C stretching [141]. In addition, the peaks at 2342.97, 2852.44 and 2919.14 cm^{-1} in the MoS_2 and G spectra represent C-H stretching [142], as shown in Figure (4.19a).

Furthermore, Figure (4.19C) shows a clear peak for the (C=C) bond, indicating increased graphene concentration in the composite material, specifically in $P_3HT\text{-}G_{200P}/MoS_{2\ 500P}$. In Figure (4.19D), we observe characteristic peaks of all the bonds in $P_3HT\text{-}G_{800P}/MoS_{2\ 800P}$ nanocomposite, indicating strong bonding and an increase in nanoparticle concentration for both MoS_2 and G. Overall, all the prepared nanocomposite exhibit characteristic peaks of P_3HT, MoS_2, and G in their spectra. Table (4.6) shows chemical bonds and their IR resonance positions of G NP_S and MoS_2 NP_S.

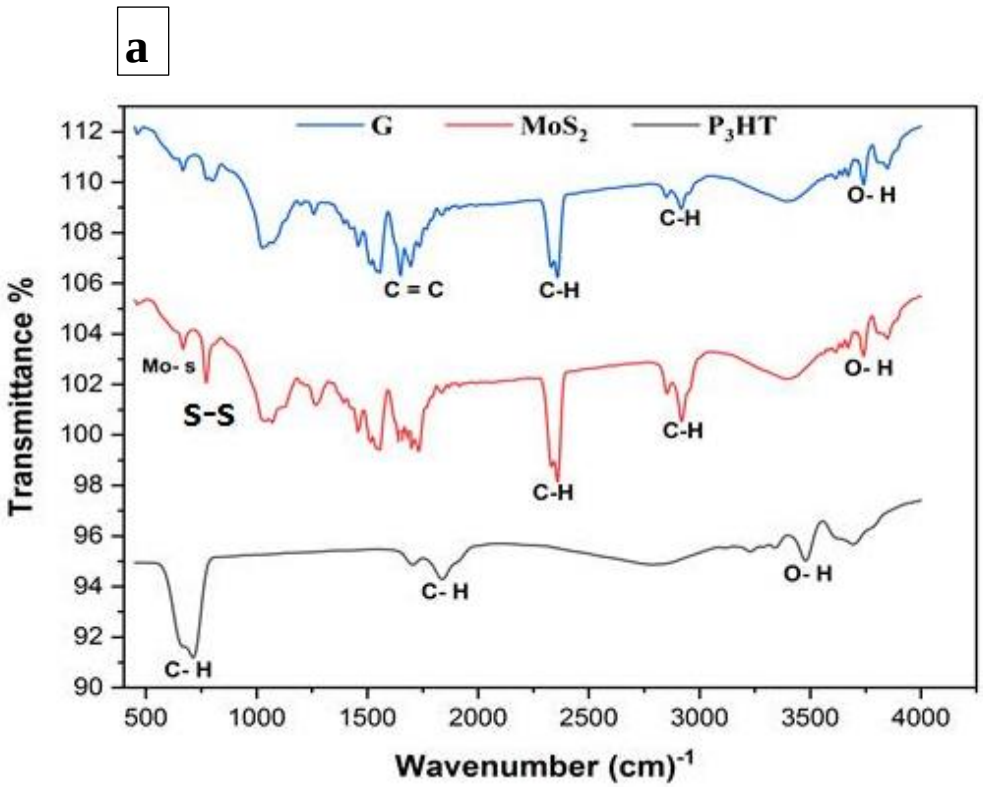

b

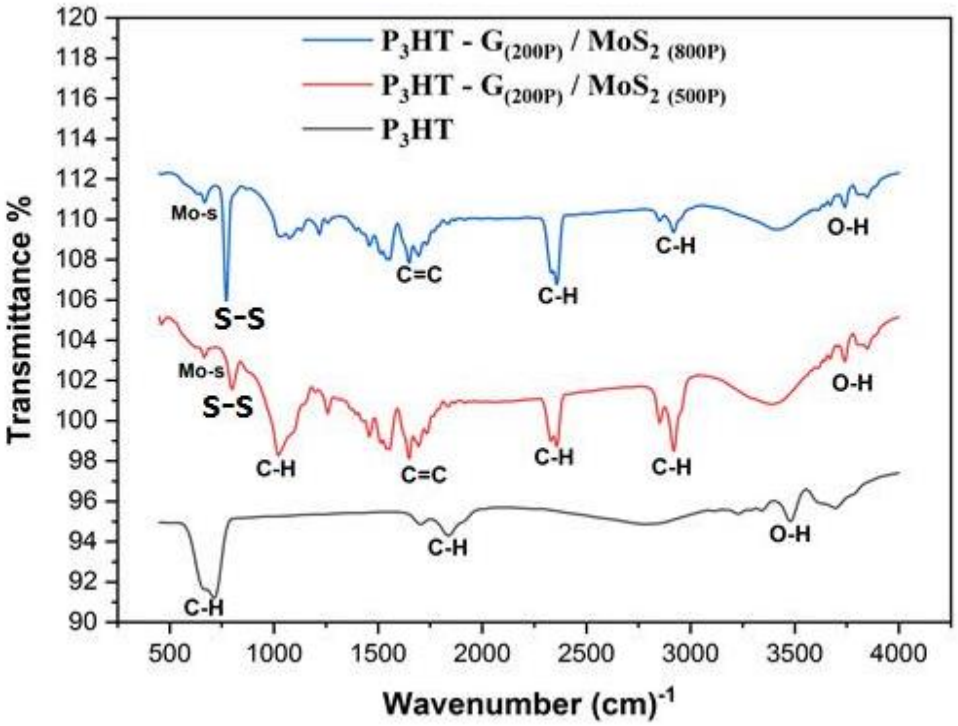
P3HT - G(200P) / MoS2 (800P)
P3HT - G(200P) / MoS2 (500P)
P3HT
Transmittance %
Wavenumber (cm)-1
Mo-s
S-S
C=C
C-H
O-H

c

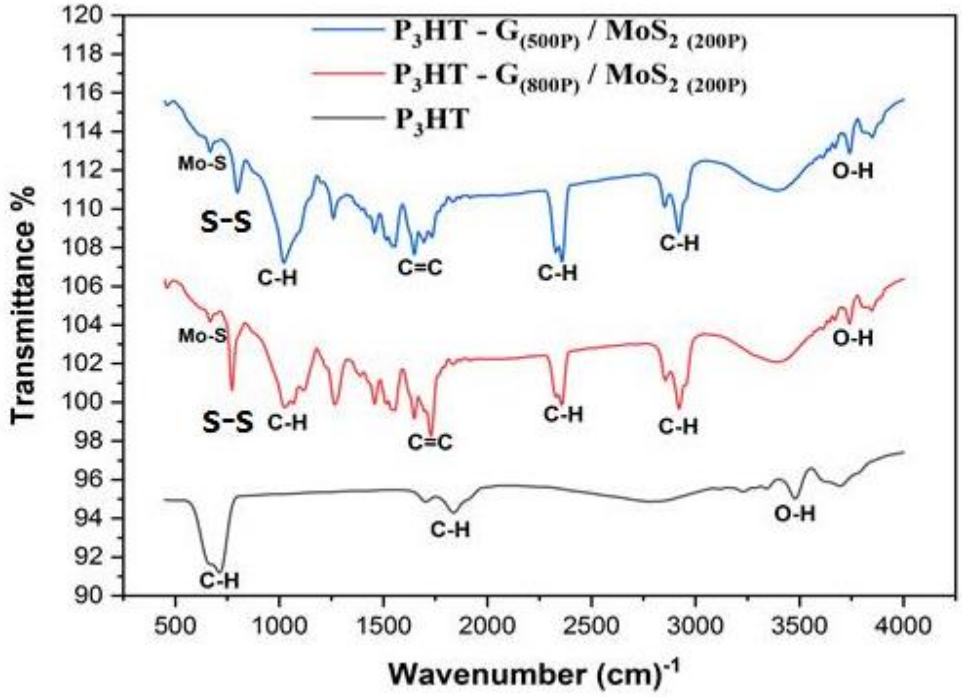
P3HT - G(500P) / MoS2 (200P)
P3HT - G(800P) / MoS2 (200P)
P3HT
Transmittance %
Wavenumber (cm)-1
Mo-S
S-S
C=C
C-H
O-H

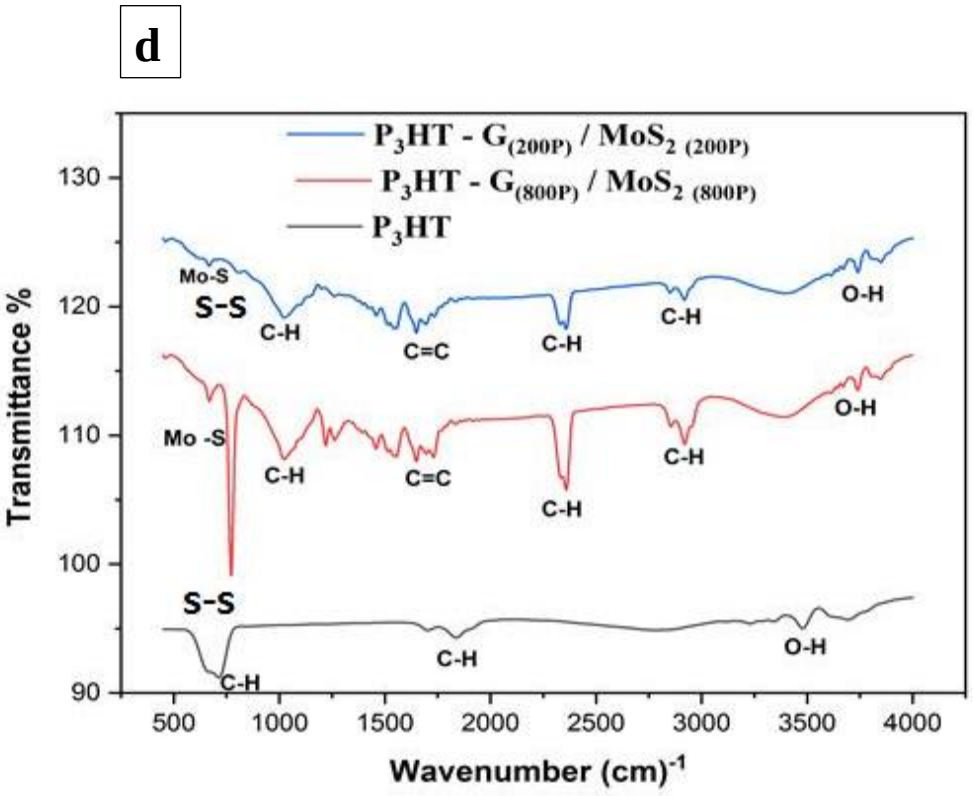

Figure (4.19): FTIR Spectra of P_3HT-G/MoS_2 NP_S Samples With Different Laser Pulse.

Table (4.6): Chemical Bonds and Their IR Resonance Positions of G NP_S and MoS_2 NP_S.

Bonds	Wavenumber (cm^{-1})	vibration Region	Ref. For comparative
C-H	714	NIR -IR	[133]
	1807	NIR -IR	[133]
	2342.97	Mid -IR	[142]
	2852.44	Mid -IR	[142]
	2919.14	Mid -IR	[142]
	3394.80	Mid -IR	[133]
Mo -S	667.90	Visible	[56]
S-S	772.29	NIR -IR	[56]
C=C	1649.34	NIR -IR	[141]
	1695.42	NIR -IR	[141]

4.4 Electrical Properties

4.4.1 Hall Effect

The Hall effect measurements, including Hall coefficient (R_H), carrier concentrations (n_e), electrical conductivity (σ), and Hall mobility (μ_H) were performed for all P_3HT-G/MoS_2 films deposited on a glass substrate, and the results are presented in Table (4.7). The Hall Effect measurements indicated that all of the P_3HT-G/MoS_2 nanocomposite films were n-type. It was observed that the Hall coefficient decreased while the carrier concentration increased for some films with an increase in the number of laser pulses for both GNP_s and MoS_2NP_s. This was attributed to the increasing concentration due to confinement by dynamic light scattering [143]. On the other hand, it was observed that resistivity decreased while electrical conductivity increased for some prepared films with an increase in the number of laser pulses for both GNPs and MoS_2NPs . This behaviour was also attributed to the increase of carrier concentration resulting from confinement by dynamic light scattering. This is because the confinement restricts the motion of the carriers, which can lead to them being trapped in a smaller volume. This can increase the carrier concentration in the confined region, increase conductivity, improve optical properties and enhance photoluminescence, which is consistent with previous studies [144]. Additionally, the Hall mobility was found to be decreased with an increase in the number of laser pulses for both GNPs and MoS_2NPs for some prepared films of the nanocomposite. This decrease in the mobility of carriers may have been caused by ionized impurity scattering and a decrease in carrier mobility due to high carrier concentration, which is consistent with previous studies [145].

Table (4.7) :The result of Hall Measurement for all the Prepared Films of the Nanocomposite.

samples	$n_e \times 10^{18}$ $(cm)^{-3}$	R_H $(cm^{-3}C^{-1})$	σ $(\Omega.cm)^{-1}$	μ_H $(cm^2V^{-1}s^{-1})$	Carrier type
$P_3HT - G_{200P}$ /$MoS_{2\ 200P}$	1.67	-3.75	17.7	66.2	n
$P_3HT - G_{800P}$ /$MoS_{2\ 800P}$	6.39	-9.78	25.4	24.8	n
$P_3HT - G_{200P}$ /$MoS_{2\ 500P}$	1.63	-3.84	10.5	40.3	n
$P_3HT - G_{200P}$ /$MoS_{2\ 800P}$	3.23	-1.93	19.3	37.4	n
$P_3HT - G_{500P}$ /$MoS_{2\ 200P}$	1.51	-4.13	13	53.9	n
$P_3HT - G_{800P}$ /$MoS_{2\ 200P}$	2.18	-2.87	17.9	51.4	n

4.5 Electrical and Optoelectronic Properties of Heterojunction

4.5.1 Dark Current-Voltage Measurements

The electrical behaviour of Ag/PSi/P_3HT–G/MoS_2/Ag such as Schottky or heterojunction is determined generally by depending on the characteristics of current-voltage characteristics.

From Figures 4.20(a-f), it can be noted that the forward current is very small at a voltage less than (2V). This current known as recombination current, is due to the presence of recombination centers, which occurs at low voltages only. Increasing the value of the bias

voltage on both sides of the heterojunction leads to the decrease of the built-in potential, as well as the width of the depletion layer, At high voltage an exponential current arises increasing with the increase of the bias voltage called diffusion current. In this region; the bias, voltage can deliver, electrons with enough energy to penetrate, the barrier between the two sides of the junction. In the case of reverse bias, contains two regions, The first region, the current slightly observed at the low values of the reverse voltage this is due to an increase in the width of the depletion region and a decrease in the concentration of carriers. In the second region at high voltage, the diffusion current dominates until it gets saturation. It was noticed in the case of as prepared that the behavior of the current as a function of voltage will behave like Schottky meaning that the current in the forward direction is similar to the current in the reverse direction, and it may be attributed to several reasons, including the high resistance of the material, the short lifetime, or the lattice mismatch.

As for Figure 4.20(f), it can be noticed the electrical behavior of Ag/PSi/P_3HT–G/MoS_2/Ag is the behavior of a diode with a forward bias and the value of the forward current is very small when the bias voltage is less than 4 Volts.

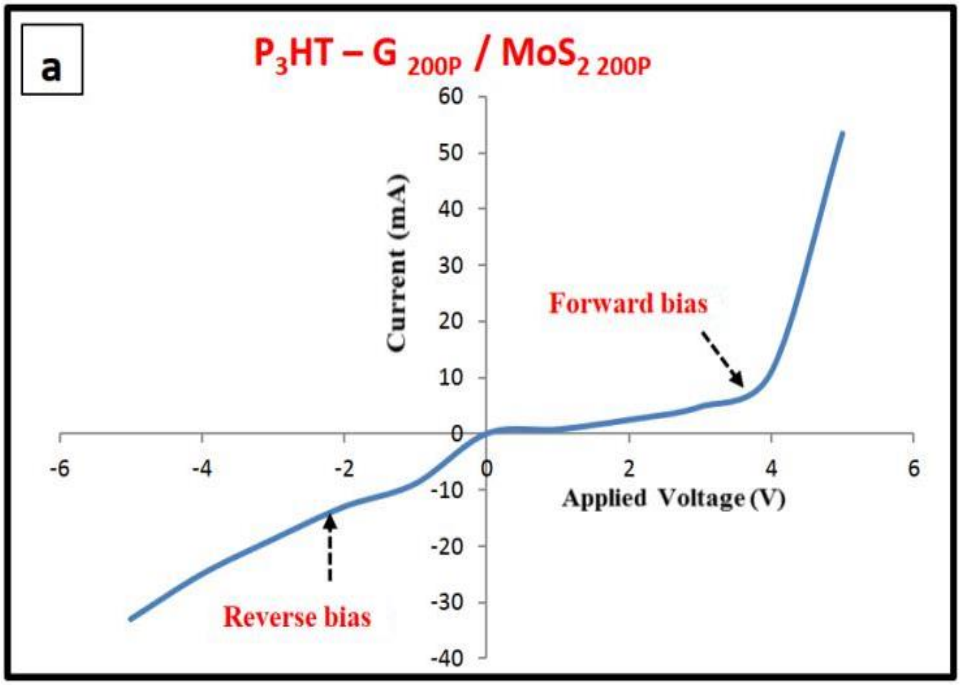
a
P3HT – G 200P / MoS2 200P
Current (mA)
Applied Voltage (V)
Forward bias
Reverse bias
60
50
40
30
20
10
0
-10
-20
-30
-40
-6
-4
-2
0
2
4
6

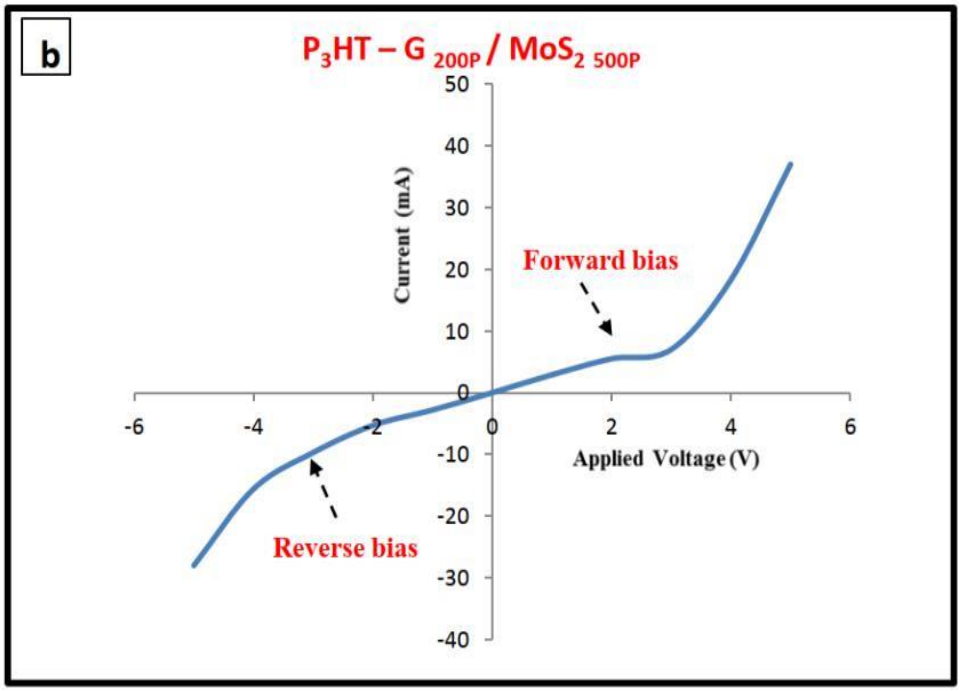
b
P3HT – G 200P / MoS2 500P
Current (mA)
Applied Voltage (V)
Forward bias
Reverse bias
50
40
30
20
10
0
-10
-20
-30
-40
-6
-4
-2
0
2
4
6

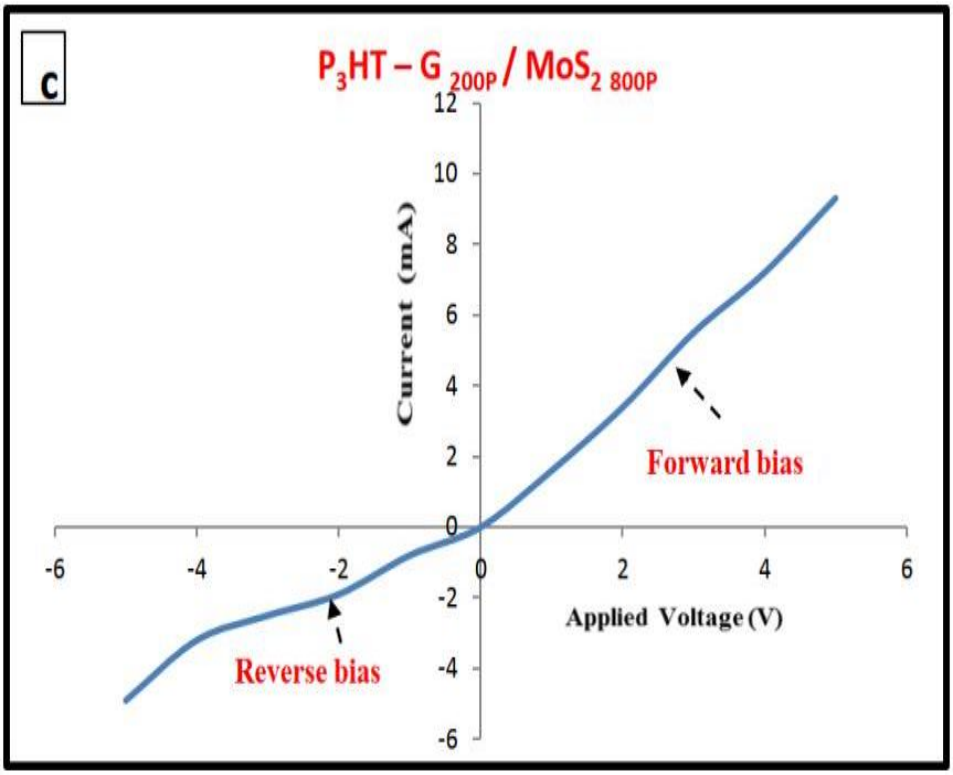
c
P3HT – G 200P / MoS2 800P
Current (mA)
Applied Voltage (V)
Forward bias
Reverse bias
12
10
8
6
4
2
0
-2
-4
-6
-6
-4
-2
0
2
4
6

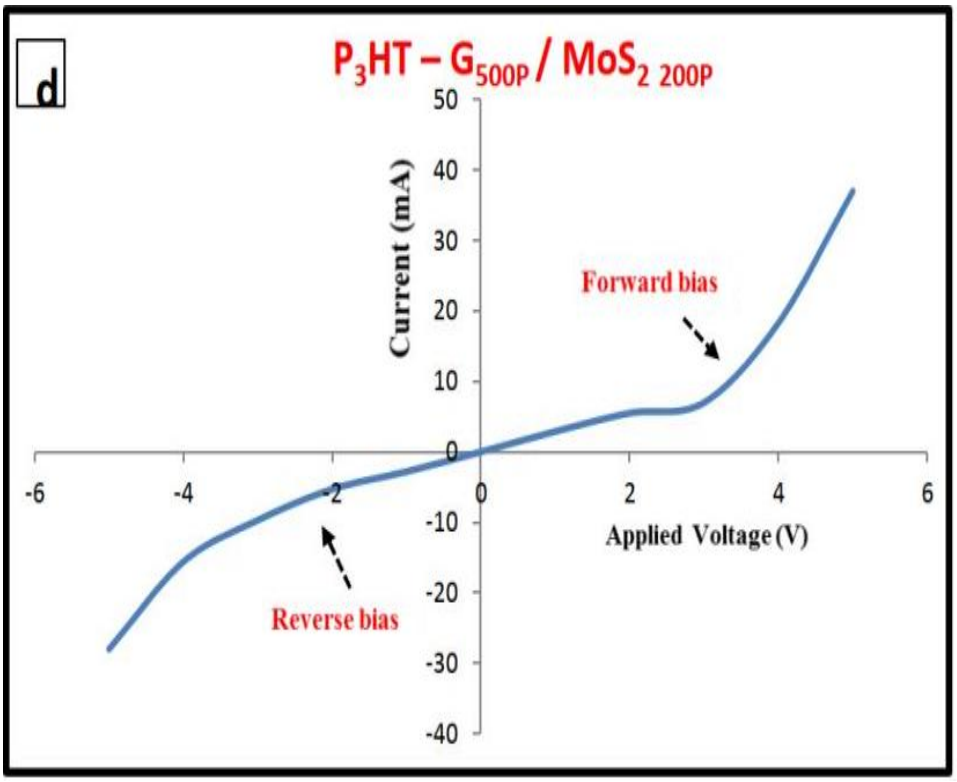
d
P3HT – G500P / MoS2 200P
Current (mA)
Applied Voltage (V)
Forward bias
Reverse bias
50
40
30
20
10
0
-10
-20
-30
-40
-6
-4
-2
0
2
4
6

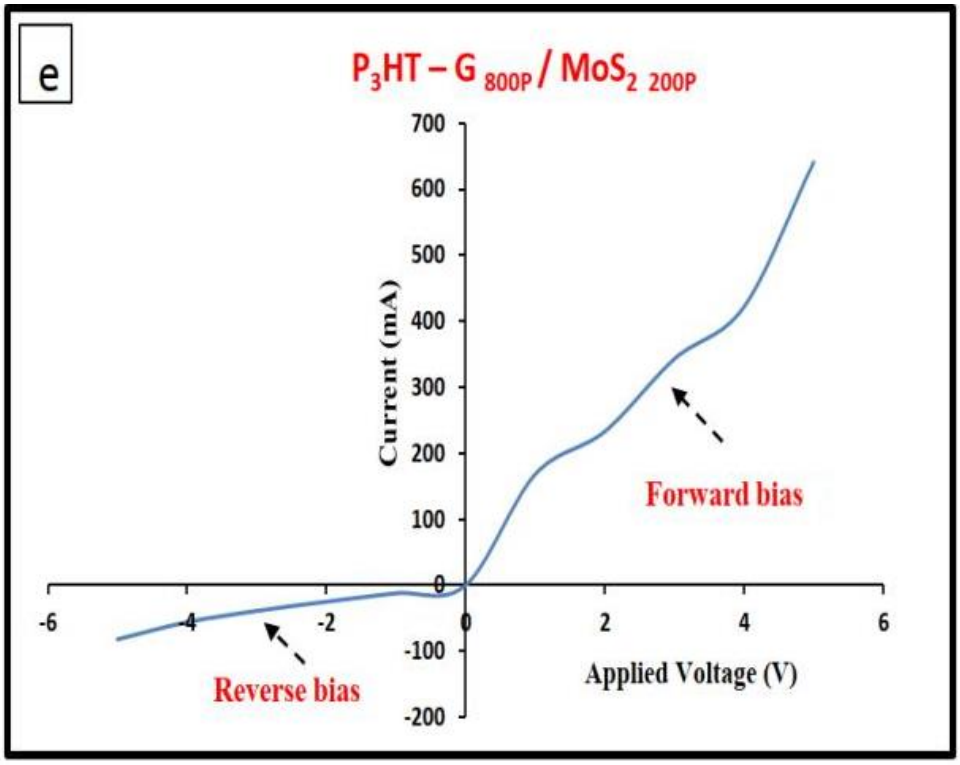

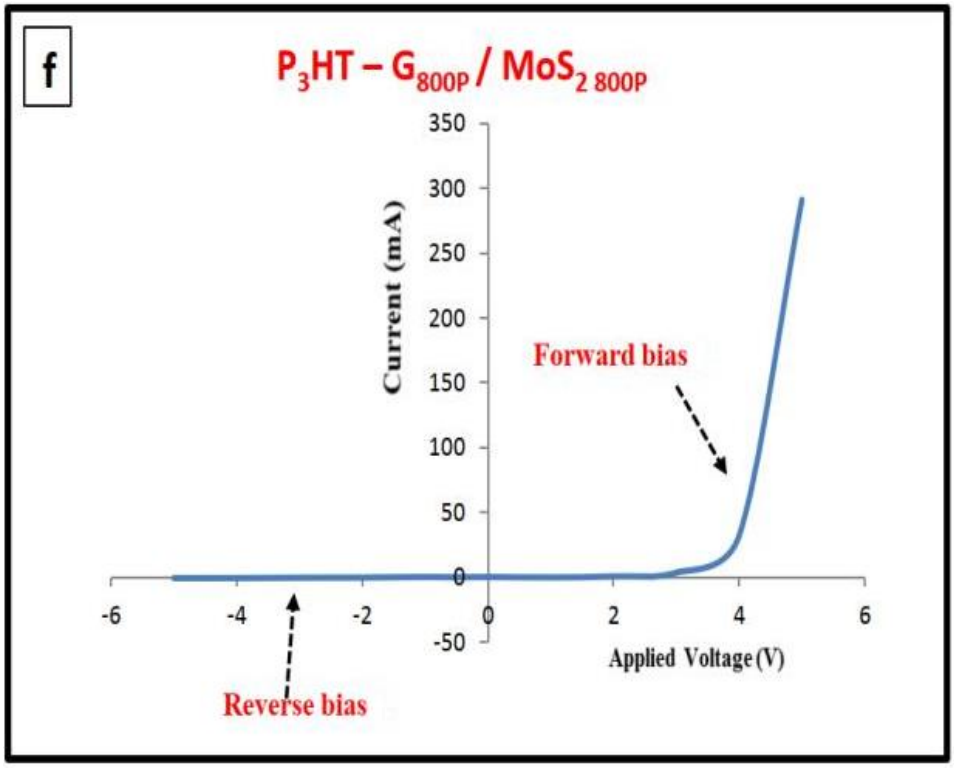

Figure (4.20): Dark (I-V) Characteristic of Ag/PSi/P_3HT–G/MoS_2/Ag Heterojunction at Different Laser Pulses.

4.5.2 I-V Characteristics under Illumination

Figures 4.21(a-f) show the device's reversed current-voltage characteristics measured in dark and under illumination conditions, the photocurrent under the illumination of a (100 mW/cm^2 tungsten lamp). The measured reverse current value under illumination for Ag/PSi/P_3HT–G/MoS_2/Ag was found to be higher than that in the dark at a given voltage.

The current starting at a low voltage is known as the thermionic emission current. The thermionic emission current and carrier velocity increase in the linear region when the sample is illuminated, this means that the light-induced carrier will contribute photocurrent as a result of the incident light absorption, thus the production of (electron–hole) pairs.

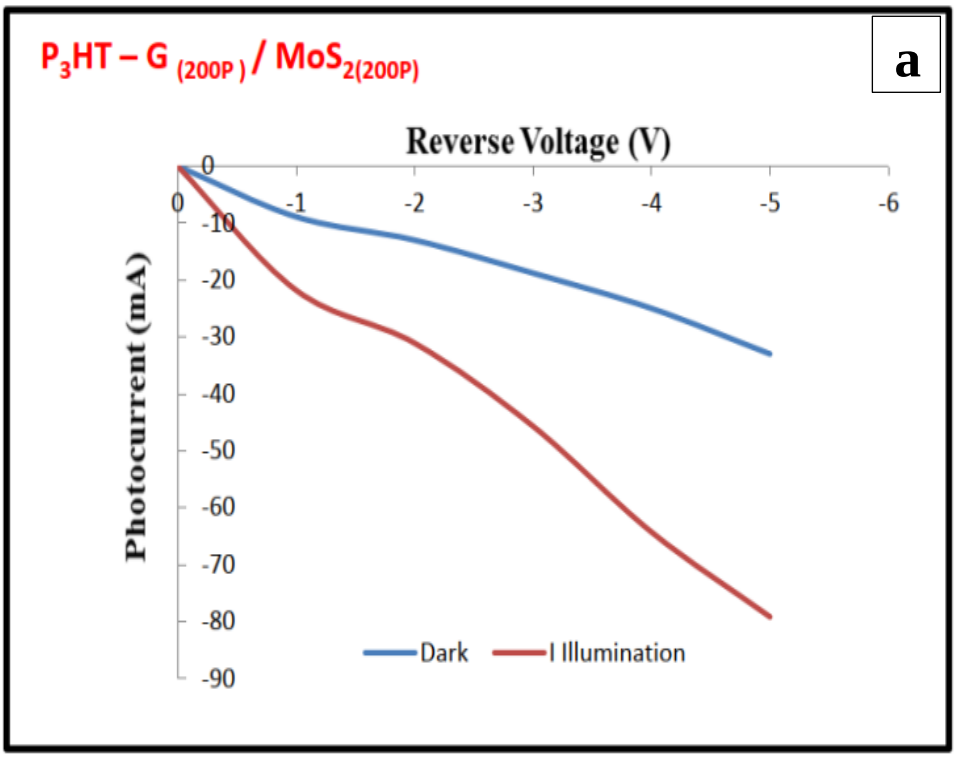

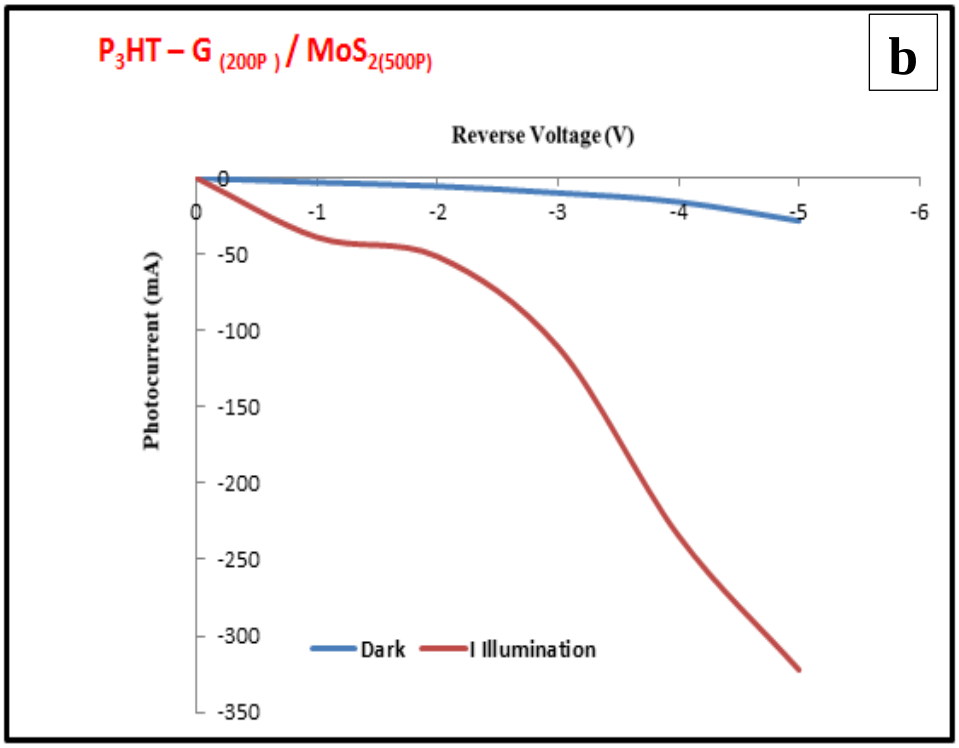
P3HT – G (200P) / MoS2(500P)
b
Reverse Voltage (V)
Photocurrent (mA)
0
-1
-2
-3
-4
-5
-6
-50
-100
-150
-200
-250
-300
-350
Dark
I Illumination

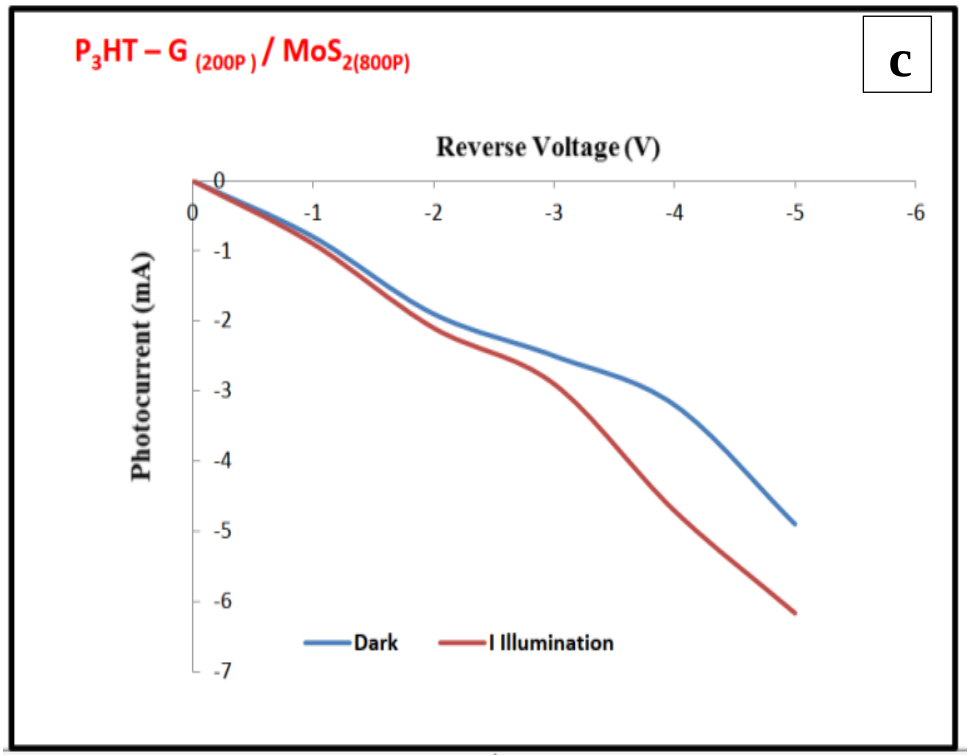
P3HT – G (200P) / MoS2(800P)
c
Reverse Voltage (V)
Photocurrent (mA)
0
-1
-2
-3
-4
-5
-6
-7
Dark
I Illumination

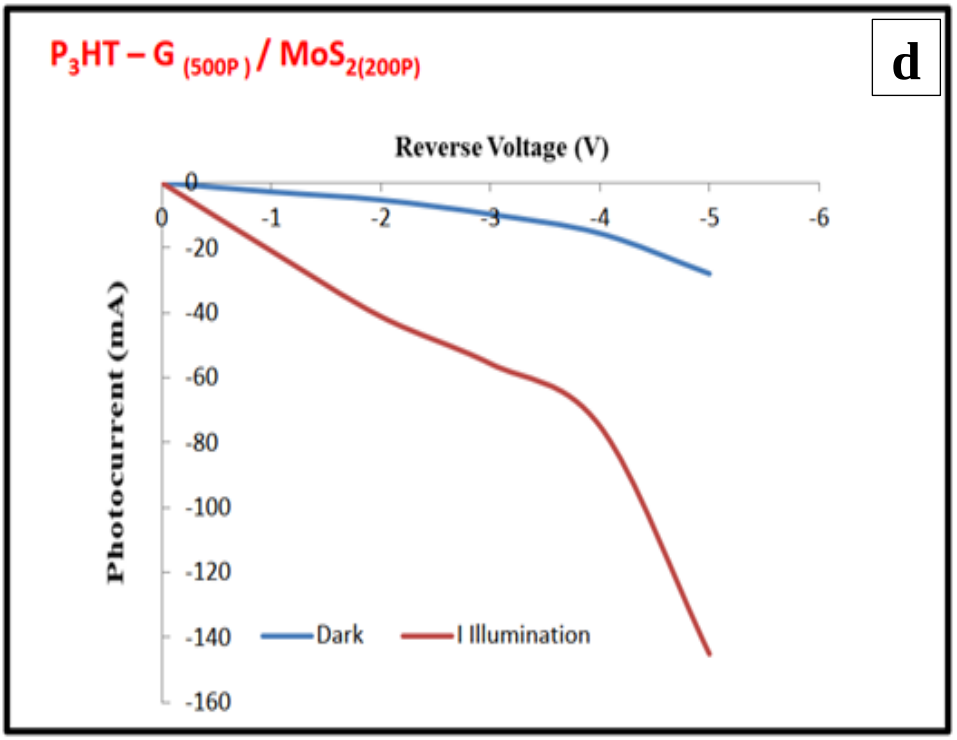
P3HT – G (500P) / MoS2(200P)
d
Reverse Voltage (V)
Photocurrent (mA)
0
-1
-2
-3
-4
-5
-6
-20
-40
-60
-80
-100
-120
-140
-160
Dark
I Illumination

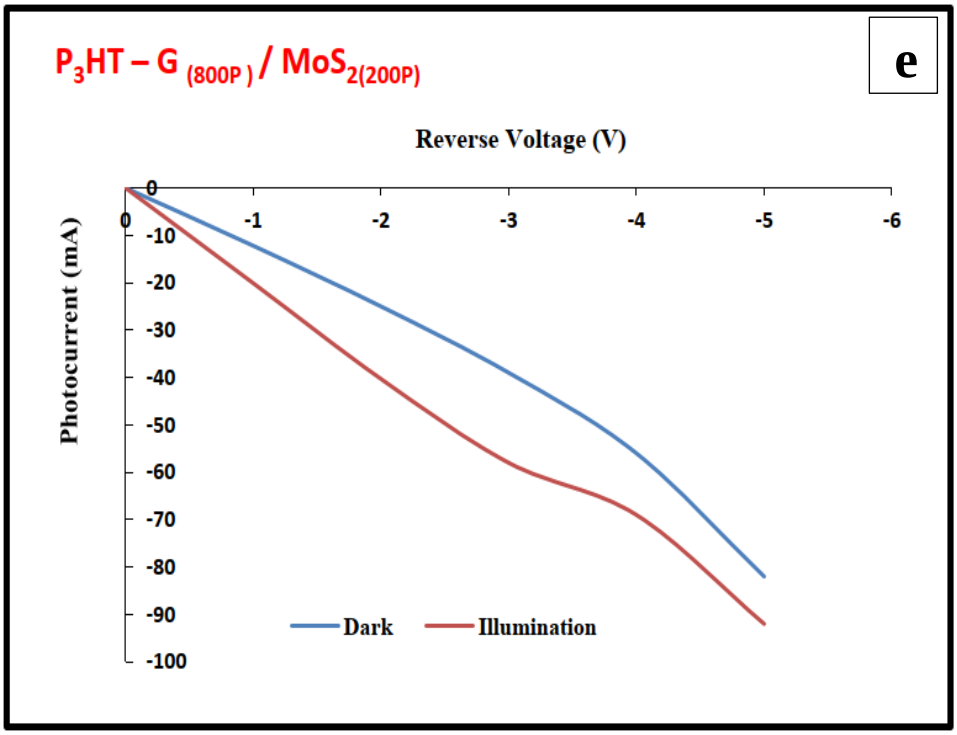
P3HT – G (800P) / MoS2(200P)
e
Reverse Voltage (V)
Photocurrent (mA)
0
-1
-2
-3
-4
-5
-6
-10
-20
-30
-40
-50
-60
-70
-80
-90
-100
Dark
Illumination

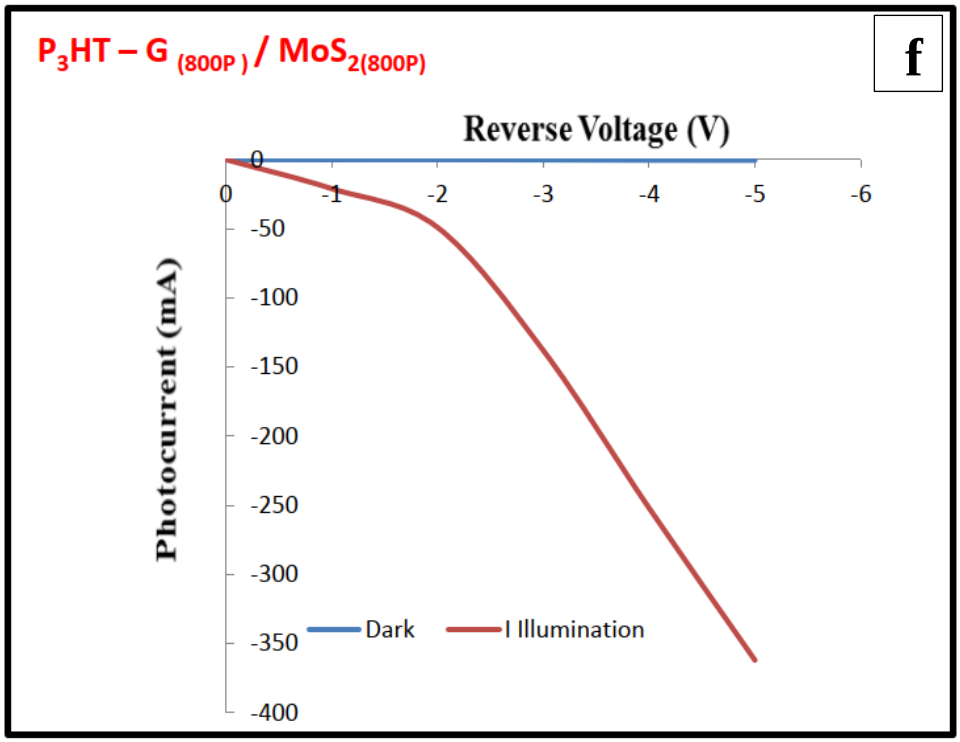

Figure (4.21): Dark and Illuminated (I-V) Characteristic of Ag/PSi/P_3HT–G/MoS_2/Ag Heterojunctionat Different Laser Pulses.

4.6 Solar Cell Parameters Measurement

Figures 4.22(a-f) present the I-V characteristics of Ag/PSi/P_3HT-G/MoS_2/Ag heterojunctions fabricated at different laser pulse numbers, with an intensity of 100 mW/cm^2. The open-circuit voltage (V_{OC}) and short-circuit current (I_{SC}) were determined at I=0 and V=0, respectively. The maximum current value (I_m) and the maximum value of the voltage (V_m) have been determined, thus extracting the maximum power from the product of (I_m.V_m), and from the previous values the filling factor (F.F) calculated according to the relationship (2-29), and from the previous values the cell efficiency (η) calculated according to the relationship (2-31) for all solar cells.

Table (4.8) summarizes the values of V_{OC}, I_{SC} maximum power voltage (V_m), maximum power current (I_m), fill factor, and conversion efficiency (η) for the fabricated solar cells. It is noteworthy that the efficiency of the solar cells increased with the increase in the number of laser pulses, which may be attributed to the increased carrier collection efficiency or the increasing depletion width and diffusion length. However, the relationship between laser pulses and efficacy is not linear. After a certain point, increasing the number of laser pulses does not significantly increase the efficiency of the solar cell. This is because the nanocomposite can only absorb so much light, and increasing the number of laser pulses beyond a certain point does not significantly increase the amount of light that is absorbed.

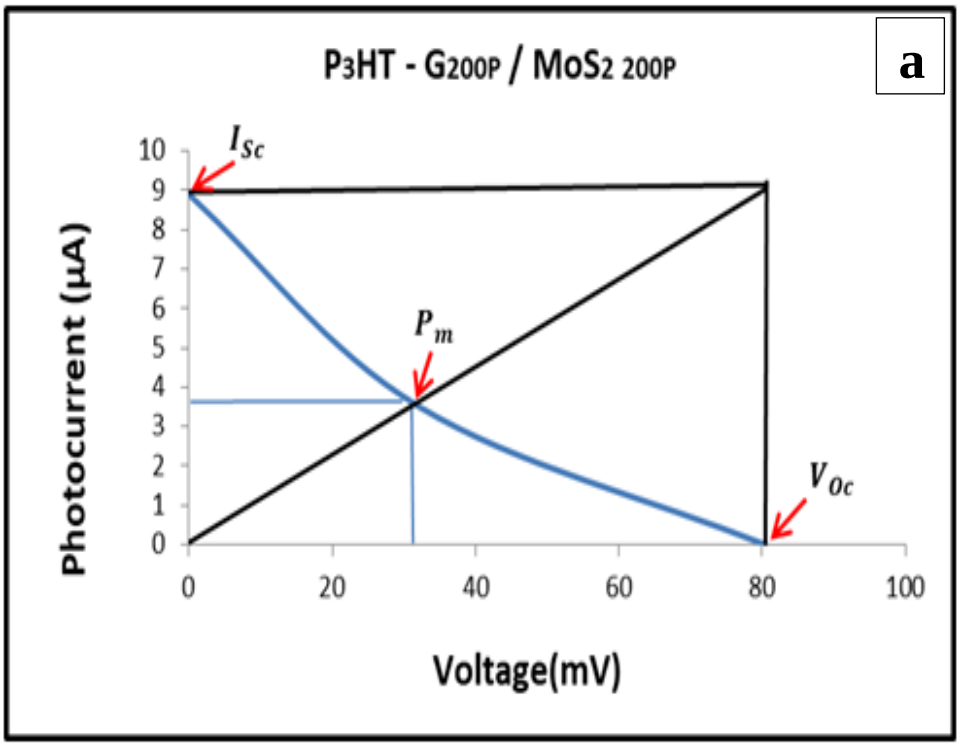

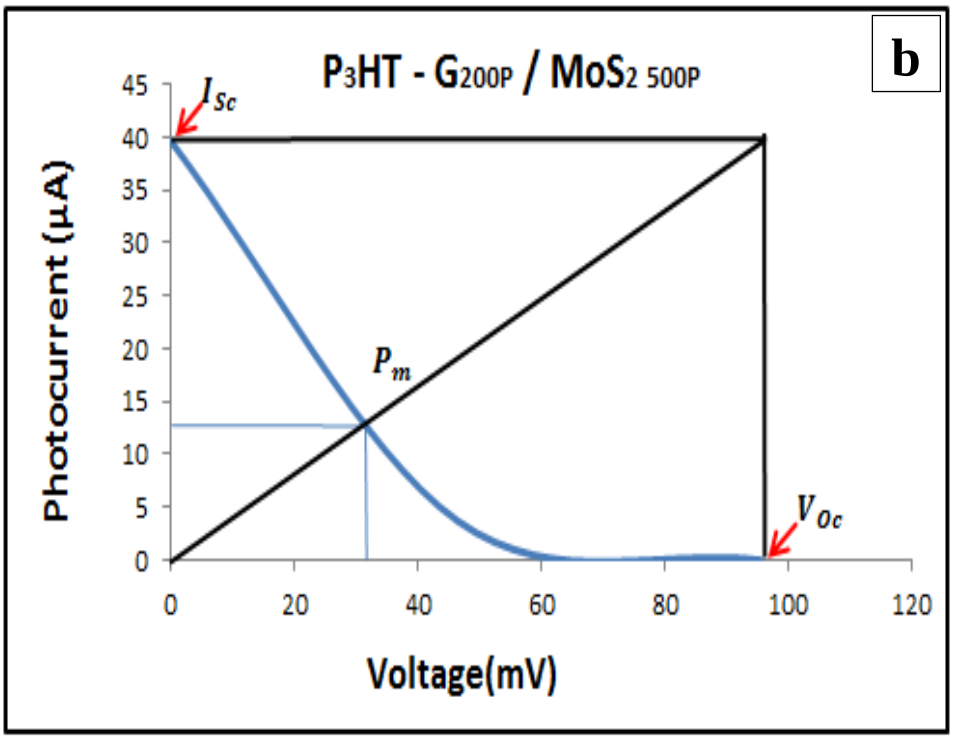
b
P3HT - G200P / MoS2 500P
Photocurrent (µA)
Voltage(mV)
I_{Sc}
P_m
V_{Oc}
0
5
10
15
20
25
30
35
40
45
0
20
40
60
80
100
120

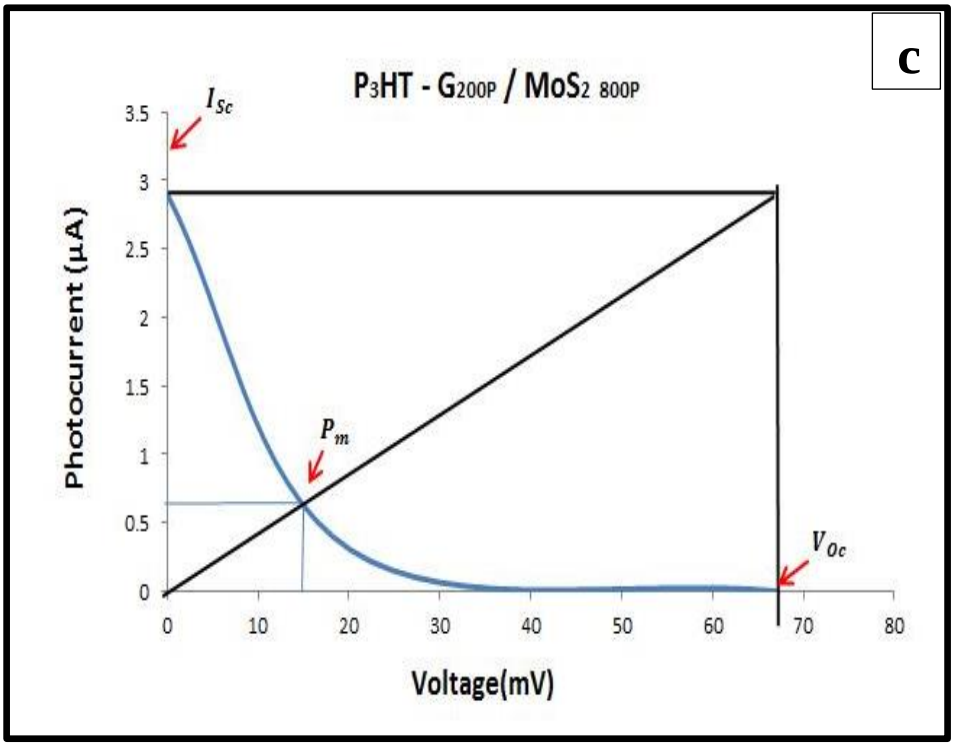
c
P3HT - G200P / MoS2 800P
Photocurrent (µA)
Voltage(mV)
I_{Sc}
P_m
V_{Oc}
0
0.5
1
1.5
2
2.5
3
3.5
0
10
20
30
40
50
60
70
80

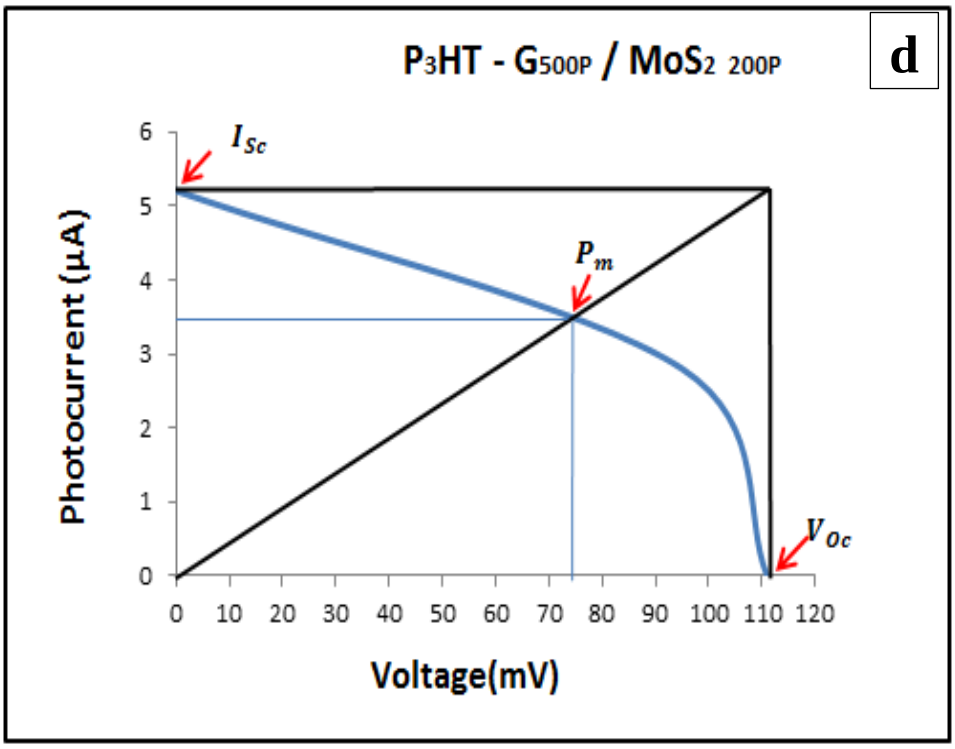
P3HT - G500P / MoS2 200P
d
Photocurrent (µA)
Voltage(mV)
I_{Sc}
P_m
V_{Oc}
0
1
2
3
4
5
6
0 10 20 30 40 50 60 70 80 90 100 110 120

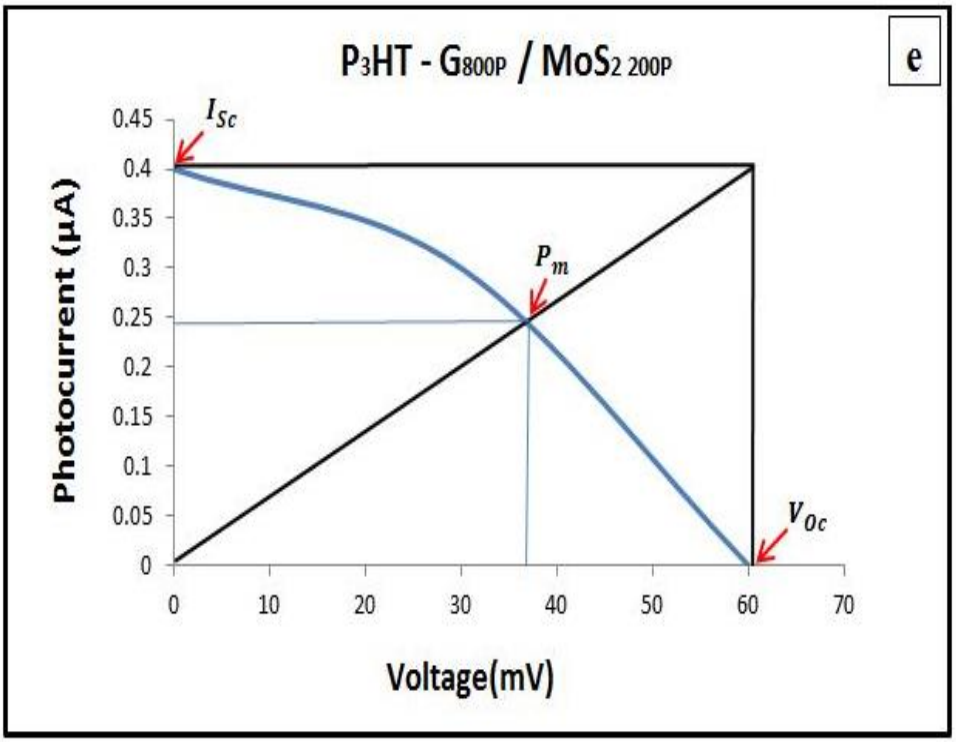
P3HT - G800P / MoS2 200P
e
Photocurrent (µA)
Voltage(mV)
I_{Sc}
P_m
V_{Oc}
0
0.05
0.1
0.15
0.2
0.25
0.3
0.35
0.4
0.45
0 10 20 30 40 50 60 70

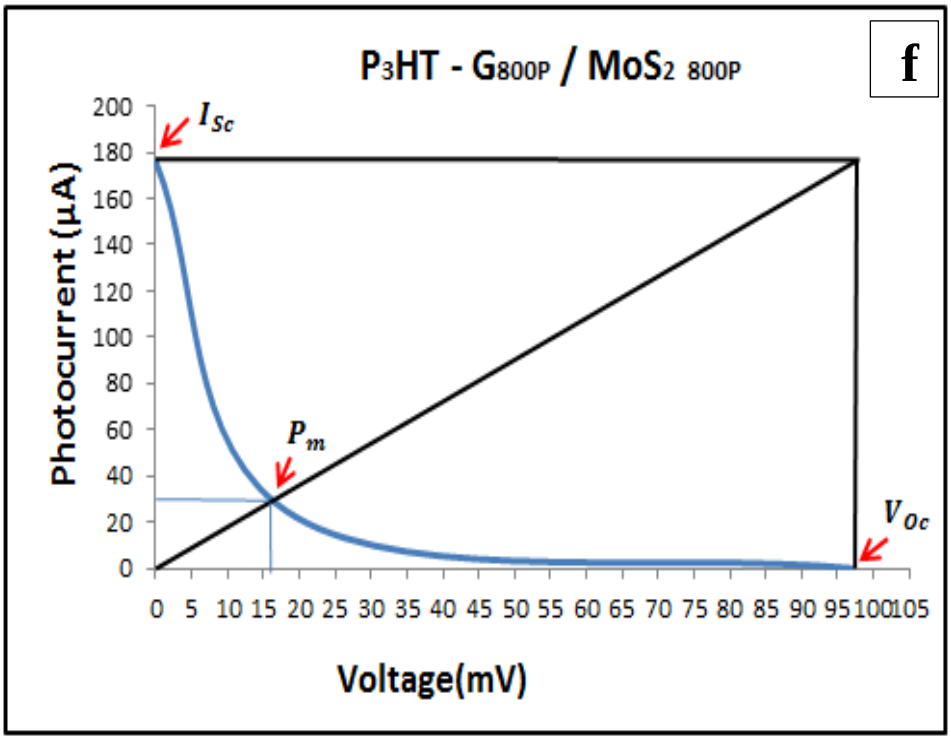

Figure (4.22): I-V Characteristic of Solar Cell under Illumination of Ag/PSi/P_3HT–G/MoS_2/Ag at the Number Different Laser Pulses.

Table(4.8): Shows the Solar Cell Parameters for all the Prepared Films.

Heterojunction (Solar cell)	V_{oc} (mV)	I_{sc} (µA)	V_m (mV)	I_m (µA)	F.F %	η%
Ag/PSi/P_3HT – G_{200P} /$MoS_{2\ 200P}$/Ag	80.5	8.9	32.2	3.5	15.7	1.43
Ag/PSi/P_3HT – G_{800P} /$MoS_{2\ 800P}$/Ag	97	176	16	30	2.8	6.11
Ag/PSi/P_3HT – G_{200P} /$MoS_{2\ 500P}$/Ag	95.6	40	28	14	10.2	4.99
Ag/PSi/P_3HT – G_{200P} /$MoS_{2\ 800P}$/Ag	67	2.7	14.9	0.53	4.3	0.100
Ag/PSi/P_3HT – G_{500P} /$MoS_{2\ 200P}$/Ag	111	5.2	73	3.5	44.2	3.25
Ag/PSi/P_3HT – G_{800P} /$MoS_{2\ 200P}$/Ag	60	0.4	37	0.229	35.3	0.107

4.7 Photodetector Parameters Measurement

4.7.1 The Spectral Responsivity (R_λ)

Equation (2-21) was used to determine the spectral responsivity of structures in the (350-1000) nm wavelength range at a (3)V bias voltage.

The structure of Ag/PSi/P_3HT–G/MoS_2/Ag consists of three heterojunctions, the first heterojunction is between the Ag layer and porous silicon (Ag/PSi) and the second heterojunction is made between the porous silicon layer and thin film P_3HT–G/MoS_2, The third heterojunction is between thin film P_3HT–G /MoS_2 and the Ag layer. Therefore the Ag/PSi/P_3HT–G/MoS_2/Ag have three depletions regions.

Figures 4.23 (a-f) show the spectral responsivity plots as a function of the wavelength of the Ag/PSi/P_3HT–G/MoS_2/Ag structure prepared at different laser pulses. Figures show that the spectral responsivity curve of Ag/PSi/P_3HT–G/MoS_2/Ag consists of several peaks of response; the maximal peak at (900) nm is due to the absorption edge of silicon which is in agreement with the previous studies [146]. The peak is located at (760) nm due to the absorption edge of P_3HT–G/MoS_2 nanocomposite. It was observed from the figures that the spectral response of the silicon absorption edge will increase from (0.06) A/W at the wavelength of (900) nm for the sample Ag/PSi/P_3HT–G_{200P}/$MoS_{2\ 800P}$/Ag to (0.36) A/W at the wavelength of (900) nm for the sample Ag/PSi/P_3HT-G_{800P}/$MoS_{2\ 800P}$/Ag.

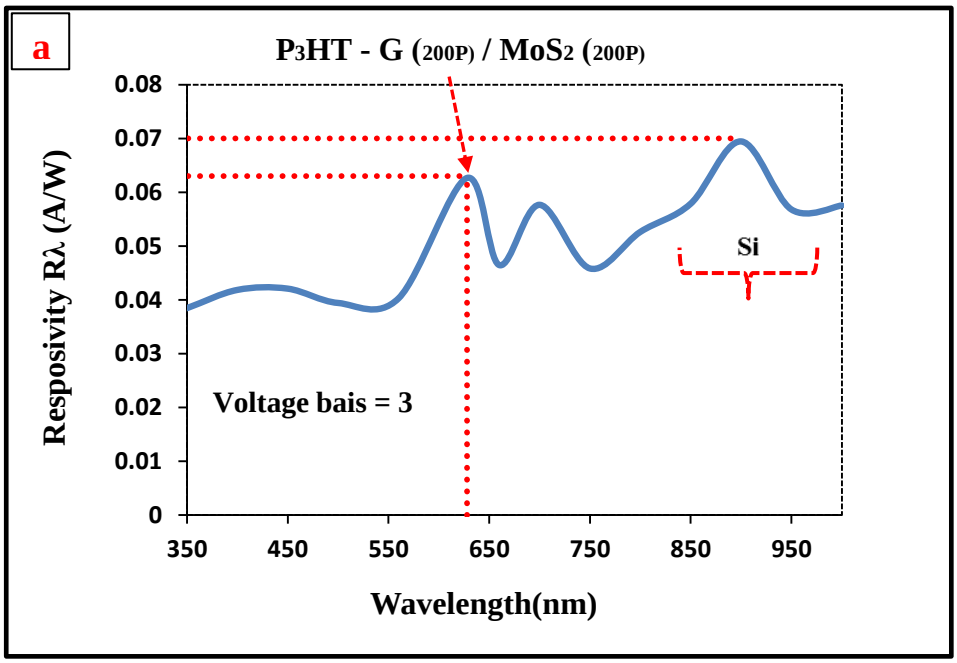
a
P3HT - G (200P) / MoS2 (200P)
Resposivity Rλ (A/W)
0.08
0.07
0.06
0.05
0.04
0.03
0.02
0.01
0
Voltage bais = 3
Si
350
450
550
650
750
850
950
Wavelength(nm)

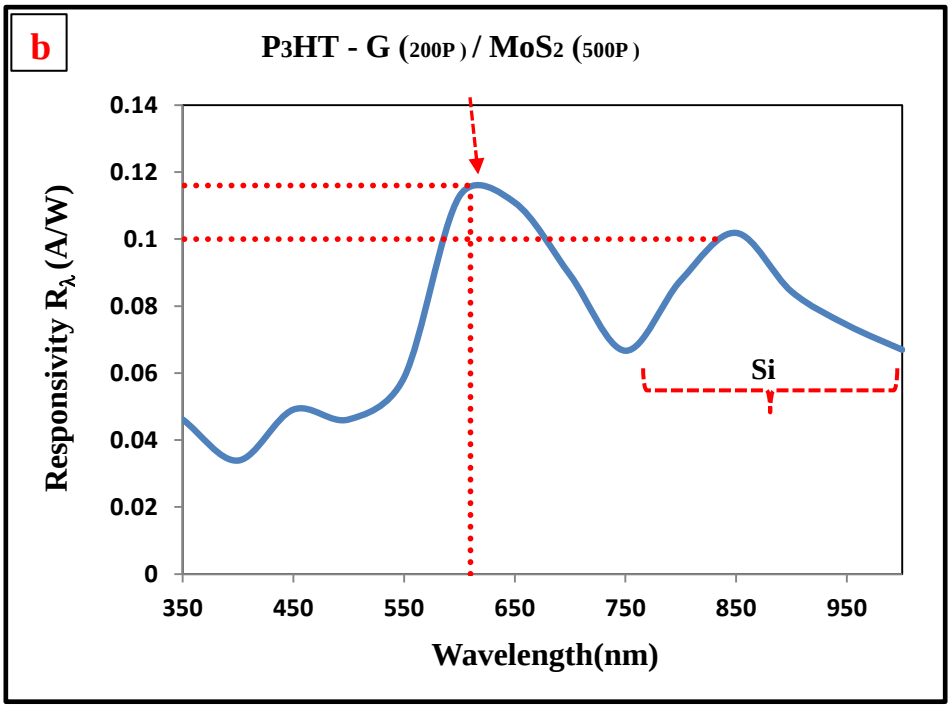
b
P3HT - G (200P) / MoS2 (500P)
Responsivity Rλ (A/W)
0.14
0.12
0.1
0.08
0.06
0.04
0.02
0
Si
350
450
550
650
750
850
950
Wavelength(nm)

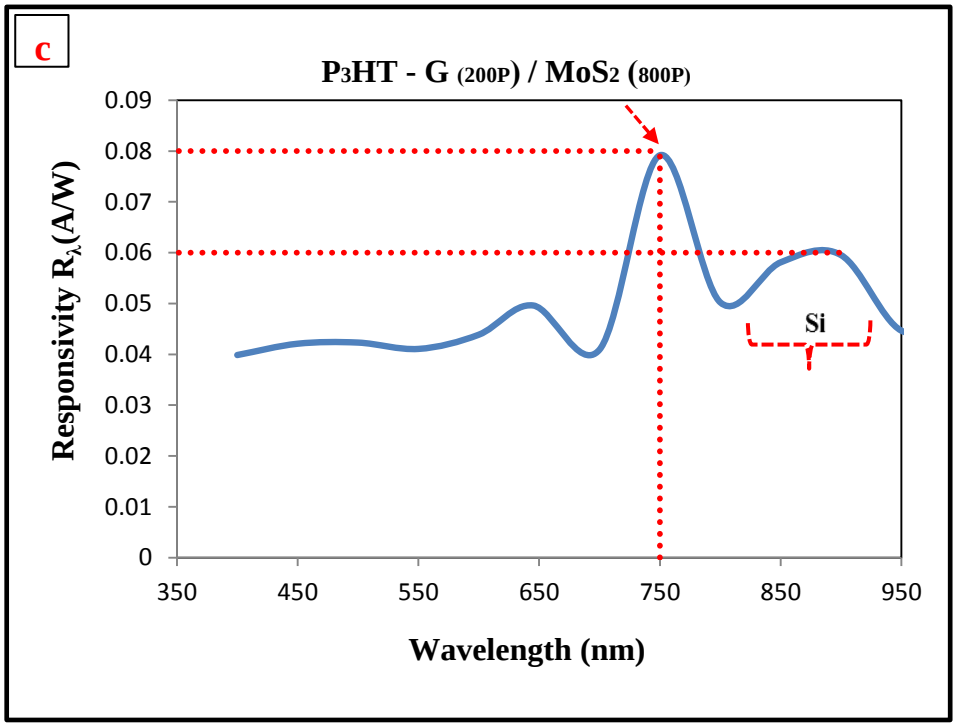
c
P3HT - G (200P) / MoS2 (800P)
Responsivity Rλ(A/W)
0.09
0.08
0.07
0.06
0.05
0.04
0.03
0.02
0.01
0
350
450
550
650
750
850
950
Si
Wavelength (nm)

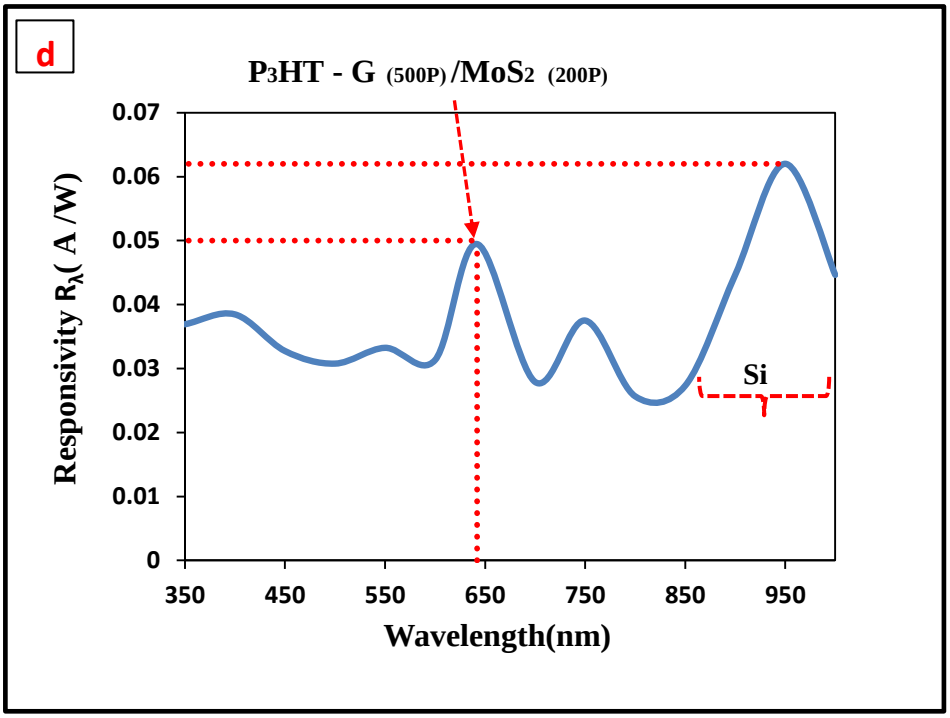
d
P3HT - G (500P) /MoS2 (200P)
Responsivity Rλ(A /W)
0.07
0.06
0.05
0.04
0.03
0.02
0.01
0
350
450
550
650
750
850
950
Si
Wavelength(nm)

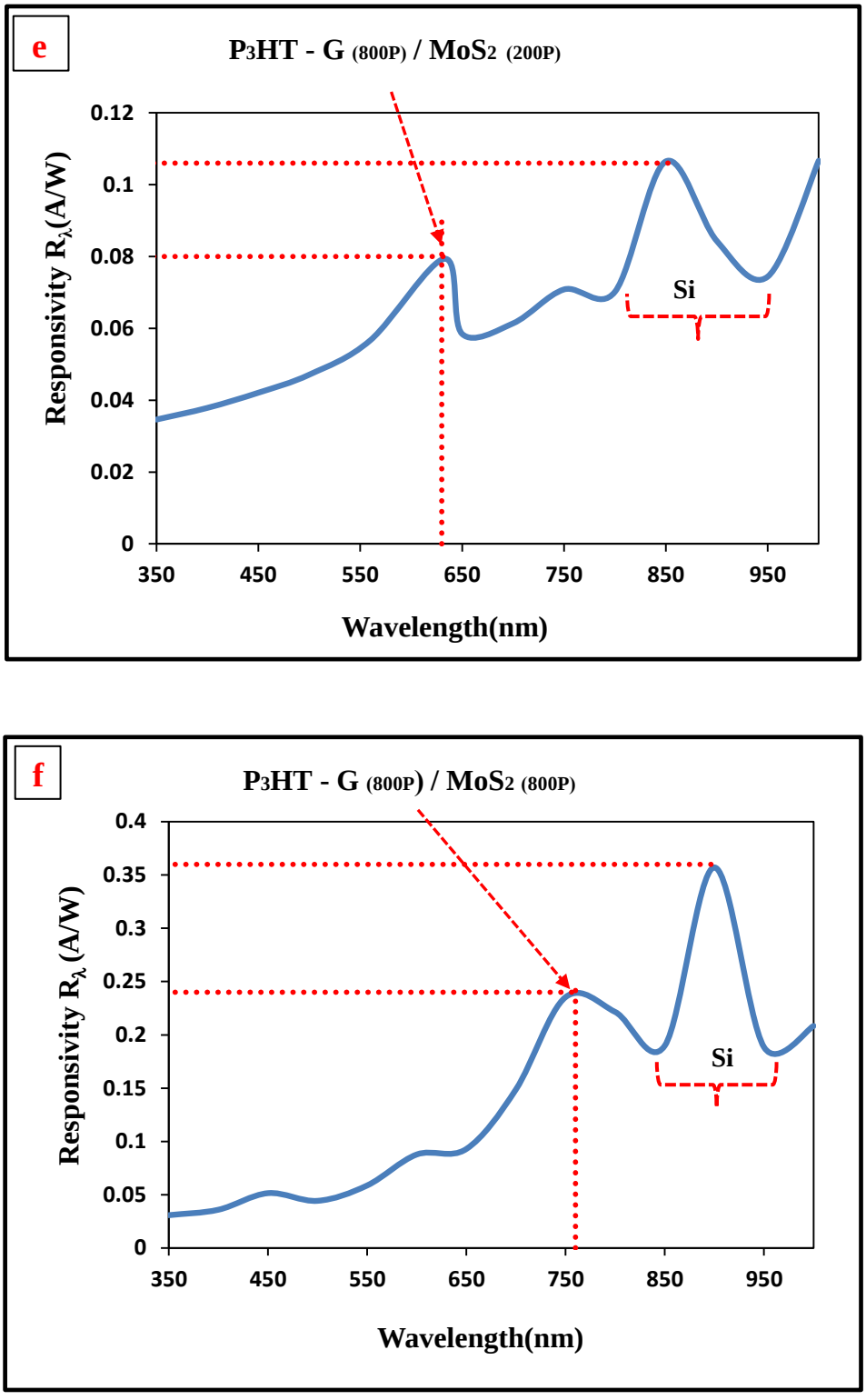

Figure (4.23): Responsivity as a Function of Wavelength of Ag/PSi/P_3HT – G /MoS_2 /Ag Photodetectors at Different Laser Pulses.

According to the results, the P_3HT-G/MoS_2 film may absorb light with greater energy, such as (600–700) nm. Whereas light with lower energy, such as (800–900) nm, can completely incident into the Si substrate and is absorbed. These results are due to the absorption edges P_3HT–G/MoS_2 and P-Si. As a result, the responsivity of the photodetector will rise from (0.05) A/W to over (0.24) A/W. This improvement can be ascribed to increasing light absorption, the smaller depletion region and decreasing the dark current.

4.7.2 Specific Detectivity (D)*

Specific detectivity is an important parameter for a photodetector which represents a minimum detectable power therefore; the performance of the detector is linked with this parameter. Equation (2-25) was used to determine the specific detectivity.

Figures 4.24(a-f) show the specific detectivity as a function of wavelength for Ag/P-Si/P_3HT–G /MoS_2 /Ag photodetectors at different laser pulses. These figures show that the specific detectivity depends directly on responsivity. The maximum for specific detectivity was found to be (3.39×10^{12}) cm.$Hz^{1/2}W^{-1}$ at wavelength (760) nm for Ag/PSi/P_3HT–G_{800P}/$MoS_{2\ 800P}$/Ag photodetector.

It was observed from the figures that the specific detectivity of the silicon absorption edge will increase from (8.6×10^{11}) cm.$Hz^{1/2}$.W^{-1} at the wavelength of 900 nm for the sample Ag/PSi/P_3HT-G_{200P} /$MoS_{2\ 800P}$/Ag to (5.1×10^{12}) cm.$Hz^{1/2}$.W^{-1} at the wavelength of (900) nm for the sample Ag/PSi/P_3HT-G_{800P}/$MoS_{2\ 800P}$/Ag.

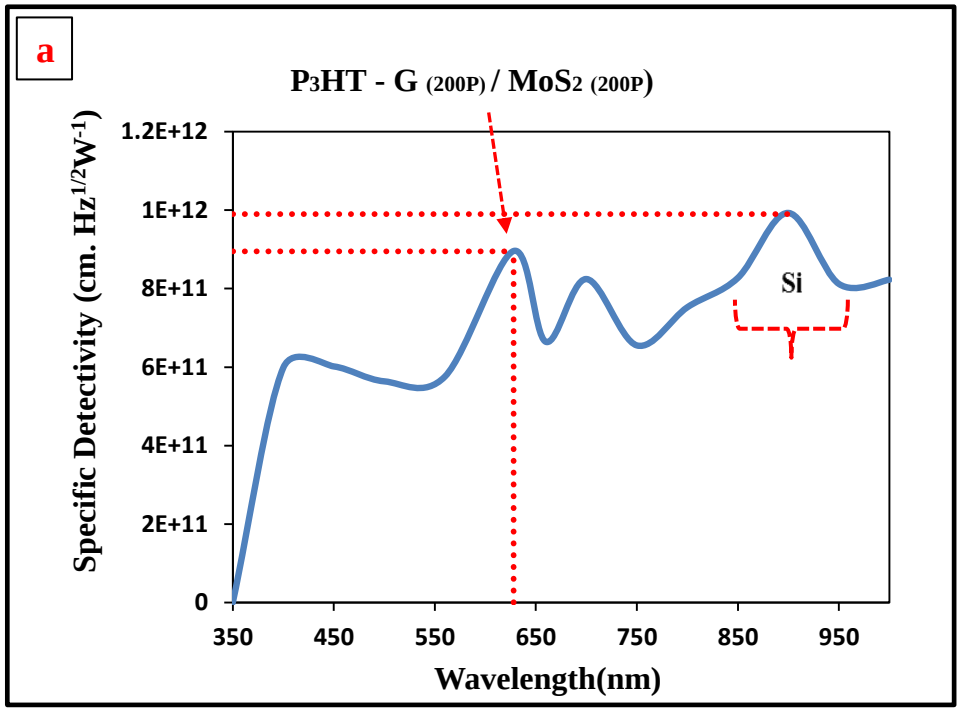
a
P3HT - G (200P) / MoS2 (200P)
Specific Detectivity (cm. Hz1/2W-1)
1.2E+12
1E+12
8E+11
6E+11
4E+11
2E+11
0
350
450
550
650
750
850
950
Wavelength(nm)
Si

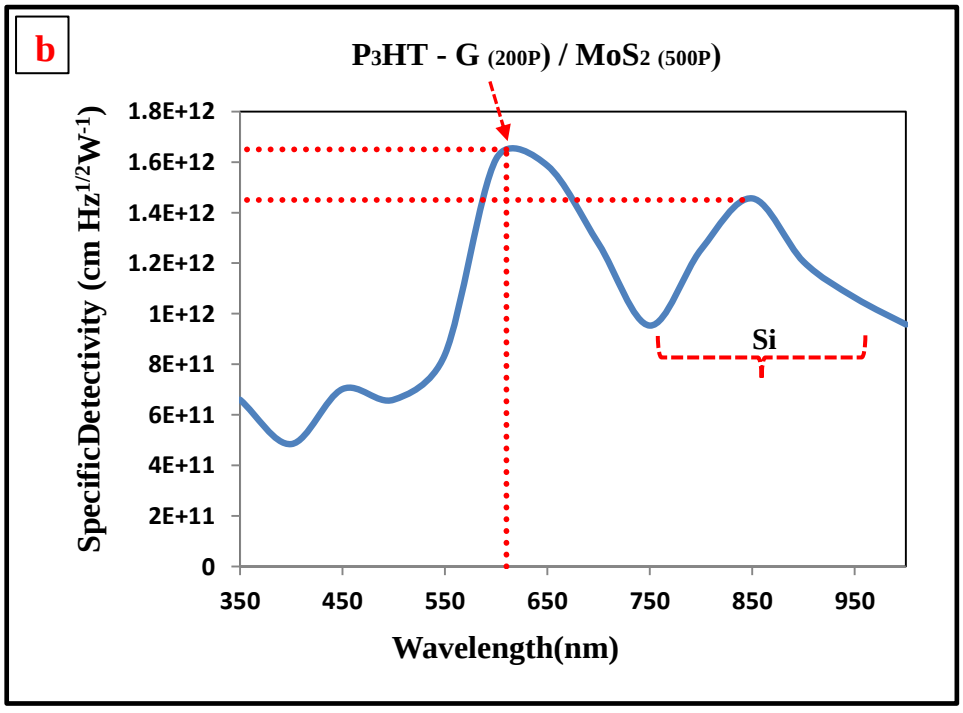
b
P3HT - G (200P) / MoS2 (500P)
SpecificDetectivity (cm Hz1/2W-1)
1.8E+12
1.6E+12
1.4E+12
1.2E+12
1E+12
8E+11
6E+11
4E+11
2E+11
0
350
450
550
650
750
850
950
Wavelength(nm)
Si

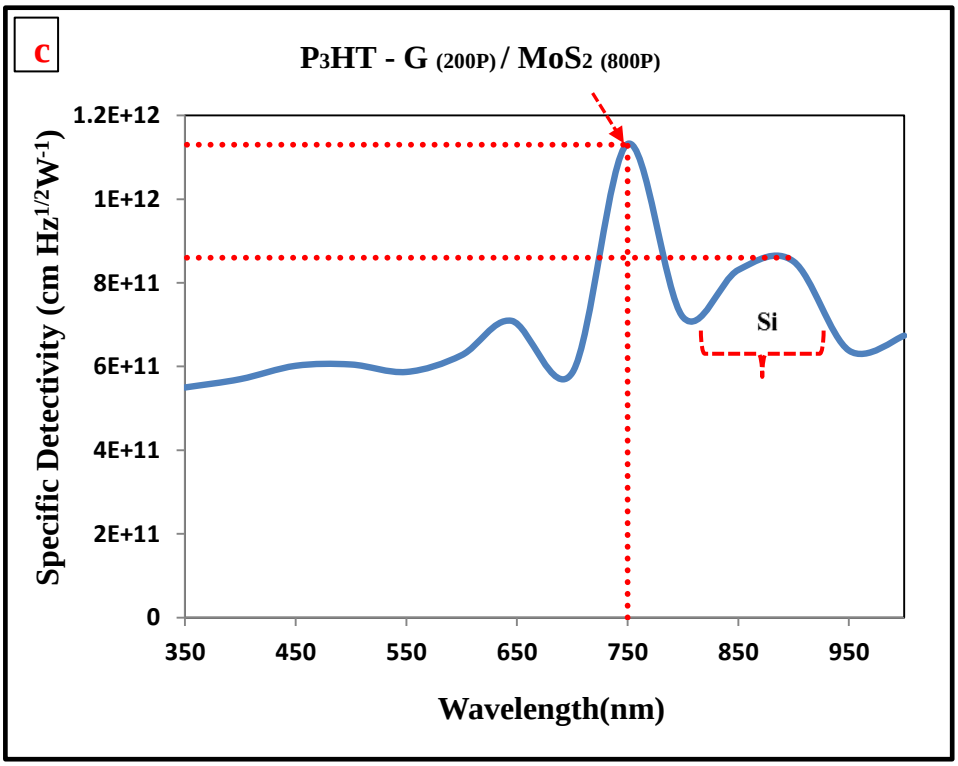
c
P3HT - G (200P) / MoS2 (800P)
Specific Detectivity (cm Hz1/2W-1)
1.2E+12
1E+12
8E+11
6E+11
4E+11
2E+11
0
350
450
550
650
750
850
950
Si
Wavelength(nm)

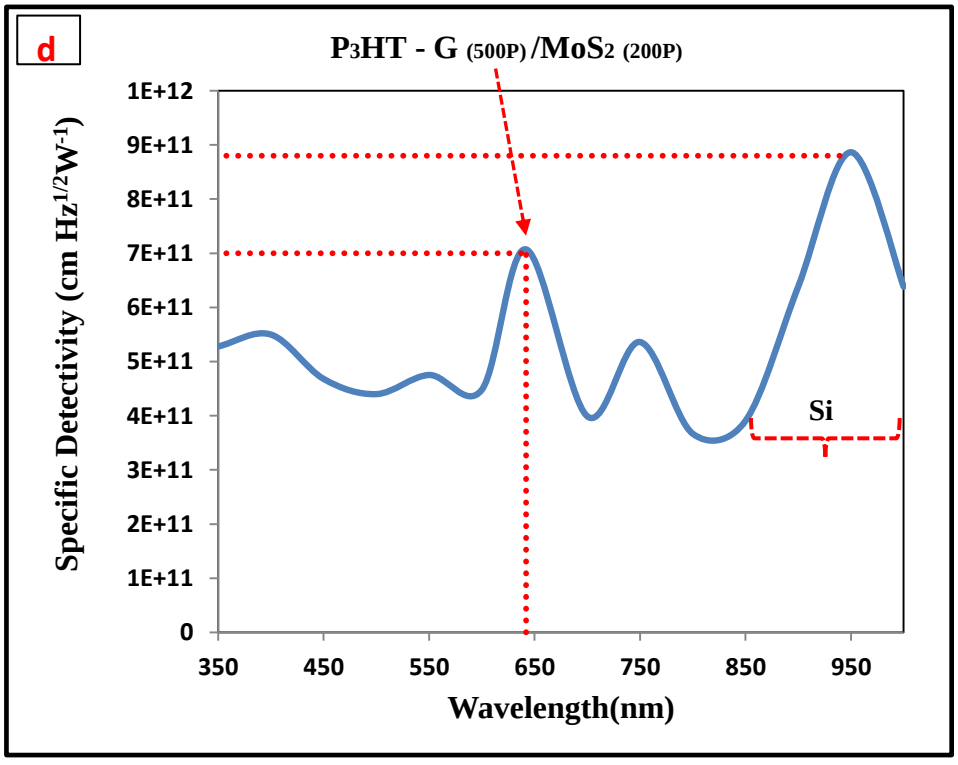
d
P3HT - G (500P) /MoS2 (200P)
Specific Detectivity (cm Hz1/2W-1)
1E+12
9E+11
8E+11
7E+11
6E+11
5E+11
4E+11
3E+11
2E+11
1E+11
0
350
450
550
650
750
850
950
Si
Wavelength(nm)

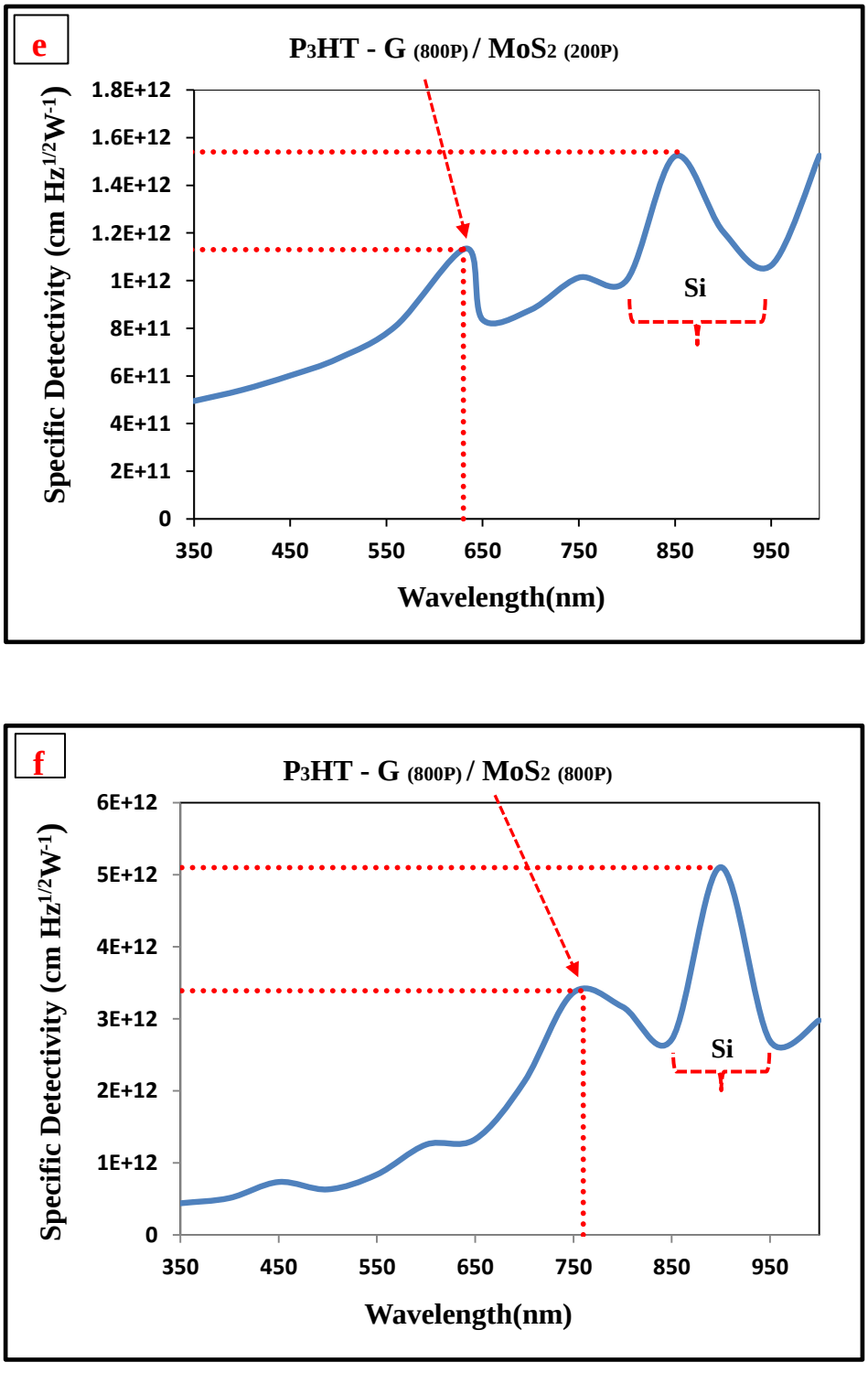

Figure (4.24): Specific Detectivity Plots for Ag/PSi/P_3HT – G /MoS_2 /Ag Photodetectors at Different Laser Pulses.

4.7.3 Quantum Efficiency

Equation (2-27) was used to determine the quantum efficiency. Figures 4.25(a-f) show the quantum efficiency as a function of wavelength (350–1000) nm of structure Ag/PSi/P_3HT–G/MoS_2/Ag. According to the data we gathered, the greatest peak quantum efficiency for Ag/PSi/P_3HT-G_{800P}/$MoS_{2\ 800P}$/Ag was 38.9 % at 760 nm. This is because there is more absorption in this region, which causes more carriers to be generated in the depletion zone, increasing spectrum sensitivity and, ultimately, quantum efficiency. The results of the detector parameters of structure Ag/PSi/P_3HT–G/MoS_2/Ag at different laser pulses are shown in Table (4.9).

According to the data, the quantum efficiency of the silicon absorption edge improves from 8.5% at 950 nm to 49.2% for the Ag/PSi/P_3HT-G_{800P}/$MoS_{2\ 800P}$/Ag sample at 900 nm. The improvement in quantum efficiency is due to the use of 800 pulses for each of MoS_2 and G resulted in a more uniform and dense nanocomposite, which has a higher absorption coefficient and a higher surface area. This resulted in a higher quantum efficiency of 49.2%.

Table (4.10) lists the specifications for all the films created and for the silicon absorption edge photodetectors that have been improved by the P_3HT-G/MoS_2 nanocomposite.

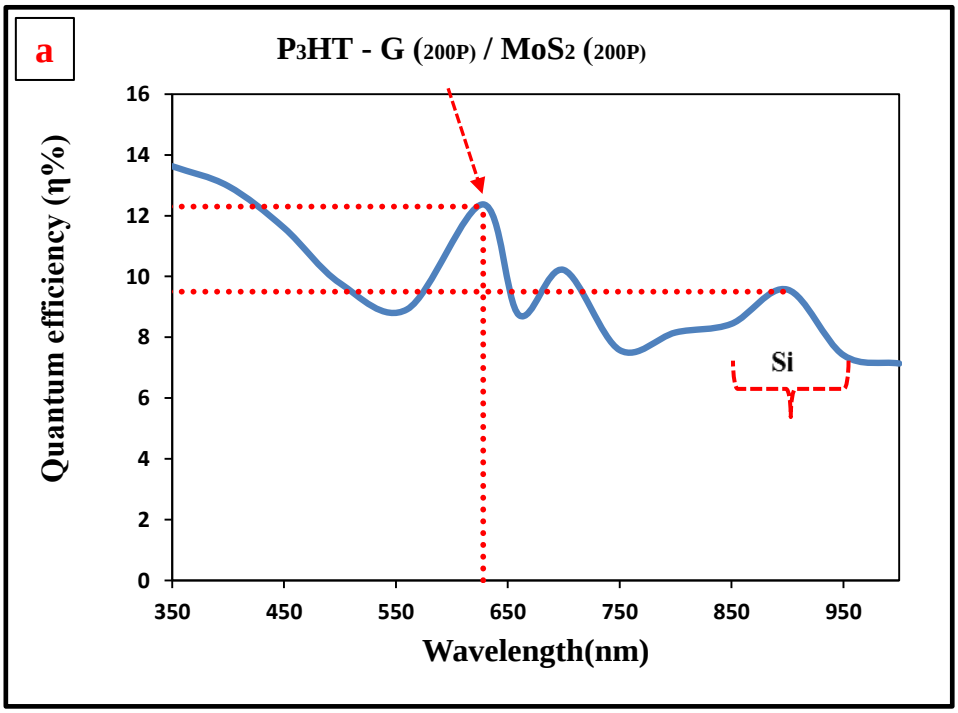
a
P3HT - G (200P) / MoS2 (200P)
Quantum efficiency (η%)
16
14
12
10
8
6
4
2
0
350
450
550
650
750
850
950
Wavelength(nm)
Si

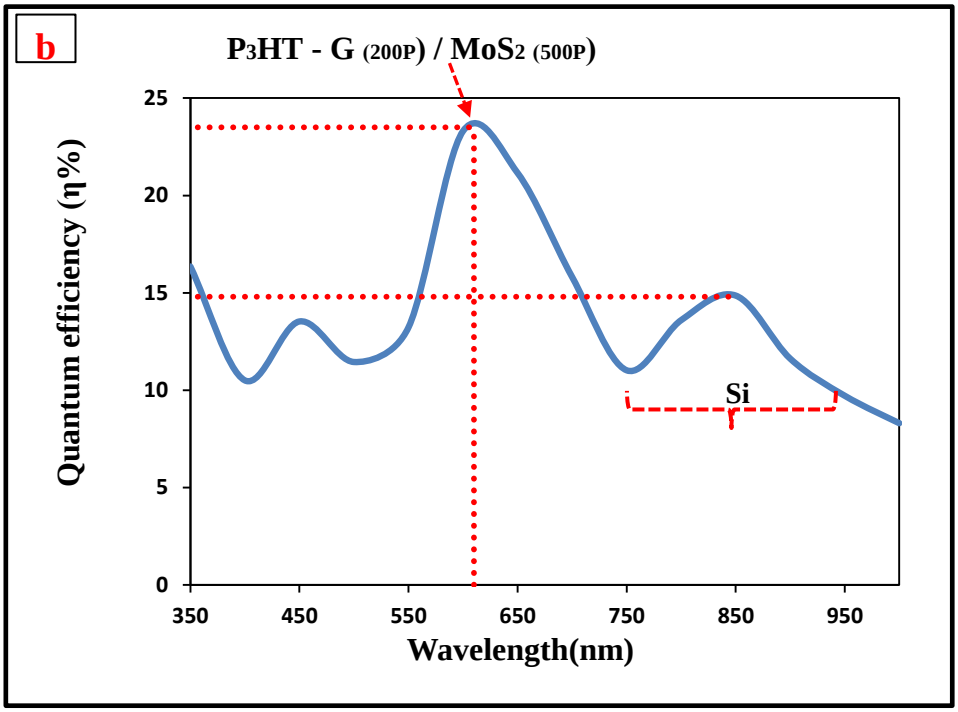
b
P3HT - G (200P) / MoS2 (500P)
Quantum efficiency (η%)
25
20
15
10
5
0
350
450
550
650
750
850
950
Wavelength(nm)
Si

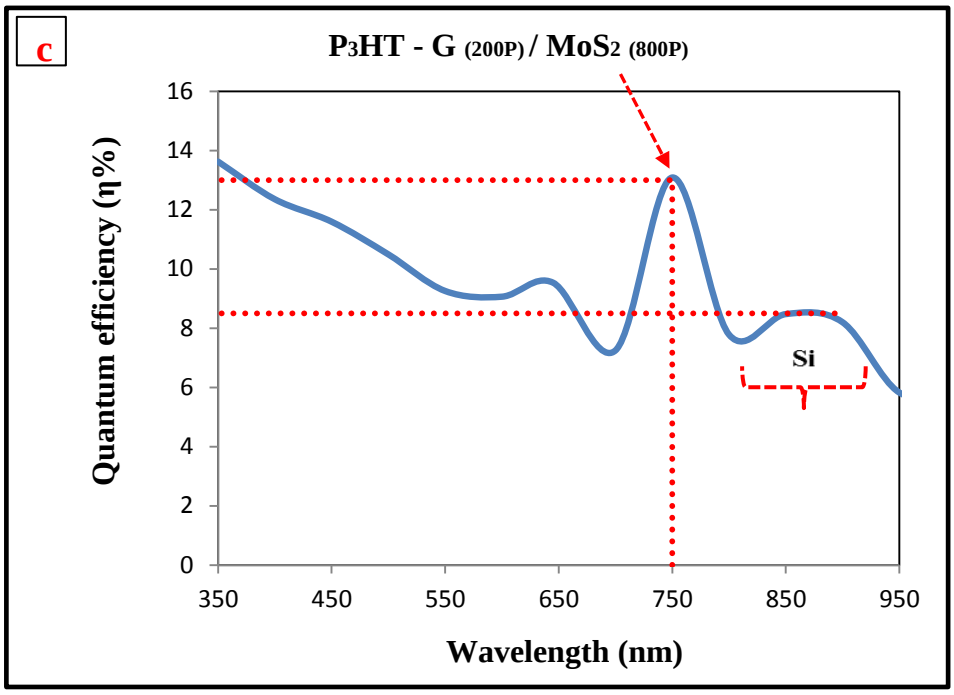
c
P3HT - G (200P) / MoS2 (800P)
Quantum efficiency (η%)
16
14
12
10
8
6
4
2
0
350
450
550
650
750
850
950
Si
Wavelength (nm)

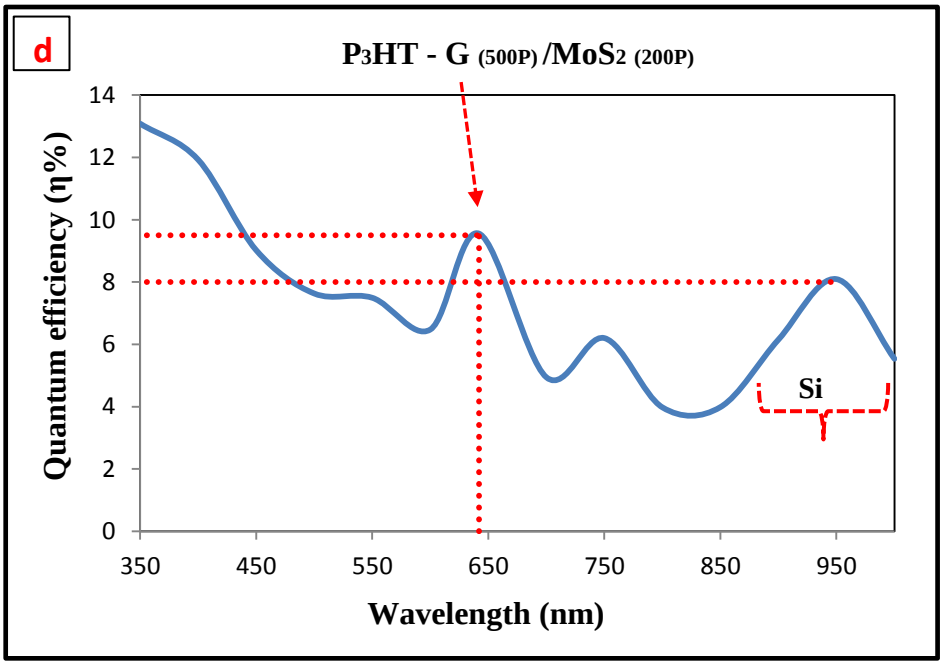
d
P3HT - G (500P) /MoS2 (200P)
Quantum efficiency (η%)
14
12
10
8
6
4
2
0
350
450
550
650
750
850
950
Si
Wavelength (nm)

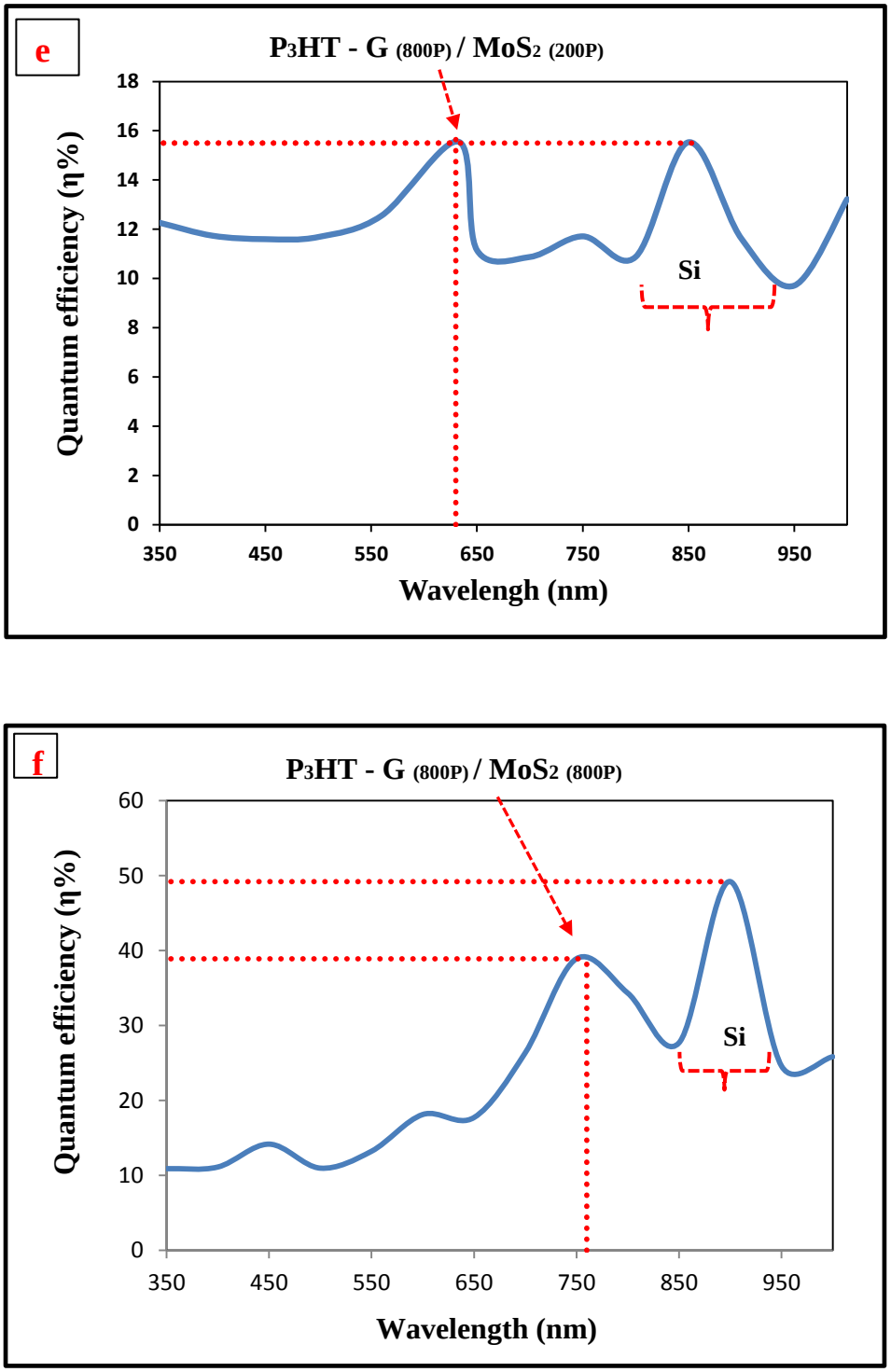

Figure (4.25): Quantum Efficiency for Ag/PSi/P_3HT – G /MoS_2 /Ag Photodetectors at Different Laser Pulses.

Table (4.9): Shows the Photodetector Parameters to the Absorption Edge of P_3HT – G /MoS_2 Nanoparticles for all the Films Prepared.

Heterojunction (Photodetectors)	**Wavelength (nm)**	**Responsivity Rλ (A/W)**	**Specific Detectivity D^* ($cm.Hz^{1/2}.W^{-1}$)**	**Quantum Efficiency η %**
Ag/P_3HT – G_{200P} /$MoS_{2\ 200P}$/ PSi/Ag	628	0.063	8.95×10^{11}	12.3
Ag/P_3HT – G_{800P} /$MoS_{2\ 800P}$/ PSi/Ag	760	0.24	3.39×10^{12}	38.9
Ag/P_3HT – G_{200P} /$MoS_{2\ 500P}$/ PSi/Ag	610	0.116	1.65×10^{12}	23.5
Ag/P_3HT – G_{200P} /$MoS_{2\ 800P}$/ PSi/Ag	750	0.08	1.13×10^{12}	13.0
Ag/P_3HT – G_{500P} /$MoS_{2\ 200P}$/ PSi/Ag	642	0.05	7.0×10^{11}	9.5
Ag/P_3HT – G_{800P} /$MoS_{2\ 200P}$/ PSi/Ag	633	0.08	1.13×10^{12}	15.5

Table (4.10): Shows the Parameters of the Photodetector of the Silicon Absorption Edge Enhanced by $P_3HT - G / MoS_2$ Nanocomposite and for all Prepared Films.

Heterojunction (Photodetectors)	**Wavelength (nm)**	**Responsivity R_λ (A/W)**	**Specific Detectivity D^* ($cm.Hz^{1/2}.W^{-1}$)**	**Quantum Efficiency η%**
$Ag/P_3HT - G_{200P} /MoS_{2\ 200P}/PSi/Ag$	900	0.07	9.9×10^{11}	9.5
$Ag/P_3HT - G_{800P} /MoS_{2\ 800P}/ PSi/Ag$	900	0.36	5.1×10^{12}	49.2
$Ag/P_3HT - G_{200P} /MoS_{2\ 500P}/ PSi/Ag$	850	0.1	1.45×10^{12}	14.8
$Ag/P_3HT - G_{200P} /MoS_{2\ 800P}/ PSi/Ag$	900	0.06	8.6×10^{11}	8.5
$Ag/P_3HT - G_{500P} /MoS_{2\ 200P}/ PSi/Ag$	950	0.062	8.8×10^{11}	8
$Ag/P_3HT - G_{800P} /MoS_{2\ 200P}/ PSi/Ag$	860	0.106	1.5×10^{12}	15.5

Table(4.11): Shows the Comparison Between Our Work and Previous Studies for Fabricating Polymer / MoS_2 / Graphene by Different Methods and use in Optoelectronic Applications.

Design	Year	Method Device fabrication	Application type	Ref.
Ag–Nps/graphene/Si	2014	CVD	photodetector	[147]
MoS_2	2014	thermal decomposition of $(NH4)_2MoS_4$	dye-sensitized solar cells	[148]
MoS_2 /grapheme heterostructure	2015	Facile hydrothermal	photodetector	[51]
MoS_2 /grapheme	2015	G:ME MoS_2 :ME	photodetector	[14]
MoS_2 \ ITO	2015	Chemically exfoliated	solar cells	[149]
MoS_2/graphene/silicon	2015	G : Low-pressure chemical vapor deposition method@ MoS_2:It is spin-coated onto a silicon surface	solar cells	[150]
N- MoS_2 /p-Si with Al_2O_3 passivation	2016	CVD	solar cells	[52]
P_3HT–graphene/Si	2018	CVD	photodetector	[55]
Graphene/Si				
MoS_2/grapheme	2018	CVD	photodetector	[151]
Poly (3-hexylthiophene)/ graphene	2019	spin-coating	photodetector	[152]
grapheme / MoS_2/grapheme	2019	G:CVD &MoS2:CVD	photodetector	[153]
PEDOT: PSS/MoS_2	2019	Mechanical Exfoliation	organic solar cells	[57]

MoS_2 /graphene nanocomposites	2020	Facile hydrothermal	dye-sensitized solar cells	[59]
polymer–graphene	2020	spin-coating	gas detector	[154]
grapheme / MoS_2/grapheme	2020	G:CVD&Dry transfer	photodetector	[155]
PVA/G/Ag	2021	PLAL	photodetector	[60]
PMMA/G/Ag				
graphene/MoS_2 interfacial layer/n-Si	2021	using pre-annealed sulfurized Mo foil	solar cells	[63]
MoS_2/SnO_2 heterojunction	2022	PLD	photodetector	[67]
P_3HT:PCBM mixture	2022	spin-coating deposition	Organic Solar Cells	[156]
2D MoS_2/1D MWCNT	2023	Mechanical Exfoliation	photodetector	[69]
P_3HT:PCBM layer @ PEDOT:PSS layer	2023	spin-coating deposition	Heterojunction Solar Cells	[157]
P_3HT-G/MoS_2 nanocomposite	2023	PLAL	solar cells	Our work
			photodetector	

4.8 Conclusions

This study successfully prepared a ternary compound of P_3HT, G, and MoS_2 using the laser ablation method for the first time. Investigations were done into how the quantity of laser pulses affected the compound's structural, morphological, and optical characteristics. The UV-Vis data showed that when the number of laser pulses increased, there was an increase in absorbance because of the higher concentration of nanoparticles.

Through the results of the photodetector parameters, it is noticed that an increase in the number of laser ablation pulses for both the graphene and MoS_2 target will increase the spectral responsivity, specific detectivity and quantum efficiency. It was observed that all the prepared films have responsivity extended from visible to near-infrared region. The maximum value of the spectral responsivity, specific detectivity and quantum efficiency of Ag/P-Si /P_3HT-G/MoS_2/Ag photodetector is around 0.24 A/W, 3.39×10^{12} $cm.Hz^{1/2}.W^{-1}$ and 38.9% respectively at 760 nm wavelength due to the absorption edge of G NP_S, MoS_2 NP_S. On the other hand, The highest spectral responsivity, specific detectivity and quantum efficiency is around 0.36 A/W, 5.1×10^{12} $cm.Hz^{1/2}.W^{-1}$ and 49.2% respectively at 900nm due to silicon absorption edge. This indicates that sample Ag/P-Si/P_3HT–G_{800P}/MoS_2 $_{800P}$/Ag is the best concentration of nanocomposite as a reagent and also as an enhancer for silicon nanowires photodetector.

The incorporation of graphene and molybdenum nanoparticles with the semiconducting polymer P_3HT can significantly improve the electrical properties of solar cells, where the study demonstrated that the Ag/PSi/P_3HT-G_{800P}/MoS_2 $_{800P}$/Ag heterojunction achieved the highest

efficiency of 6.11%, which is a significant improvement over traditional solar cells.

4.9 Future works

From the obtained results we can suggest some point for future work:

1- Investigation of the effect of Thin film thickness for P_3HT/Au nanoparticles on solar cell efficiency.

2- Investigation the effects of different laser ablation parameters on the quantum efficiency of the MoS_2@Ag nanocomposite.

3- Investigate the use of quantum dots as sensitizers in solar cells.

4- Study the incorporation of nanoparticles indium tin oxide (ITO) nanoparticles, into transparent conductive films and used in solar cells.

References

[1] Chrisey, Douglas B., and Graham K. Hubler, eds. "Pulsed laser deposition of thin films." (1994): 3.

[2] Bäuerle, Dieter, and Dieter Bäuerle. "Surface melting." Laser Processing and Chemistry (2000): 165-183.

[3] Fogarassy, Eric, and Sylvain Lazare. "Laser ablation of electronic materials: basic mechanisms and applications." (No Title) (1992).

[4] Gallais, Laurent, and Jean-Yves Natoli. "Optimized metrology for laser-damage measurement: application to multiparameter study." Applied Optics 42, no. 6 (2003): 960-971.

[5] Mittal, K. L., ed. Particles on surfaces. Plenum., 1988.

[6] Wu, X., E. Sacher, and M. Meunier. "Excimer laser induced removal of particles from hydrophilic silicon surfaces." The Journal of Adhesion 70, no. 1-2 (1999): 167-178.

[7] Arnold, N. "Dry laser cleaning of particles by nanosecond pulses: theory." In Laser Cleaning, pp. 51-102. 2002.

[8] Perrière, Jacques, Eric Millon, and Eric Fogarassy, eds. "Recent advances in laser processing of materials." (2006).

[9] Rai, Amritesh, Hema CP Movva, Anupam Roy, Deepyanti Taneja, Sayema Chowdhury, and Sanjay K. Banerjee. "Progress in contact, doping and mobility engineering of MoS_2: an atomically thin 2D semiconductor." Crystals 8, no. 8 (2018): 316.

[10] Cui, Qiuhong, Yijun Yang, Junmeng Li, Feng Teng, and Xi Wang. "Material and device architecture engineering toward high performance two-dimensional (2D) photodetectors." Crystals 7, no. 5 (2017): 149.

[11] Freedy, Keren M., and Stephen J. McDonnell. "Contacts for molybdenum disulfide: interface chemistry and thermal stability." Materials 13, no. 3 (2020): 693.

[12] Roy, Kallol, Medini Padmanabhan, Srijit Goswami, T. Phanindra Sai, Gopalakrishnan Ramalingam, Srinivasan Raghavan, and Arindam Ghosh. "Graphene–MoS_2 hybrid structures for multifunctional photoresponsive memory devices." Nature nanotechnology 8, no. 11 (2013): 826-830.

[13] Rahman, M. Saifur, Md Shamim Anower, Md Rabiul Hasan, Md Biplob Hossain, and Md Ismail Haque. "Design and numerical analysis of highly sensitive Au-MoS_2-graphene based hybrid surface plasmon resonance biosensor." Optics Communications 396 (2017): 36-43.

[14] De Fazio, Domenico, Ilya Goykhman, Duhee Yoon, Matteo Bruna, Anna Eiden, Silvia Milana, Ugo Sassi et al. "High responsivity, large-area graphene/MoS_2 flexible photodetectors." ACS nano 10, no. 9 (2016): 8252-8262.

[15] Radisavljevic, Branimir, Aleksandra Radenovic, Jacopo Brivio, Valentina Giacometti, and Andras Kis. "Single-layer MoS_2 transistors." Nature nanotechnology 6, no. 3 (2011): 147-150.

[16] Haynes, William M. "CRC handbook of chemistry and physics, (Internet Version 2011)." Taylor Francis Group: Boca Raton, FL.–2011 (2011).

[17] Yun, Won Seok, S. W. Han, Soon Cheol Hong, In Gee Kim, and J. D. Lee. "Thickness and strain effects on electronic structures of transition metal dichalcogenides: 2H-MX_2 semiconductors (M= Mo, W; X= S, Se, Te)." Physical Review B 85, no. 3 (2012): 033305.

[18] Dideikin, Artur T., and Alexander Y. Vul'. "Graphene oxide and derivatives: the place in graphene family." Frontiers in Physics 6 (2019): 149.

[19] Nurunnabi, Md, and Jason McCarthy, eds. Biomedical applications of graphene and 2D nanomaterials. Elsevier, 2019.

[20] Novoselov, Konstantin S., and A. K. Geim. "The rise of graphene." Nat. Mater 6, no. 3 (2007): 183-191.

[21] Mohammed, Musaab Khudhur, Amer Al-Nafiey, and Ghaleb Al-Dahash. "Manufacturing graphene and graphene-based nanocomposite for piezoelectric pressure sensor application: a review." Nano Biomedicine and Engineering 13, no. 1 (2021): 27-35.

[22] Bonaccorso, Francesco, Zhipei Sun, Tawfique Hasan, and A. C. Ferrari. "Graphene photonics and optoelectronics." Nature photonics 4, no. 9 (2010): 611-622.

[23] Huang, Hung-Lin, Ching-Ting Lee, and Hsin-Ying Lee. "Performance improvement mechanisms of P_3HT:PCBM inverted polymer solar cells using extra PCBM and extra P_3HT interfacial layers." Organic Electronics 21 (2015): 126-131.

[24] Erb, Tobias, Uladzimir Zhokhavets, Gerhard Gobsch, Sofiya Raleva, Bernd Stühn, Pavel Schilinsky, Christoph Waldauf, and Christoph J. Brabec.

"Correlation between structural and optical properties of composite polymer/fullerene films for organic solar cells." Advanced Functional Materials 15, no. 7 (2005): 1193-1196.

[25] Omer, B. M. "Optical Properties of Poly (3-hexylthiophene-2, 5-diyl) and Poly (3-hexylthiophene-2, 5-diyl)/(6, 6)-Phenyl C61-butyric Acid 3-ethylthiophene Ester Thin Films." Журнал нано-та електронної фізики 5,№ 3 (1) (2013): 03010-1.

[26] Mansour, Ahmed E., Ana M. Valencia, Dominique Lungwitz, Berthold Wegner, Naoki Tanaka, Yoshiaki Shoji, Takanori Fukushima, Andreas Opitz, Caterina Cocchi, and Norbert Koch. "Understanding the evolution of the Raman spectra of molecularly p-doped poly (3-hexylthiophene-2, 5-diyl): Signatures of polarons and bipolarons." Physical Chemistry Chemical Physics 24, no. 5 (2022): 3109-3118.

[27] Rauch, Tobias. Spectral enhancement of organic photodetectors. KIT Scientific Publishing, 2014.

[28] Choulis, Stelios A., Y. Kim, J. Nelson, D. D. C. Bradley, M. Giles, M. Shkunov, and I. McCulloch. "High ambipolar and balanced carrier mobility in regioregular poly (3-hexylthiophene)." Applied physics letters 85, no. 17 (2004): 3890-3892.

[29] Godovsky, D. Yu. "Device applications of polymer nanocomposites." Biopolymers· PVA hydrogels, anionic polymerization nano composites (2000): 163-205.

[30] Huisman, Carolien L., Albert Goossens, and Joop Schoonman. "Preparation of a nanostructured composite of titanium dioxide and polythiophene: a

new route towards 3D heterojunction solar cells." Synthetic metals 138, no. 1-2 (2003): 237-241.

[31] Shah, Arvind, Pedro Torres, Reto Tscharner, Nicolas Wyrsch, and Herbert Keppner. "Photovoltaic technology: the case for thin-film solar cells." science 285, no. 5428 (1999): 692-698.

[32] Goetzberger, Adolf, Christopher Hebling, and Hans-Werner Schock. "Photovoltaic materials, history, status and outlook." Materials science and engineering: R: Reports 40, no. 1 (2003): 1-46.

[33] Yan, M., L. J. Rothberg, E. W. Kwock, and T. M. Miller. "Interchain excitations in conjugated polymers." Physical review letters 75, no. 10 (1995): 1992.

[34] Cheng, Yen-Ju, Sheng-Hsiung Yang, and Chain-Shu Hsu. "Synthesis of conjugated polymers for organic solar cell applications." Chemical reviews 109, no. 11 (2009): 5868-5923.

[35] Krebs, Frederik C. "Fabrication and processing of polymer solar cells: A review of printing and coating techniques." Solar energy materials and solar cells 93, no. 4 (2009): 394-412.

[36] Coakley, Kevin M., and Michael D. McGhee. "Conjugated polymer photovoltaic cells." Chemistry of materials 16, no. 23 (2004): 4533-4542.

[37] Chen, Jiun-Tai, and Chain-Shu Hsu. "Conjugated polymer nanostructures for organic solar cell applications." Polymer Chemistry 2, no. 12 (2011): 2707-2722.

[38] Chamberlain, G. A. "Organic solar cells: A review." Solar cells 8, no. 1 (1983): 47-83.

[39] Zworykin, V. K., G. A. Morton, and L. Malter. "The secondary emission multiplier-a new electronic device." Proceedings of the Institute of Radio Engineers 24, no. 3 (1936): 351-375.

[40] Haugan, H. J., S. Elhamri, F. Szmulowicz, B. Ullrich, G. J. Brown, and W. C. Mitchel. "Study of residual background carriers in midinfrared InAs⁄GaSb superlattices for uncooled detector operation." Applied Physics Letters 92, no. 7 (2008).

[41] Lin, Jeng-Yu, Gentian Yue, Sheng-Yen Tai, Yaoming Xiao, Ho-Ming Cheng, Fu-Ming Wang, and Jihuai Wu. "Hydrothermal synthesis of graphene flake embedded nanosheet-like molybdenum sulfide hybrids as counter electrode catalysts for dye-sensitized solar cells." Materials Chemistry and Physics 143, no. 1 (2013): 53-59.

[42] Li, Xiaodong, Wenjun Zhang, Yulei Wu, Chao Min, and Junfeng Fang. "Solution-processed MoS_x as an efficient anode buffer layer in organic solar cells." ACS applied materials & interfaces 5, no. 18 (2013): 8823-8827.

[43] Yun, J.M., Noh, Y.J., Yeo, J.S., Go, Y.J., Na, S.I., Jeong, H.G., Kim, J., Lee, S., Kim, S.S., Koo, H.Y. and Kim, T.W., Efficient work-function engineering of solution-processed MoS_2 thin-films for novel hole and electron transport layers leading to high-performance polymer solar cells. Journal of Materials Chemistry C, 1(24), pp.3777-3783, 2013.

[44] Lei, B., G. R. Li, and X. P. Gao. "Morphology dependence of molybdenum disulfide transparent counter electrode in dye-sensitized solar cells." Journal of Materials Chemistry A 2, no. 11 (2014): 3919-3925.

[45] Yang, Xi, Weifei Fu, Wenqing Liu, Jinghua Hong, Yu Cai, Chuanhong Jin, Mingsheng Xu, Haibo Wang, Deren Yang, and Hongzheng Chen. "Engineering crystalline structures of two-dimensional MoS_2 sheets for high-performance organic solar cells." Journal of Materials Chemistry A 2, no. 21 (2014): 7727-7733.

[46] Yang, Xi, Wenqing Liu, Min Xiong, Yingying Zhang, Tao Liang, Jingting Yang, Mingsheng Xu, Jian Ye, and Hongzheng Chen. "Au nanoparticles on ultrathin MoS_2 sheets for plasmonic organic solar cells." Journal of Materials Chemistry A 2, no. 36 (2014): 14798-14806.

[47] Hu, Xiaotian, Lie Chen, Licheng Tan, Yong Zhang, Lin Hu, Bing Xie, and Yiwang Chen. "Versatile MoS_2 nanosheets in ITO-free and semi-transparent polymer power-generating glass." Scientific Reports 5, no. 1 (2015): 12161.

[48] Chuang, Ming-Kai, Shun-Shing Yang, and Fang-Chung Chen. "Metal nanoparticle-decorated two-dimensional molybdenum sulfide for plasmonic-enhanced polymer photovoltaic devices." Materials 8, no. 8 (2015): 5414-5425.

[49] Jiao, Kejia, Chunyang Duan, Xiaofeng Wu, Jiayuan Chen, Yu Wang, and Yunfa Chen. "The role of MoS_2 as an interfacial layer in graphene/silicon solar cells." Physical Chemistry Chemical Physics 17, no. 12 (2015): 8182-8186.

[50] Tsuboi, Yuka, Feijiu Wang, Daichi Kozawa, Kazuma Funahashi, Shinichiro Mouri, Yuhei Miyauchi, Taishi Takenobu, and Kazunari Matsuda. "Enhanced photovoltaic performances of graphene/Si solar cells by insertion of a MoS_2 thin film." Nanoscale 7, no. 34 (2015): 14476-14482.

[51] Huang, Zongyu, Weijia Han, Hongli Tang, Long Ren, D. Sathish Chander, Xiang Qi, and Han Zhang. "Photoelectrochemical-type sunlight photodetector based on MoS_2/graphene heterostructure." 2D Materials 2, no. 3 (2015): 035011.

[52] Rehman, Atteq ur, Muhammad Farooq Khan, Muhammad Arslan Shehzad, Sajjad Hussain, Muhammad Fahad Bhopal, Sang Hee Lee, Jonghwa Eom, Yongho Seo, Jongwan Jung, and Soo Hong Lee. "n-MoS_2/p-Si solar cells with Al_2O_3 passivation for enhanced photogeneration." ACS applied materials & interfaces 8, no. 43 (2016): 29383-29390.

[53] Baldovi, Herme G., Marcos Latorre-Sánchez, Ivan Esteve-Adell, Anish Khan, Abdullah M. Asiri, Samia A. Kosa, and Hermenegildo Garcia. "Generation of MoS_2 quantum dots by laser ablation of MoS_2 particles in suspension and their photocatalytic activity for H_2 generation." Journal of Nanoparticle Research 18 (2016): 1-8.

[54] Palsaniya, Shatrudhan, Harshal B. Nemade, and Ashok Kumar Dasmahapatra. "Synthesis of polyaniline/graphene/MoS_2 nanocomposite for high performance supercapacitor electrode." Polymer 150 (2018): 150-158.

[55] Aydın, Hasan, Sırrı Batuhan Kalkan, C. Varlikli, and Cem Çelebi. "P_3HT–graphene bilayer electrode for Schottky junction photodetectors." Nanotechnology 29, no. 14 (2018): 145502.

[56] Chaudhary, Nahid, Manika Khanuja, and S. S. Islam. "Broadband photodetector based on 3D architect of MoS_2-PANI hybrid structure for high photoresponsive properties." Polymer 165 (2019): 168-173.

[57] Ramasamy, Madeshwaran Sekkarapatti, Ka Yeon Ryu, Ju Won Lim, Asia Bibi, Hannah Kwon, Ji-Eun Lee, Dong Ha Kim, and Kyungkon Kim. "Solution-processed PEDOT:PSS/MoS_2 nanocomposites as efficient hole-transporting layers for organic solar cells." Nanomaterials 9, no. 9 (2019): 1328.

[58] Kumar, Sujit, Anjali Sharma, Yen Teng Ho, Akhilesh Pandey, Monika Tomar, A. K. Kapoor, Edward Yi Chang, and Vinay Gupta. "High performance UV photodetector based on MoS_2 layers grown by pulsed laser deposition technique." Journal of Alloys and Compounds 835 (2020): 155222.

[59] Krishnamoorthy, D., and A. Prakasam. "Preparation of MoS_2/graphene nanocomposite-based photoanode for dye-sensitized solar cells (DSSCs)." Inorganic Chemistry Communications 118 (2020): 108016.

[60] Musaab Khudhur Mohammed, Ghaleb Abd-Alwahab Al-Dahash, Amer K. H. Al.Nafiey " Employment of Polymer/Graphene-Ag nanocomposite Films prepared by PLAL for Optoelectric applications."(2021).

[61] Baby, Melbin, and K. Rajeev Kumar. "Impregnation of Microwave treated exfoliated MoS_2 nanosheets into PMMA matrix by solution casting for reinforcing applications." In IOP Conference Series: Materials Science and Engineering, vol. 1166, no. 1, p. 012033. IOP Publishing, 2021.

[62] Moniri, Samira, and Mohammad Reza Hantehzadeh. "Colloidal synthesis of MoS_2 NPs by nanosecond laser ablation of a bulk MoS_2 target in ethylene glycol solution." Optical and Quantum Electronics 53 (2021): 1-17.

[63] Ma, Jun, Yujie Yuan, and Ping Sun. "Performances enhancement of graphene/n-Si Schottky junction solar cells with dual-functional MoS_2 interfacial layers." Journal of Alloys and Compounds 883 (2021): 160898.

[64] Shin, Dong Hee, Chan Wook Jang, Jung Sun Ko, and Suk-Ho Choi. "Enhancement of efficiency and stability in organic solar cells by employing MoS_2 transport layer, graphene electrode, and graphene quantum dots-added active layer." Applied Surface Science 538 (2021): 148155.

[65] Li, Zhiwen, Siqi Hu, Qiao Zhang, Ruijuan Tian, Linpeng Gu, Yisong Zhu, Qingchen Yuan et al. "Telecom-band waveguide-integrated MoS_2 photodetector assisted by hot electrons." ACS Photonics 9, no. 1 (2022): 282-289.

[66] Shih, Yi-Shan, Wei-Chen Li, Jun-Hao Shen, Shao-Yu Chu, Wu-Yih Uen, Hsin-Ying Lee, Gong-Ru Lin, Yu-Cheng Chen, and Wei-Chen Tu. "Low-Power Photodetectors Based on PVA-Modified Reduced Graphene Oxide Hybrid Solutions." Macromolecular Rapid Communications 43, no. 8 (2022): 2100854.

[67] Augustine, Pius, Kishan Lal Kumawat, Deependra Kumar Singh, Saluru Baba Krupanidhi, and Karuna Kar Nanda. "MoS_2/SnO_2 heterojunction-based self-powered photodetector." Applied Physics Letters 120, no. 18 (2022).

[68] Velasco Davoise, Lara, Ana M. Díez-Pascual, and Rafael Peña Capilla. "Application of graphene-related materials in organic solar cells." Materials 15, no. 3 (2022): 1171.

[69] Fu, Nanxin, Jiazhen Zhang, Yuan He, Xuyang Lv, Shuguang Guo, Xingjun Wang, Bin Zhao, Gang Chen, and Lin Wang. "High-Sensitivity 2D MoS_2/1D MWCNT Hybrid Dimensional Heterostructure Photodetector." Sensors 23, no. 6 (2023): 3104.

[70] Loeza-Poot, M., J. Méndez-Hernández, M. Oviedo-Mendoza, R. Mis-Fernández, J. L. Peña, C. E. Peñuela-Cruz, and E. Hernández-Rodríguez. "Effects of the processing variables on the optical properties of P_3HT: PCBM absorber layer: A statistical point of view." Optical Materials 137 (2023): 113514.

[71] Liu, Chunyi. A study of particle generation during laser ablation with applications. University of California, Berkeley, 2005.

[72] Brown, Matthew S., and Craig B. Arnold. "Fundamentals of laser-material interaction and application to multiscale surface modification." In Laser precision microfabrication, pp. 91-120. Berlin, Heidelberg: Springer Berlin Heidelberg, 2010.

[73] Smith, Howard M., and A. F. Turner. "Vacuum deposited thin films using a ruby laser." Applied Optics 4, no. 1 (1965): 147-148.

[74] Ashfold, Michael NR, Frederik Claeyssens, Gareth M. Fuge, and Simon J. Henley. "Pulsed laser ablation and deposition of thin films." Chemical Society Reviews 33, no. 1 (2004): 23-31.

[75] Amendola, Vincenzo, and Moreno Meneghetti. "What controls the composition and the structure of nanomaterials generated by laser ablation in liquid solution?." Physical Chemistry Chemical Physics 15, no. 9 (2013): 3027-3046.

[76] Biswas, Abhijit, Ilker S. Bayer, Alexandru S. Biris, Tao Wang, Enkeleda Dervishi, and Franz Faupel. "Advances in top–down and bottom–up surface nanofabrication:Techniques, applications & future prospects." Advances in colloid and interface science 170, no. 1-2 (2012): 2-27.

[77] Zavabeti, Ali, Azmira Jannat, Li Zhong, Azhar Ali Haidry, Zhengjun Yao, and Jian Zhen Ou. "Two-dimensional materials in large-areas: synthesis, properties and applications." Nano-Micro Letters 12 (2020): 1-34.

[78] Fojtík, Anton, Horst Weller, U. Koch, and Arnim Henglein. "Photo-Chemistry of Colloidal Metal Sulfides 8. Photo-Physics of Extremely Small CdS Particles: Q-State CdS and Magic Agglomeration Numbers." Berichte der Bunsengesellschaft für physikalische Chemie 88, no. 10 (1984): 969-977.

[79] Yeh, Ming-Shin, Yuh-Sheng Yang, Yi-Pei Lee, Hsiu-Fang Lee, Ya-Huey Yeh, and Chen-Sheng Yeh. "Formation and characteristics of Cu colloids from CuO powder by laser irradiation in 2-propanol." The Journal of Physical Chemistry B 103, no. 33 (1999): 6851-6857.

[80] Mafuné, Fumitaka, Jun-ya Kohno, Yoshihiro Takeda, and Tamotsu Kondow. "Full physical preparation of size-selected gold nanoparticles in solution: laser ablation and laser-induced size control." The Journal of Physical Chemistry B 106, no. 31 (2002): 7575-7577.

[81] Fojtik, Anton, and Arnim Henglein. "Laser ablation of films and suspended particles in a solvent: formation of cluster and colloid solutions." berichte-bunsengesellschaftfur physikalische chemie 97 (1993): 252-252.

[82] Mafuné, Fumitaka, Jun-ya Kohno, Yoshihiro Takeda, Tamotsu Kondow, and Hisahiro Sawabe. "Formation and size control of silver nanoparticles by laser ablation in aqueous solution." The Journal of Physical Chemistry B 104, no. 39 (2000): 9111-9117.

[83] Tsuji, Takeshi, Toshihiko Kakita, and Masaharu. "Preparation of nano-size particles of silver with femtosecond laser ablation in water." Applied Surface Science 206, no. 1-4 (2003): 314-320.

[84] Jeon, Jiann-Shing, and Chen-Sheng Yeh. "Studies of silver nanoparticles by laser ablation method." Journal of the Chinese Chemical Society 45, no. 6 (1998): 721-726.

[85] Amendola, Vincenzo, and Moreno Meneghetti. "Laser ablation synthesis in solution and size manipulation of noble metal nanoparticles." Physical chemistry chemical physics 11, no. 20 (2009): 3805-3821.

[86] Nichols, William T., Takeshi Sasaki, and Naoto Koshizaki. "Laser ablation of a platinum target in water. II. Ablation rate and nanoparticle size distributions." Journal of Applied Physics 100, no. 11 (2006).

[87] Zhigilei, Leonid V., Zhibin Lin, and Dmitriy S. Ivanov. "Atomistic modeling of short pulse laser ablation of metals: connections between melting, spallation, and phase explosion." The Journal of Physical Chemistry C 113, no. 27 (2009): 11892-11906.

[88] Kabashin, Andrei V., and M. Meunier. "Synthesis of colloidal nanoparticles during femtosecond laser ablation of gold in water." Journal of Applied Physics 94, no. 12 (2003): 7941-7943.

[89] Lazar, Oana Andreea, Călin Constantin Moise, Anastas Savov Nikolov, Laura-Bianca Enache, Geanina Valentina Mihai, and Marius Enachescu. "The water-based synthesis of platinum nanoparticles using KrF Excimer laser ablation." Nanomaterials 12, no. 3 (2022): 348.

[90] Sobhan, Mushtaq A., Martin Ams, Michael J. Withford, and Ewa M. Goldys. "Ultrafast laser ablative generation of gold nanoparticles: the influence of pulse energy, repetition frequency and spot size." Journal of Nanoparticle Research 12 (2010): 2831-2842.

[91] Wagener, Philipp, Andreas Schwenke, Boris N. Chichkov, and Stephan Barcikowski. "Pulsed laser ablation of zinc in tetrahydrofuran: bypassing the cavitation bubble." The Journal of Physical Chemistry C 114, no. 17 (2010): 7618-7625.

[92] Mafuné, Fumitaka, Jun-ya Kohno, Yoshihiro Takeda, Tamotsu Kondow, and Hisahiro Sawabe. "Formation of gold nanoparticles by laser ablation in aqueous solution of surfactant." The Journal of Physical Chemistry B 105, no. 22 (2001): 5114-5120.

[93] Ashry, M., and S. Fares. "Radiation effect on the optical and electrical properties of CdSe (In)/p-Si heterojunction photovoltaic solar cells." Journal of Semiconductors 33, no. 10 (2012): 102001.

[94] Bisi, Olmes, Stefano Ossicini, and Lorenzo Pavesi. "Porous silicon: a quantum sponge structure for silicon based optoelectronics." Surface science reports 38, no. 1-3 (2000): 1-126.

[95] Demontis, Valeria. "Porous Silicon applications in biotechnology." (2007).

[96] Kittel, Charles. Introduction to solid state physics. John Wiley & sons, inc, 2005.

[97] Ilican, Saliha, Yasemin Caglar, Mujdat Caglar, and Fahrettin Yakuphanoglu. "Structural, optical and electrical properties of F-doped ZnO nanorod semiconductor thin films deposited by sol–gel process." Applied Surface Science 255, no. 5 (2008): 2353-2359.

[98] Stenzel, Olaf. The physics of thin film optical spectra. Berlin/Heidelberg, Germany: Springer, 2015.

[99] Klingshirn, Claus F. Semiconductor optics. Springer Science & Business Media, 2012.

[100] R. Palma, J. Rigueiro, and J. Duart, "Study of carrier transport in metal/porous silicon/Si structures " , J.Appl. Phys., 86, 12, (1999) 6911-6914.

[101] Paul, Aloke, Tomi Laurila, Vesa Vuorinen, and Sergiy V. Divinski. "Fick's laws of diffusion." Thermodynamics, diffusion and the kirkendall effect in solids (2014): 115-139

.

[102] Mohammed, M. "Effect of Preparation Conditions on the Structural and Optical Properties of TiO_2 Thin Films Deposited by Pulsed Laser Techniques", M.Sc., Thesis, Babylon University, College of Science, 2010.

[103] Łukasiak, Lidia, and Andrzej Jakubowski. "History of semiconductors." Journal of Telecommunications and information technology 1 (2010): 3-9.

[104] Mulya Dewi, Nur Oktri, Yoki Yulizar, and Dewangga Oky Bagus Apriandanu. "Green synthesis of Co_3O_4 nanoparticles using Euphorbia heterophylla L. leaves extract: characterization and photocatalytic activity." In IOP Conference Series: Materials Science and Engineering, vol. 509, p. 012105. IOP Publishing, 2019.

[105] Sze, Simon Min. Semiconductor devices: physics and technology. John wiley & sons, 2008.

[106] Mohammed J.," Preparation of some Organic Nanocomposites for Solar Cells and Sensing Applications", Ph.D. Thesis, College of Science, University of Babylon, (2017).

[107] Yahya, K. "Characterization of Pure and Dopant TiO2 Thin Films for Gas Sensors Applications,". "PhD diss., Ph. D Thesis, University of Technology Department of Applied Science, 1-147, 2010.

[108] Neamen, D. A. "Semiconductor Physics and Devices, University of New Mexico, Richard D. Irwin." (1992): 746.

[109] Wolf, Helmut F. "Semiconductors." (1971).

[110] Sharma, B. L., and R. K. Purohit. Semiconductor heterojunctions. Vol. 5. Elsevier, 2015.

[111] Durose, K., Asher, S.E., Jaegermann, W., Levi, D., McCandless, B.E., Metzger, W., Moutinho, H., Paulson, P.D., Perkins, C.L., Sites, J.R. and Teeter, G., 2004. Physical characterization of thin-film solar cells. Progress in Photovoltaics: Research and Applications, 12(2-3), pp.177-217.

[112] Budde, Wolfgang. "Physical detectors of optical radiation." Optical Radiation Measurements (1983).

[113] Borrello, Sebastian R., and Mark V. Wadsworth. "Photodetectors." Kirk-Othmer Encyclopedia of Chemical Technology (2000).

[114] Capper, Peter, and C. T. Elliott. "BOOK REVIEW: Infrared Detectors and Emitters: Materials and Devices." Measurement Science and Technology 12, no. 9 (2001): 1608.

[115] Al-Obaidi, Karam M., Mazran Ismail, and Abdul Malek Abdul Rahman. "Passive cooling techniques through reflective and radiative roofs in tropical houses in Southeast Asia: A literature review." Frontiers of Architectural Research 3, no. 3 (2014): 283-297.

[116] De Stefano, L., F. De Luca, G. Buccolieri, and P. Plescia. "Milling effects upon quantitative determinations of chrysotile asbestos by the reference intensity ratio method." Powder Diffraction 15, no. 1 (2000): 26-29.

[117] Widén, Joakim. Distributed Photovoltaics in the Swedish Energy System. Model Development and Simulations. No. NEI-SE--810. Uppsala Univ.(Sweden). Dept. of Engineering Sciences, 2009.

[118] Rani, R., and R. Velavan. "Preparation and characterisation of certain ii vi i iii vi_2 semiconductor thin films and transparent conducting oxides." (2004).

[119] Aldrin, Antony, and M. K. Jayaraj. "Preparation and characterisation of certain II-VI, I-III-VI_2 semiconductor thin films and transparent conducting oxides." PhD diss., Department of Physics, 2004.

[120] Partain, L. D. "Solar cells and their applications." In Fuel and Energy Abstracts, vol. 5, no. 36, p. 349. 1995.

[121] Max, Ming, and Liu Kang. "Principles and Application of Optical Communication." chapter 17 (1996): 865-867.

[122] El Assyry, A., Lamsayah, M., Warad, I., Touzani, R., Bentiss, F., and Zarrouk, A. Theoretical investigation using DFT of quinoxaline derivatives for electronic and photovoltaic effects. Heliyon, 6(3) (2020): p. e03620.

[123] Kalogirou, S. (Ed.). McEvoy's handbook of photovoltaics: fundamentals and applications. Academic Press. (2017).

[124] Jean, Joel, and Patrick Richard Brown. Emerging Photovoltaic Technologies. IOP Publishing, 2020.

[125] Solanki, Chetan Singh. Solar photovoltaics: fundamentals, technologies and applications. Phi learning pvt. Ltd., 2015.

[126] Karimzadeh, R., and N. Mansour. "The effect of concentration on the thermo-optical properties of colloidal silver nanoparticles." Optics & Laser Technology 42, no. 5 (2010): 783-789.

[127] Pope, Christopher G. "X-ray diffraction and the Bragg equation." Journal of chemical education 74, no. 1 (1997): 129.

[128] Hernández, M., A. Juarez, and R. Hernandez. "Interferometric thickness determination of thin metallic films." Superficies y vacío 9 (1999): 283-285.

[129] Traill, R., Can. Mineral., The crystal structures of molybdenum sulfide .Acta Crystallographica (1963).

[130] Quan, Hongying, Baochang Cheng, Dezhi Chen, Xiaohui Su, Yanhe Xiao, and Shuijin Lei. "One-pot synthesis of α-MnS/nitrogen-doped reduced graphene oxide hybrid for high-performance asymmetric supercapacitors." Electrochimica Acta 210 (2016): 557-566.

[131] Sakurai, Takeaki, Susumu Toyoshima, Masato Kubota, Toshihiro Yamanari, Tetsuya Taima, Kazuhiro Saito, and Katsuhiro Akimoto. "Structural study of P_3HT and P_3HT: PCBM thin films by synchrotron X-ray diffraction." Materials Science 25 Part B (2007): 2008.

[132] Asok, Aswathy, Adarsh Ajith Naik, S. Arunachalam, R. Govindaraj, and K. Haribabu. "Microwave assisted synthesis of polythiophene–molybdenum sulfide counter electrode in dye sensitized solar cell." Journal of Materials Science: Materials in Electronics 30 (2019): 13655-13663.

[133] Ansari, Muhammad Azhar, Shaikh Mohiuddin, Fatma Kandemirli, and Muhammad Imran Malik. "Synthesis and characterization of poly (3-hexylthiophene): improvement of regioregularity and energy band gap." RSC advances 8, no. 15 (2018): 8319-8328.

[134] Zhang, Ruiyang, Wenchao Wan, Dawei Li, Fan Dong, and Ying Zhou. "Three-dimensional MoS_2/reduced graphene oxide aerogel as a macroscopic visible-light photocatalyst." Chinese Journal of Catalysis 38, no. 2 (2017): 313-320.

[135] Ali, Gomaa AM, Mohammad R. Thalji, Wee Chen Soh, H. Algarni, and Kwok Feng Chong. "One-step electrochemical synthesis of MoS_2 /graphene composite for supercapacitor application." Journal of Solid State Electrochemistry 24 (2020): 25-34.

[136] Frey, G. L., S. Elani, M. Homyonfer, Y. Feldman, and R. Tenne. "Optical-absorption spectra of inorganic fullerene like M S_2 (M= Mo, W)." Physical Review B 57, no. 11 (1998): 6666.

[137] Abdi, Mahnaz M., H. N. M. Ekramul Mahmud, Luqman Chuah Abdullah, Anuar Kassim, Mohamad Zaki Ab. Rahman, and Josephine Liew Ying Chyi. "Optical band gap and conductivity measurements of polypyrrole-chitosan composite thin films." Chinese Journal of Polymer Science 30 (2012): 93-100.

[138] Wang, H., Wu, J., Cong, C., Shang, J., Yu, T., & Zhang, X.. "Preparation of MoS_2 nanosheets with large lateral size and thickness controllability by a two-step process. " Journal of Materials Chemistry (2014)C, 2(30):5987-5991.

[139] Huang, L., Liu, X., Chen, C., & Chen, X. (2018). "Tuning the properties of MoS_2 by laser ablation": A review. Materials Today Physics(2018), 6: 15-26.

[140] Adhikari, Bimalendu, Abhijit Biswas, and Arindam Banerjee. "Graphene oxide-based hydrogels to make metal nanoparticle-containing reduced graphene oxide-based functional hybrid hydrogels." ACS applied materials & interfaces 4, no. 10 (2012): 5472-5482.

[141] Nishida, Jun, Shinsuke Shigeto, Sohshi Yabumoto, and Hiro-O. Hamaguchi. "Anharmonic coupling of the CH-stretch and CH-bend vibrations of chloroform as studied by near-infrared electroabsorption spectroscopy." The Journal of Chemical Physics 137, no. 23 (2012).

[142] AbdulAlmohsin, S., and J. B. Cui. "Graphene-enriched P_3HT and porphyrin-modified ZnO nanowire arrays for hybrid solar cell applications." The Journal of Physical Chemistry C 116, no. 17 (2012): 9433-9438.

[143] Collomb, David, Penglei Li, and Simon J. Bending. "Nanoscale graphene Hall sensors for high-resolution ambient magnetic imaging." Scientific reports 9, no. 1 (2019): 14424.

[144] Kausar, Ayesha, Hafsa Ilyas, and Muhammad Siddiq. "Current research status and application of polymer/carbon nanofiller buck paper: A review." Polymer-Plastics Technology and Engineering 56, no. 16 (2017): 1780-1800.

[145] Mehmood, Ahsan, N. M. Mubarak, Mohammad Khalid, Priyanka Jagadish, Rashmi Walvekar, and E. C. Abdullah. "Graphene/PVA buck

paper for strain sensing application." Scientific Reports 10, no. 1 (2020): 20106.

[146] Hassoni, Majid H., Wisam J. Aziz, Ahmed N. Abd, and Nadir F. Habubi. "Invention and description of p-CuO/n-Si (200 ^{o}C) Heterojunction for Photodiode Applications." Journal of Global Pharma Technology 11, no. 02 (2019): 601-606.

[147] Ayhan, Muhammed Emre, Golap Kalita, Masaharu Kondo, and Masaki Tanemura. "Photoresponsivity of silver nanoparticles decorated graphene–silicon Schottky junction." RSC Advances 4, no. 51 (2014): 26866-26871.

[148] Ye, Jian-Hong, Chao-Kuang Cheng, Jeng-Yu Lin, Chi-Hsien Huang, Tsung-Kuang Yeh, and Chien-Kuo Hsieh. "Potential-controlled pulse electrochemical deposition of poly nanostructural two-dimensional molybdenum disulfide thin films as a counter electrode for dye-sensitized solar cells." Surface and Coatings Technology 394 (2020): 125855.

[149] Nawz, Tahreem, Amna Safdar, Muzammil Hussain, Dae Sung Lee, and Muhammad Siyar. "Graphene to advanced MoS_2: A review of structure, synthesis, and optoelectronic device application." Crystals 10, no. 10 (2020): 902.

[150] Kim, Minjae, Malik Abdul Rehman, Kyung-Mun Kang, Yue Wang, Sewon Park, Hong-Sub Lee, Sanjib Baran Roy et al. "The role of oxygen defects engineering via passivation of the Al_2O_3 interfacial layer for the direct growth of a graphene-silicon Schottky junction solar cell." Applied Materials Today 26 (2022): 101267.

[151] Sun, Bo, Tielin Shi, Zhiyong Liu, Youni Wu, Jianxin Zhou, and Guanglan Liao. "Large-area flexible photodetector based on atomically thin MoS_2/graphene film." Materials & Design 154 (2018): 1-7.

[152] Yadav, Anjali, Aditi Upadhyaya, Saral Kumar Gupta, Ajay Singh Verma, and Chandra Mohan Singh Negi. "Poly-(3-hexylthiophene)/graphene composite based organic photodetectors: The influence of graphene insertion." Thin Solid Films 675 (2019): 128-135.

[153] Liu, Beiyun, Yongfeng Chen, Congya You, Yawei Liu, Xinyi Kong, Jingfeng Li, Songyu Li et al. "High performance photodetector based on graphene/MoS_2/graphene lateral heterostrurcture with Schottky junctions." Journal of Alloys and Compounds 779 (2019): 140-146.

[154] Soleimani, Ehsan, Seyed Foad Aghamiri, Payam Molla-Abbasi, and Meisam Shabanian. "Tuning the polymer–graphene interfaces by picric acid molecules to improve the sensitivity of a prepared conductive polymer composite gas detector." Iranian Polymer Journal 29 (2020): 341-350.

[155] Lee, Ilmin, Won Tae Kang, Ji Eun Kim, Young Rae Kim, Ui Yeon Won, Young Hee Lee, and Woo Jong Yu. "Photoinduced tuning of Schottky barrier height in graphene/MoS_2 heterojunction for ultrahigh performance short channel phototransistor." ACS nano 14, no. 6 (2020): 7574-7580.

[156] Liirò-Peluso, Letizia, James Wrigley, David B. Amabilino, and Peter H. Beton."Submolecular Resolution Imaging of P_3HT:PCBM Nanostructured Films by Atomic Force Microscopy: Implications for Organic Solar Cells." ACS applied nano materials 5, no. 10 (2022): 13794-13804.

[157] Korte, Dorota, Egon Pavlica, Domen Klančar, Gvido Bratina, Michal Pawlak, Ewa Gondek, Peng Song, Junyan Liu, and Beata Derkowska-Zielinska. "Influence of P_3HT:PCBM Ratio on Thermal and Transport Properties of Bulk Heterojunction Solar Cells." Materials 16, no. 2 (2023): 617.

الخلاصـــــــة

يقدم هذا العمل، لأول مرة، إنتاج مركب نانوي (P_3HT-G/MoS_2) عن طريق الاستئصال بالليزر لأهداف الكرافين وثاني كبريتيد الموليبدينوم (MoS_2) في محلول بولي (3- هكسيل ثيوفين) (P_3HT) .تم تحليل الخصائص التركيبية والمورفولوجية والبصرية للمركب النانوي المحضر باستخدام أدوات التحليل الطيفي XRD و AFM و FTIR و TEM و UV- Vis.

أشار تحليل XRD إلى وجود العديد من القمم التي تنتمي إلى الجسيمات النانوية للـ G و MoS_2. وأظهر تحليل XRD أيضًا وجود علاقة بين شدة هذه القمم وعدد نبضات الليزر. توفر نتائج تحليل FTIR معلومات حول الرابطة القوية بين عناصر المركبات النانوية لعينة-P_3HT $G_{800P}/MoS_{2\ 800P}$. كما لاحظ تصوير TEM أن الجسيمات النانوية للـ G و MoS_2عبارة عن أشكال نصف كروية وأشارت النتائج الإحصائية إلى زيادة توزيع الحجم من 3.1 إلى 20.8 نانومتر عن طريق زيادة عدد نبضات الليزر.

أظهرت ملاحظات التحليل الطيفي للأشعة فوق البنفسجية والمرئية (UV-Vis) أن معامل الامتصاص والامتصاصية قد زادا عن طريق زيادة عدد نبضات الليزر بسبب تركيز الجسيمات النانوية للـ G وMoS_2 . أشارت النتائج أيضًا إلى أن فجوة نطاق الطاقة المباشرة والتي تعود للعينة P_3HT-$G_{800P}/MoS_{2\ 800P}$ تبلغ 2.1 الكترون فولت وهي مناسبة جدًا للتطبيقات الإلكترونية البصرية. أظهرت الدراسة الكهربائية باستخدام تأثير هول أن مادة المركب النانوي P_3HT-G/MoS_2 هي من النوع سالب الشحنة وأن حركة وتركيز حاملات الشحنة تعتمد على عدد نبضات الليزر.

تم استخدام المركب النانوي P_3HT-G/MoS_2 لتصنيع أجهزة الكشف الضوئي والخلايا الشمسية .لقد وجد أن عدد نبضات الليزر المستخدمة لإنتاج الجسيمات النانوية للـ G و MoS_2 يؤثر على أداء الكاشف الضوئي. وكانت القيمة العظمى للاستجابة الطيفية والكشفية النوعية والكفاءة الكمية للكاشف المصنع هي 0.36A/W، 5.1×10^{12} $cm.Hz^{1/2}.W^{-1}$ و 49.2% على التوالي عند طول موجي (900) نانومتر بسبب حافة امتصاص السيليكون. بينما القيمة العظمى للاستجابة الطيفية والكشفية النوعية والكفاءة الكمية للكاشف المُصنع كانت0.24 A/W، 3.39×10^{12} $cm.Hz^{1/2}.W^{-1}$ و38.9% على التوالي عند طول موجي (760) نانومتر بسبب حافة امتصاص الجسيمات النانوية للمركب (P_3HT-G / MoS_2).

في هذا العمل، نعرض، لأول مرة، تصنيع الخلايا الشمسية باستخدام مركب نانوي (P_3HT-G/MoS_2) وقمنا بدراسة تأثير عدد نبضات الليزر المستخدمة لإنتاج الجسيمات النانوية للـ G و MoS_2 على كفاءة الخلايا الشمسية المصنعة .تم دراسة الخواص الكهربائية للخلية الشمسية المصنعة في ظروف الظلام والضوء وأظهرت النتائج أن كفاءتها كانت 6.11% مع V_{oc} و I_{sc} يساوي (97) مللي فولت و(176) مللي أمبير على التوالي.

جمهورية العراق

وزارة التعليم العالي والبحث العلمي

جامعة بابل / كلية العلوم للبنات

قسم فيزياء الليزر

تحضير اغشية رقيقة بوليمر – الكرافين / MoS_2 بطريقة الاستئصال الليزري: التوصيف والتطبيقات الالكتروضوئية

أطروحة

مقدمة الى مجلس كلية العلوم للبنات/جامعة بابل كجزء من متطلبات نيل درجة الدكتوراه فلسفة في العلوم/فيزياء الليزر وتطبيقاته

من قبل الطالبة

نغم محمد عبيد

إشراف

أ.م.د. أمير خضير النافعي

أ.د. غالب عبد الوهاب علي الدهش

2023 م **1444 هـ**